Hydrogen embrittlement resistance in advanced high strength: vanadium bearing and TRIP-assisted steels

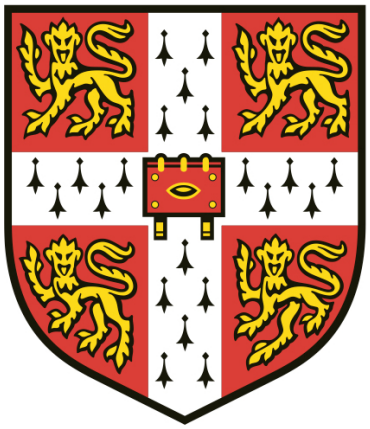

Beriham Ibrahim Y Basha

Magdalene College

University of Cambridge

This thesis is submitted for the degree of Doctor of Philosophy

September 2019

Declaration

This thesis is the result of my own work and includes nothing which is the outcome of work done in collaboration except as declared in the Preface and specified in the text. It is not substantially the same as any that I have submitted, or, is being concurrently submitted for a degree or diploma or other qualification at the University of Cambridge or any other University or similar institution except as declared in the Preface and specified in the text. I further state that no substantial part of my thesis has already been submitted, or, is being concurrently submitted for any such degree, diploma or other qualification at the University of Cambridge or any other University or similar institution except as declared in the Preface and specified in the text. It does not exceed the prescribed word limit for the relevant Degree Committee.

Hydrogen embrittlement resistance in advanced high strength: vanadium bearing and TRIP-assisted steels

Abstract

Advanced high strength steels undergo a series of microstructural transitions associated with damage, these lead to failure especially when hydrogen enters the lattice and gets trapped in defects. It is desired to design advanced steels highly resistant to hydrogen embrittlement (HE), while preserving a balance between their superior strength and ductility. For this purpose, a new 100Cr6 bearing steel is proposed with 0.3 wt.% vanadium, compared to a previous grade containing 0.5 wt.% vanadium, for which a new heat treatment is proposed.

Mechanical testing was carried out on hydrogen-free and hydrogen-charged specimens to evaluate the potency of V_4C_3 traps to reduce the HE susceptibility in such steels. The nature of crack propagation and HE mechanisms in 100Cr6, 100Cr6+0.3V and 100Cr6+0.5V were assessed using hydro-hardness technique, which provides direct observation of hydrogen diffusion to cracks. The results showed that pre-charged 100Cr6+0.5V are anomalously weaker compared to 100Cr6+0.3V. Slow strain rate tests (SSRT) on notched round bar specimens have been carried out at a constant tensile crosshead speed of 0.005 mm min^{-1}. Failure was more pronounced in vanadium-free specimens as V_4C_3 limited the transition from ductile to brittle fracture mode in 100Cr6+0.5V steel. Rolling contact fatigue (RCF) test was also carried out to study the propagation of cracks un-

der rolling contact fatigue conditions. It was concluded that 100Cr6+0.5V steel has longer bearing life and higher resistance to hydrogen embrittlement than 100Cr6. However, microstructural analysis confirmed the presence of non-metallic inclusions (NMIs) in 100Cr6+0.5V steel and the disadvantageous effects on its mechanical properties were recorded.

A crucial consequence of plastic deformation during RCF is the transformation-induced hydrogen desorption which occurs when retained austenite transforms into martensite. This mechanism can be investigated through studying the HE susceptibility of transformation-induced plasticity (TRIP) steels. An intensive study was carried out to optimise the TRIP steel heat treatment aiming to achieve an ultimate tensile strength (UTC) of 1303 MPa. The microstructure showed lower bainite structure consisting of ferrite plates, film-like and blocky retained austenite. The most promising microstructure with respect to the expected UTC was obtained after bainitic isothermal tempering at 302 °C for 24 to 30 minutes. Thermal desorption analysis was used to study desorption of hydrogen from TRIP steel. The high activation energy of diffusion indicates that the hydrogen is trapped in retained austenite which is considered as irreversible trap. However, there was no evidence demonstrating the advantage of retained austenite on preventing embrittlement after saturation with hydrogen. As a result, it can be inferred that a finer and lower fraction of retained austenite can reduce the mass of trapped hydrogen minimising the susceptibility to HE in TRIP-assisted steels.

Beriham Ibrahim Y Basha

Preface

This dissertation is submitted for the degree of Doctor of Philosophy at the University of Cambridge. The research reported herein was conducted under the supervision of Professor P.E.J. Rivera-Díaz-del-Castillo in the Department of Materials Science and Metallurgy, University of Cambridge, between October 2014 and September 2019. This work is original to the best of my knowledge, except where acknowledgements and references are made to previous work. Neither this, nor any substantially similar dissertation has been or is being submitted for any degree, diploma or other qualification at any other university or institution. This dissertation does not exceed the word limit of 60,000 words.

Part of this work has been presented in the following publication:

- E.I. Galindo-Nava, B.I.Y. Basha, and P.E.J. Rivera-Díaz-del-Castillo. Hydrogen transport in metals: Integration of permeation, thermal desorption and degassing. *Journal of Materials Science & Technology*, **vol.** 33, pp. 1433-1447, 2017.

- Beriham I. Basha, and P.E.J. Rivera-Díaz-del-Castillo. Developing hydrogen resistant bearing steels of reduced vanadium content and simplified heat treatments. *In preparation.*

- Beriham I. Basha, and P.E.J. Rivera-Díaz-del-Castillo. A new aspect on studying

the nature of crack propagation and hydrogen embrittlement mechanism in martensitic 100Cr6 bearing steels. *In preparation.*

- Beriham I. Basha, David San Martin, Jakub J. Rydel, P.E.J. Rivera-Díaz-del-Castillo. The role of vanadium in improving the rolling contact fatigue life of martensitic 100Cr6 bearing steel. *In preparation.*

- Beriham I. Basha, Shengyen Li, Taymaz Jozaghi, Pejman Honarmandi, Ibrahim Karaman, Raymundo Arroyave, P.E.J. Rivera-Díaz-del-Castillo. Optimisation of heat treatment of Fe-C-Mn-Si-Al TRIP steel. *In preparation.*

Beriham Basha

September 2019

Acknowledgements

First and about all, I thank the Almighty God for everything. I would like to thank the University of Cambridge for offering me this opportunity to pursue my PhD degree. My grateful gratitude goes to Princess Nourah bint Abdulrahman University in Saudi Arabia for supporting and sponsoring my PhD scholarship. I am also thankful to the financial support received from Vanitec Ltd for the experimental part of my research, and to SKF who gave access to their laboratory and research facilities. This work was supported in part by the Engineering and Physical Sciences Research Council (Programme Grant Number EP/L014742/1).

I am also greatly indebted to my supervisor Professor Pedro Rivera-Díaz-del-Castillo, this work would not have been possible without his guidance and support from the start of the project till date, under his guidance, I successfully overcame many difficulties and gained a great deal of knowledge. I must also mention Dr Rosie Ward, the Academic Secretary, for her unconditional and endless support.

I also wish to thank Professor Mark Rainforth and his team from the University of Sheffield for providing me with the material necessary for this research. I am equally thankful to the support received through the collaborative work undertaken with the Department of Materials Science and Engineering in Texas A&M University. Many thanks also to Dr David San Martín from CENIM who encouraged and convinced me during

our many discussions. I also thank Dr Enrique Galindo-Nava for sharing expertise and valuable guidance.

I greatly appreciate and acknowledge the cooperation with Sarah Hopkin from the University of Oxford for sharing her unpublished APT results. Special thanks to Jakub Rydel for offering me a number of his specimens to complete my RCF tests. I am also immensely grateful to all the technicians and lab assistants in the Department of Materials Science & Metallurgy for their assistance and patience. I am indebted to all my friends and colleagues in SKF UTC and Phase Transformation groups.

My parents and siblings, I would never be able to pay back your love and affection, thank you for showing faith in me and giving me the liberty to choose what I desired. Finally, to my soulmate, my husband Saud, thanks for your continued support, you were always around at times I thought that it is impossible to continue, you are my source of strength, words would never say how grateful I am to you.

Contents

Nomenclature

α	Ferrite
α'	Martensite
β^*	Atomic attachment rate
$\triangle G^*$	Nucleation barrier
$\triangle G_1$	Critical driving force at M_s
$\triangle G_2$	Amount of driving force needed for transformation at T_1
γ	Austenite
γ_k^3	Interface Gibbs energy density
ϕ	Heating rate corresponding to the de-trapping activation energy
τ	Incubation time
Ac_1	Austenite start temperature
Ac_3	Austenite finish temperature
AHSS	Advanced high strength steels
AIDE	Adsorption-induced dislocation emission
APT	Atom probe tomography
BIT	Bainite isothermal transformation
bcc	Body-centered cubic
C_i^k	Concentration of component i in precipitate k

$C_i'^k$	Evolution rate of a precipitate
CR	Cooling rate
DER	Dark etching regions
E_a	De-trapping activation energy
EBSD	Electron backscatter diffraction
ECAE	Equal Channel Angular Extrusion
EDX	Energy dispersive X-ray
F	Driving force
f	Shape factor of the nucleus
fcc	Face-centered cubic
G	Total Gibbs free energy
GC	Gas chromatography
HAB	High angle bands
HE	Hydrogen embrittlement
HEDE	Hydrogen-enhanced decohesion
HELP	Hydrogen-enhanced local plasticity
HISCC	Hydrogen-induced stress corrosion cracking
HR	Heating rate
HSTD	Tank with a standard gas mixture to calibrate the hydrogen content in TDA
HT	Heat treatment
I	Interfacial energy
IA	Intercritical annealing
IG	Intergranular cracking mood
J	Nucleation rate
k_β	Boltzmann constant

KAIQ	Kernel average image quality
KWN	Kampmann-Wagner Numerical model
L_T	Empirical relationship
LAB	Low angle bands
LCF	Low cycle fatigue
M_s	Martensite start temperature
MFC	Mass flow control
$N_\circ$	Total number of potential nucleation sites
NMI	Non-metallic inclusions
OM	Optical microscopy
ppm	Parts per million
q_i, $\mathrm{q}_i^{'}$	Independent state parameters
Q	Rate of the total Gibbs energy dissipation
$\mathrm{r}_k^{'}$	Growth rate of a precipitate k
r_k	Radius of the precipitate k
R	The gas constant
RCF	Rolling contact fatigue
RT	Room temperature
SEM	Scanning electron microscopy
SSRT	Slow strain rate test
STEM	Scanning transmission electron microscopy
T_0	Temperature where α and γ of identical chemical composition have the same free energy
T_1	Temperature above M_s
T_p	TDA peak temperature corresponding to $-E_a$
T	Absolute temperature

t	Time
TDA	Thermal desorption analysis
TEM	Transmission electron microscopy
TG	Transgranular cracking mode
TRIP	Transformation-induced plasticity
TWIP	Twinning-Induced Plasticity
U	External applied stress
UTS	Ultimate tensile strength
V_4C_3	Vanadium carbides
VN	Vanadium nitride
WEA	White etching area
WEB	White etching band
WEC	White etching crack
X_B^M	Equilibrium composition of component B in matrix M
X_B^β	Equilibrium composition of component B in precipitate β
XRD	X-ray diffraction
YS	Yield strength
Z	Non-equilibrium Zeldovich factor

Chapter 1

Introduction

Since its discovery in the 1870s [1], extensive studies have been carried out to understand the hydrogen-induced mechanical degradation mechanisms of steels, but despite intensive research, hydrogen embrittlement (HE) - also known as delayed fracture - of high strength steels [2–4] remains a mystery due to hydrogen high mobility and its low solubility in iron [5]. It is believed that HE begins when diffusible hydrogen atoms are introduced into steels from the environment and accumulate by stress-induced diffusion at stress concentrated regions causing cracks initiation and propagation [6]. Under normal conditions when steels are subjected to large plastic deformation, they undergo substantial changes of microstructure, such as forming dislocations that act as stress relieve in the material [7]. However, in the presence of hydrogen, dislocations are blocked by hydrogen atoms. The hindrance of their movement results in loss of ductility and toughness of the steel that eventually leads to sudden failure without warning [8]. Not long ago, the attention to vanadium carbides V_4C_3 increased because they were found to suppress HE whilst enhancing steel strength [9]. Recently, Szost *et al.* investigated the efficiency of V_4C_3 in hydrogen trapping in martensitic 100Cr6+0.5V bearing steel, they reported that the most

effective precipitate size for V_4C_3 hydrogen trapping is around 10 nm [10, 11], owing to the fact that the size and coherency of carbides are major factors behind the capability of trapping hydrogen during electrochemical charging [12]. The ability of carbides to trap hydrogen depends also on the interaction with hydrogen which is determined by: (1) the binding energy which expresses the strength of the trap, as each trapping site is characterised by its binding energy, (2) the de-trapping activation energy needed for hydrogen to diffuse/escape from the trapping site [13, 14].

Bearings are key elements in machines that contain rotating parts, they are crucial for friction reduction during operation, Figure 1.1. While they facilitate the desired motion under heavy loading, they are carefully designed to combine high performance with long life. In rotating elements such as bearing, fatigue performance depends on many factors including material properties, loading, service conditions, and environmental factors [15]. However, it is generally recognised that the presence of hydrogen contributes to bearings failure, this is evidenced by excessive vibration or even fracture, and when they do fail, their failure causes major and costly breakdowns. Research has shown that rolling contact fatigue (RCF) damage can initiate within the steel at non-metallic inclusions (NMIs), like MnS and Al_2O_3 [16], that form in bearing steels during material production and distribute with various orientations affected by the flow of material during processing [15]. Inclusions are attributed to hydrogen accumulation around their stress field [17] and shorten bearing life because hydrogen, according to decohesion theory [18], can reduce cohesive strength between metal atoms resulting in crack initiation and propagation.

In this thesis, chapter 2 presents a narrative review of previous findings as well as theoretical and methodological contributions of HE on advanced high strength steels, in particular bearing and transformation-induced plasticity (TRIP) steels. Chapter 3 cov-

Figure 1.1: Typical spherical roller bearings [19].

ers the modelling part of this study. The first part of chapter 4 presents an intensive experimental study which involves tools to enable the design of HE-resistant industrial high strength 100Cr6 steels. Microstructure characterisation followed by systematic measurements of hydrogen trapping by V_4C_3 precipitates. The de-trapping activation energy for 100Cr6, 100Cr6+0.5V and 100Cr6+0.3V steels are obtained. It is also important to understand the plastic behaviour occurring due to the presence of NMIs, for which rigorous tensile and RCF tests were conducted on hydrogen-free and hydrogen-charged 100Cr6 and 100Cr6+0.5V steels. The nature of crack propagation and HE mechanisms in 100Cr6, 100Cr6+0.3V and 100Cr6+0.5V were examined by hydro-hardness testing. The second part of chapter 4 highlights the work done on a newly designed CMnAlSi TRIP-assisted steel. It gives detailed information experimental analysis of two-stage heat treatment: intercritical annealing and bainite isothermal transformation, examination of different bainitic isothermal holding times in order to evaluate the influence of bainitic transformation on the final microstructure and the mechanical properties of the studied

TRIP steel, structural constituents identification by means of dilatometery, microscopic observations and X-ray diffraction, different hydrogen charging test designed for different purposes. Chapter 5 displays the results with detailed discussion. Chapter 6 summarises the finding of this study and the researcher propositions for future work to examine more mechanical features of the studied steel.

Chapter 2

Literature review

2.1 Mechanisms of hydrogen embrittlement in advanced high strength steels

Steels with yield strength exceeding 1000 MPa are generally referred to as advanced high strength steels (AHSS) [20]. These steels are carefully designed to meet the increasing demand on industrial unique applications such as aerospace and automotive structures.

Bearings, for example, are typically manufactured from high carbon steels widely used in demanding service conditions, they provide high wear resistance and rolling fatigue strength [21]. However, these mechanical elements are subjected to rolling contact fatigue (RCF) and undergo a series of microstructural transitions associated with damage leading to failure. Failure is generally considered to occur when mechanical components no longer fulfill their intended aim. In rotating elements, this is evidenced by excessive vibration or even fracture. Prior to this, some microstructural transitions arise including dissolution, coarsening of hardening precipitates, and the formation of nanosized dislo-

cation cellular structures. It is not clear whether these transitions are the effect or the cause of crack formation. The presence of hydrogen increases the issue by reducing the fracture toughness of the steel [22], therefore, understanding the factors that control microstructural transitions would be essential for improving the life of bearing steel.

In a similar way, advanced high strength steels for automotive applications have an excellent combination of high strength and ductility due to their multi-phase microstructure. For example, multi-phase TRIP-assisted steels have outstanding properties that are based on the stability of retained austenite in their structure, but again, hydrogen causes a reduction in ductility and fracture stress [23].

Hydrogen embrittlement - also known as hydrogen induced cracking - is a phenomenon that involves ingress of hydrogen into the metal, causing degradation to its mechanical properties. When hydrogen atoms diffuse into the lattice, they migrate toward high stress regions causing microcracks. Hydrogen atoms then accumulate on the crack tips, and with the steel being loaded for a period of time, the microcracks propagate and grow until failure, which occurs often unexpectedly. Almost all metallic materials are prone to hydrogen damage when a sufficient amount of hydrogen enters the material. However, the effect of hydrogen embrittlement increase with the strength level of the steel, for instance, martensitic structures are more susceptible than bainitic and austenitic steels. Embrittlement due to hydrogen is much more pronounced in martensitic and ferritic steels even with relatively low concentrations of hydrogen [24] because of the higher diffusivity of hydrogen in these structures, Figure 2.1 [25].

Hydrogen embrittlement is classified into external and internal according to the hydrogen source Figure 2.2. External type, Figure 2.2a, takes place in hydrogen containing atmosphere, as hydrogen atoms are introduced individually to the surface of a material

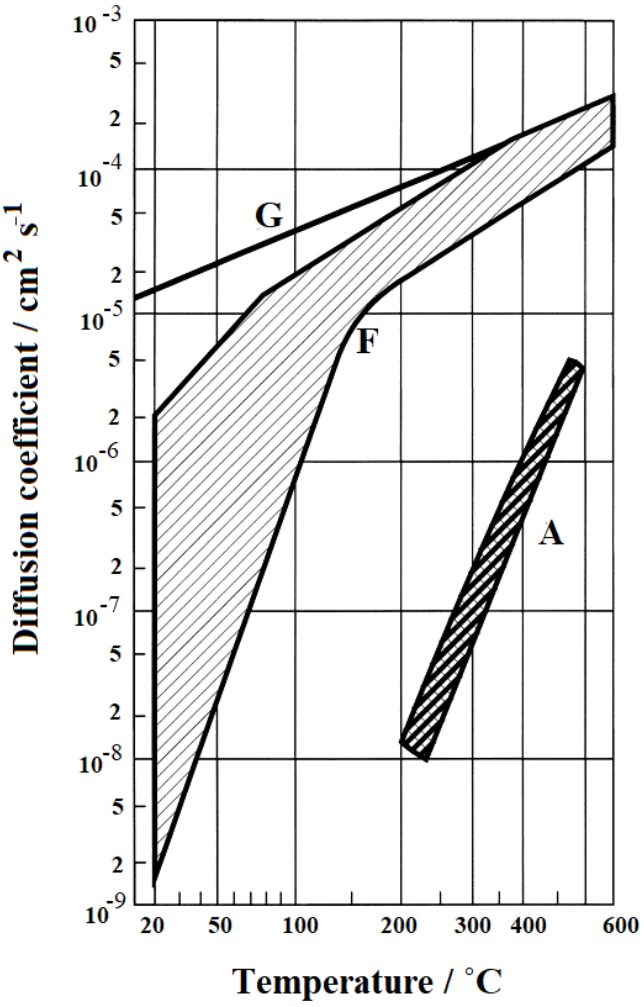

Figure 2.1: Diffusion coefficient for hydrogen in ferrite (F) and austenite (A). G is the lattice diffusion [25] which refers to the hydrogen atomic diffusion within the crystalline lattice [26].

and ingress to the lattice [27]. The damage here appears in a form of ductility loss, reduced tensile strength, and brittle fracture mode [28]. In the internal type, Figure 2.2b, the hydrogen is present in the bulk from earlier stages of steel processing or fabrication, mostly recombined in the form of hydrogen molecules [29], and the embrittlement occurs later during the application of load [14].

Oriani's theory [33] on hydrogen diffusion through metal and its impact as an embrittling agent has been widely recognised. According to the theory, hydrogen tends to

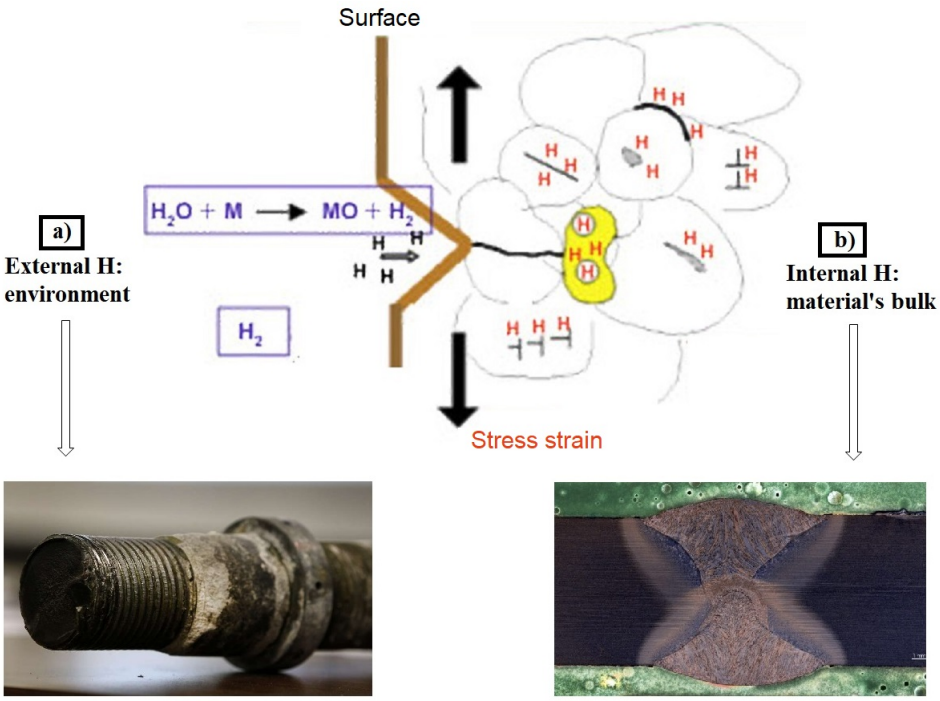

Figure 2.2: Hydrogen embrittlement types [30]: a) External: the image displays a rod found broken in the base of the self-anchored suspension span (SAS) tower of the new Bay Bridge, San Francisco-Oakland [31]. b) Internal: light microscopy image of a welded connection weld structure [32].

embrittle metals by accumulating at cracks tips reducing the cohesive strength between atomic bonds. This gives rise to applied stresses to become greater than the local maximum cohesive force per unit area, leading to a considerable toughness reduction. The theory also considered two types of sites that accommodate hydrogen in the lattice: reversible and irreversible trapping sites, with the later being counted as favourable spots for hydrogen atoms. Furthermore, Oriani calculated the density of hydrogen in trapping sites that is necessary to initiate a crack at a grain boundary. He found that increasing the reversible trap density reduces grain boundary cracking, while irreversible trapping sites restrict the cracking kinetics.

Later, several models have been put forth to interpret the influence of hydrogen on the

mechanical properties of high strength steels. According to the adsorption-induced dislocation emission (AIDE) mechanism [34], hydrogen absorbs through the surface of a steel at high stress regions of crack tips. It then accelerates the release of dislocations from the crack tip, causing the crack to propagate and grow, resulting in intense deformation in the crack surrounding area. The hydrogen-enhanced local plasticity (HELP) mechanism [35] suggests that dislocations mobility is stimulated due to the solute hydrogen accumulation around dislocation cores around the crack tip, which results in a reduction of the elastic interactions between dislocations and neighboring elastic obstacles. As a consequence, the stress required for dislocation pileups is reduced and plasticity is enhanced, resulting in subcritical crack growth on the macroscopic scale [36], Figure 2.3 [36, 37].

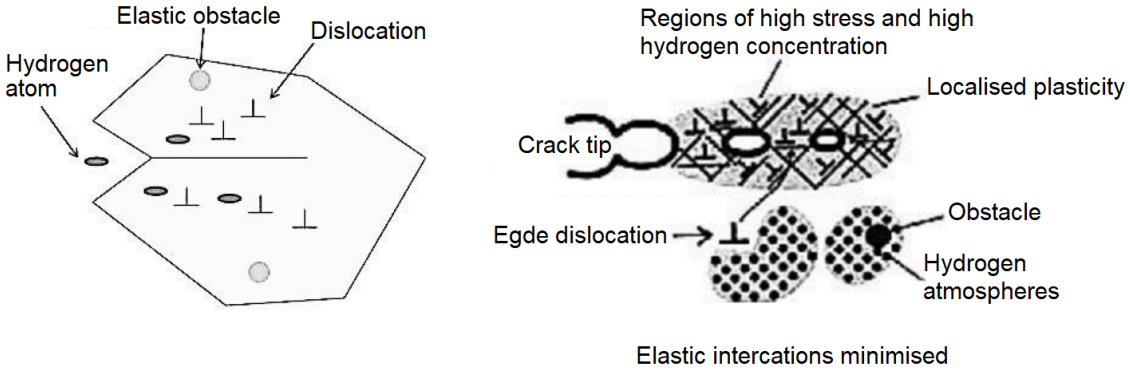

Figure 2.3: Schematic diagram illustrating the HELP mechanism. The elastic interactions between dislocations and neighboring elastic centers is decreased due to high hydrogen concentration around the crack tip [36, 37].

Hydrogen-enhanced decohesion (HEDE) mechanism [38, 39] suggests that hydrogen segregates at the dislocation shielding region at the crack tip and weakens the cohesive metallic bonds between metal atoms, causing reduction in the local atomic cohesion strength. As a result, the damage can occur in the presence of hydrogen under any low tensile stresses causing tensile separation of atoms (decohesion) and brittle crack propagation, Figure 2.4 [36, 37].

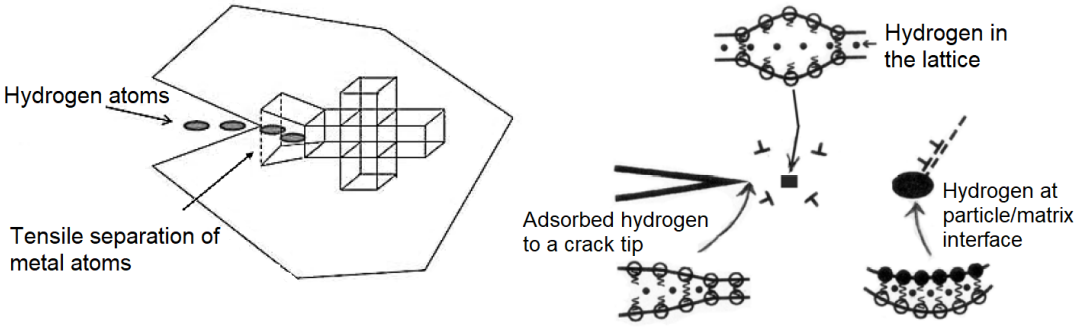

Figure 2.4: Schematic diagram illustrating the HEDE mechanism. Iron bonds are weaken by hydrogen in the lattice, dislocation can increase stress field [36,37].

AIDE and HEDE could occur sequentially. AIDE occurs first till the stress from emitted dislocations increased then HEDE occurs, followed by AIDE again when the crack tip moves away from the stress field of the previously emitted dislocations [40–42].

Hydrogen-induced stress corrosion cracking (HISCC) is a type of damage that is attributed to hydrogen embrittlement. It applies to high-tensile steels in low aggressive water solutions [43] as a result of residual or applied stresses after being subjected to a process involving corrosion and becomes more detrimental in a hydrogen-rich environment. The so-called hydrogen-induced stress corrosion cracking is described as the formation of cracks in metals under the influence of a tensile stress [25]. The source of tensile stresses varies, it can be external loads, thermal or residual stresses [14]. Despite the fact that the time needed to initiate stress corrosion cracking decreases by increasing these stresses, its formation and progress depend on other factors such as chemical composition and the thermal condition of the material, grain size, presence of secondary phases, precipitates, and other [44–46]. Depending on the microstructure, cracks grow via an intergranular mode (IG) as the crack grow along grain boundaries, or via a transgranular mode (TG) where the crack grows through the grains [47]. The influence of diffusible hydrogen con-

tent on the fracture stresses is revealed in Figure 2.5 for a medium carbon high strength steel. Two regions of fracture modes, ductile and intergranular, are observed.

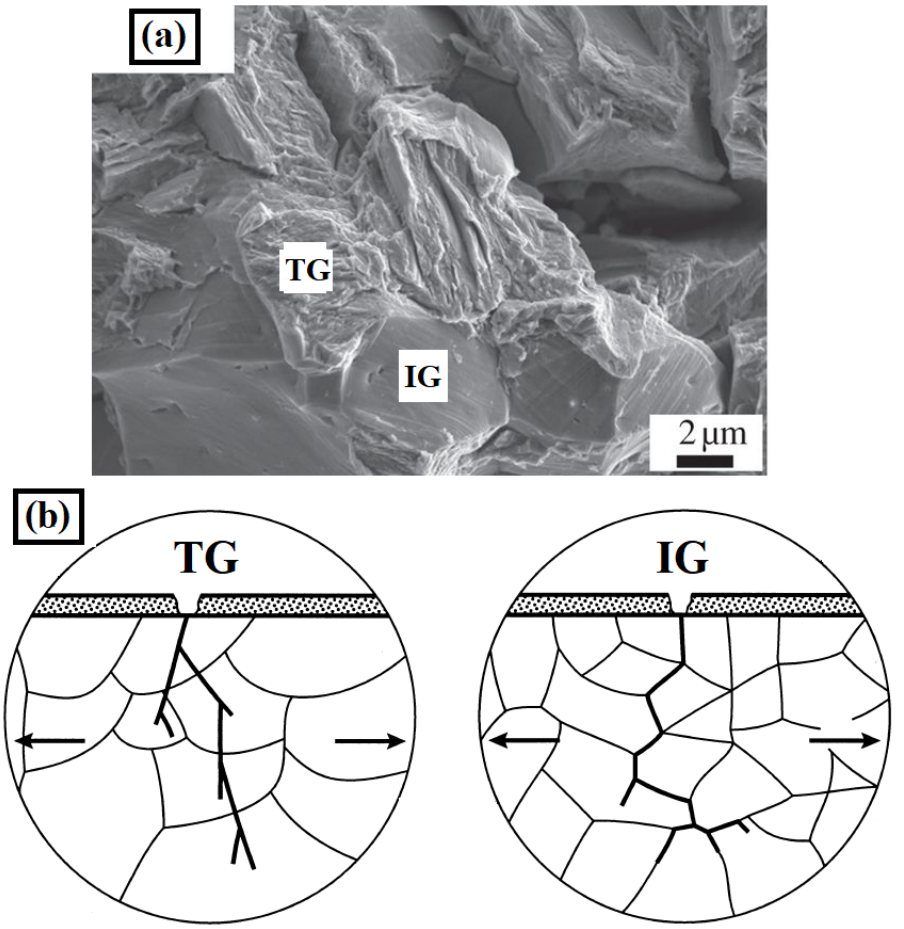

Figure 2.5: a) Fracture surface showing both intergranular (IG) and transgranular (TG) fractures in samples charged with 1 A m^{-2} [48]. b) Mechanism of intergranular and transgranular fractures [25].

Koyama *et al.* [49] examined the effect of hydrogen content in a Fe-Mn-C twinning-induced plasticity (TWIP) steel. It was found that for a low diffusible hydrogen content (e.g. 0.8 ppm), the steel showed a ductile fracture behaviour similar to the hydrogen-free case, whereas with relatively high diffusible hydrogen content ($>$ 1.24 ppm) the material exhibited intergranular fracture and a degradation of the true fracture stress, Figure 2.6.

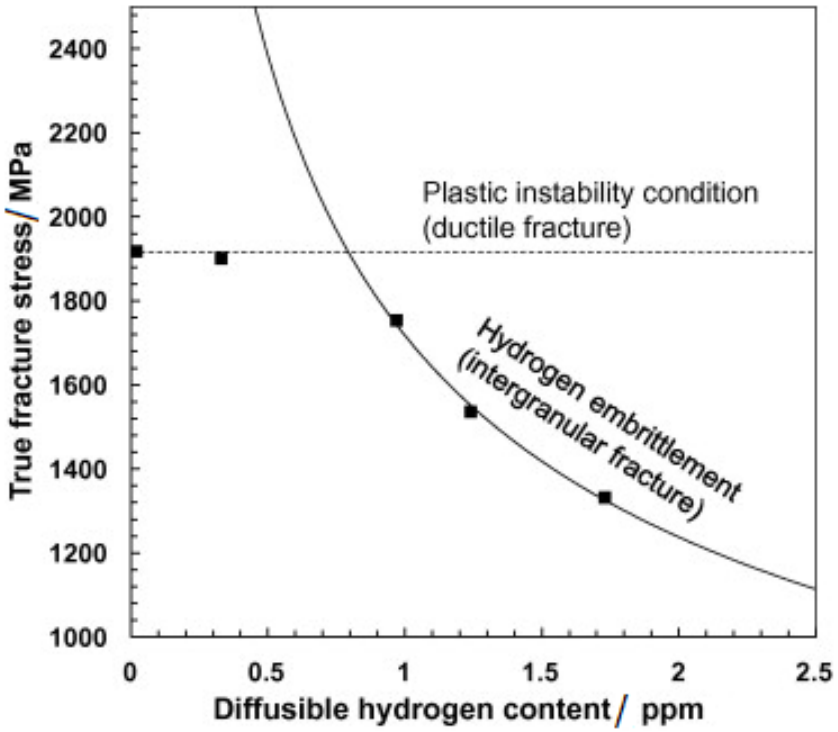

Figure 2.6: The relationship between true fracture stress and diffusible hydrogen content [49].

Martin *et al.* [50] studied the formation and nature of quasi-cleavage fracture surfaces in hydrogen embrittled steels. Quasi-cleavage is a common intermediate fracture mode of hydrogen-induced fracture surfaces that combines characteristics of cleavage and dimpled rupture fractures, Figure 2.7. High magnification scanning electron microscopy (SEM) images of fracture surface showed that quasi-cleavage surfaces are ridges with thin saw-teeth features, Figure 2.8, and are parallel to the crack propagation direction but could shift due to the grain orientation. The ridges were correlated with sub-surface intense and highly localised deformation bands. The bright-field micrograph of surfaces underneath and parallel to ridges faces showed slip planes with high dislocations density, Figure 2.9.

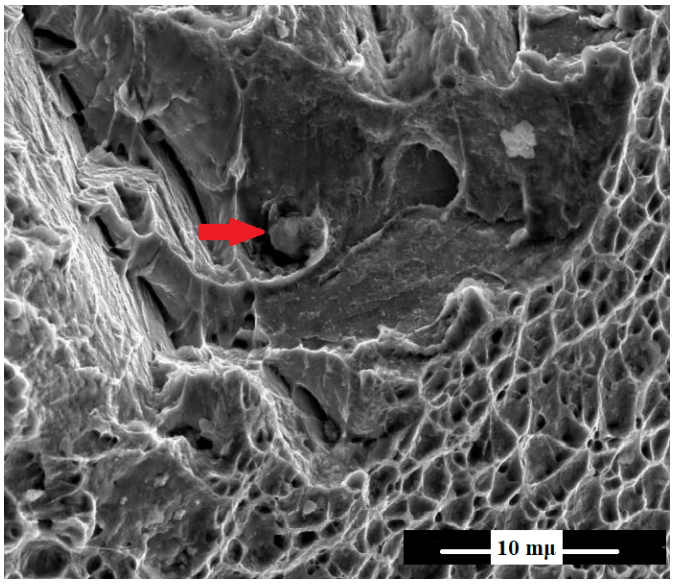

Figure 2.7: Fractography of a low carbon steel showing quasi-cleavage initiated from a MnS inclusion. Red arrow is pointing at a MnS inclusion in microvoid [51].

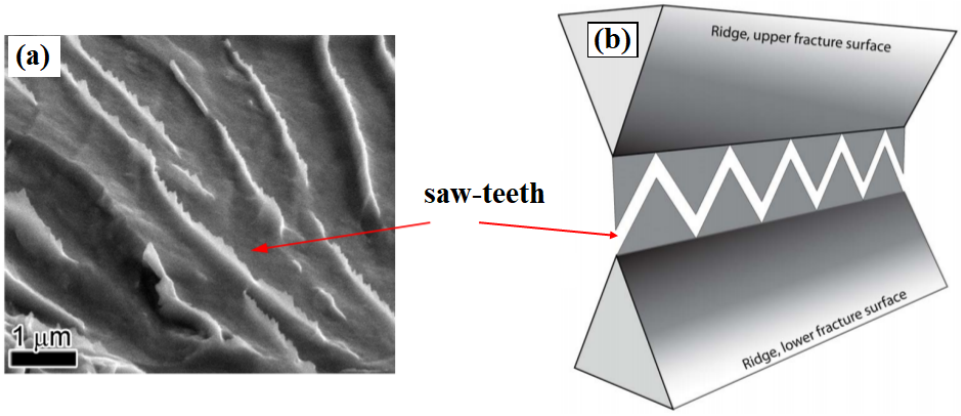

Figure 2.8: a) High magnification SEM image showing the saw-teeth ridges of a quasi-cleavage surface. b) Final separation between ridges produces saw-teeth surfaces [52].

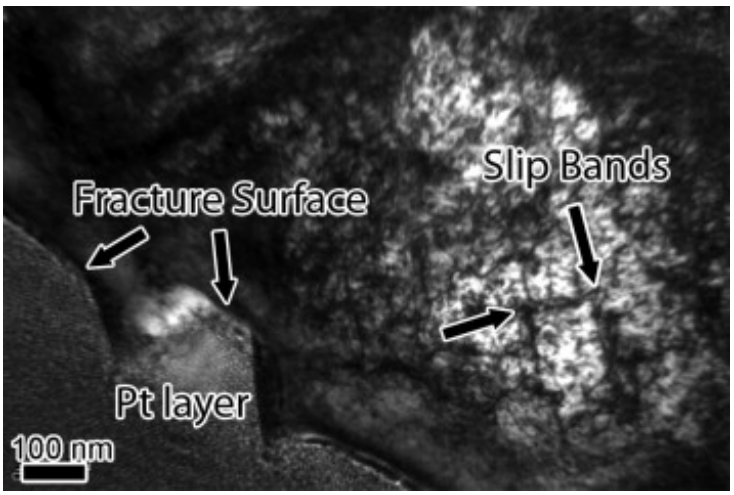

Figure 2.9: Bright-field electron micrograph of the microstructure beneath the ridges on the fracture surface of a martensitic steel [50].

When materials are subjected to cyclic plastic deformation, microcracks initiate along slip bands (dislocation slipping within individual grains, but they cannot go across grain boundaries), and driven by localised stress fields formed as a result of dislocation pile-ups. A similar mechanism applies for hydrogen embrittlement [53]. In regions of high hydrogen concentrations, hydrogen accumulates in the stress field of dislocations, forming an atmosphere around them. In such a way, hydrogen decreases the equilibrium dislocation spacing while simultaneously increases the dislocation mobility, causing a reduction in the interaction energy of dislocations with elastic obstacles [54, 55]. Hence, dislocation interactions occur at lower stress levels than in the absence of hydrogen. Furthermore, hydrogen lowers the stress needed to create the initial voids and accelerate their expansion, resulting in the saw-teeth ridges of a quasi-cleavage surface, Figure 2.10.

Therefore, understanding the microstructural alterations may lead to damage control. Research must be translated into clear guidance accessible to the technologist to optimise microstructure and heat treatment scenarios, which is the purpose of this work.

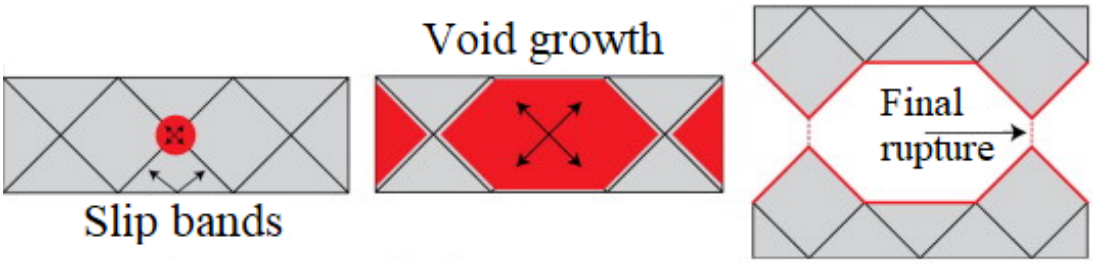

Figure 2.10: Schematic depictions of void nucleation extending along slip band intersections resulting in a fracture surface [50].

2.2 Hydrogen embrittlement of martensitic 100Cr6 bearing steels

100Cr6 high carbon-chromium, 1.0 wt.% C and 1.5 wt.% Cr, bearing steels are mainly used in engines, aircraft, vehicles, fans and machine moving parts, due to their high wear resistance and rolling fatigue strength. Their ability to rotate at high velocities with minimal vibrations, and their excellent hardness, 60 - 67 Rockwell C at room temperature, provides them with long working life, making them suitable for highly stressed applications [56, 57]. However, certain challenges have been recognised with this grade. Bearing steel microstructure preferably consists of $< 10\%$ of nonstabilised retained austenite produced by a controlled heat treatment [58]. During austenitisation, and as the temperature increases, grain size increases and concurrently the area per unit volume of grain boundaries decreases. The grain boundaries become enriched with segregated impurities such as P, S, N, Sb and Sn (enhanced by the presence of Mn and Si in the alloy), causing intergranular embrittlement [14]. Hydrogen promotes grain decohesion when large amounts of impurities segregate at the grain boundaries, causing intergranular fracture [59]. This is because hydrogen has a strong tendency to segregate into structural defects like grain

boundaries and edge dislocations [3].

2.2.1 Microstructural evolution during rolling contact fatigue

Typically, rolling contact fatigue (RCF) cracks start with the initiation and growth of microcracks through a stressed area. The microcracks eventually form surface spalls ending with the ultimate failure of the component, Figure 2.11 [60]. Fatigue cracking of the load-bearing rolling elements develops at or under the surface as shown in Figure 2.12.

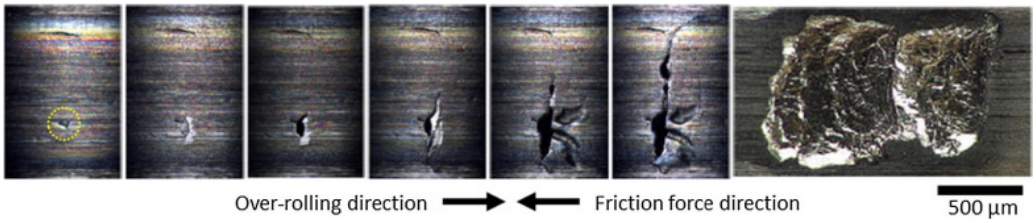

Figure 2.11: Surface crack growth leading to spalling under rolling test [60].

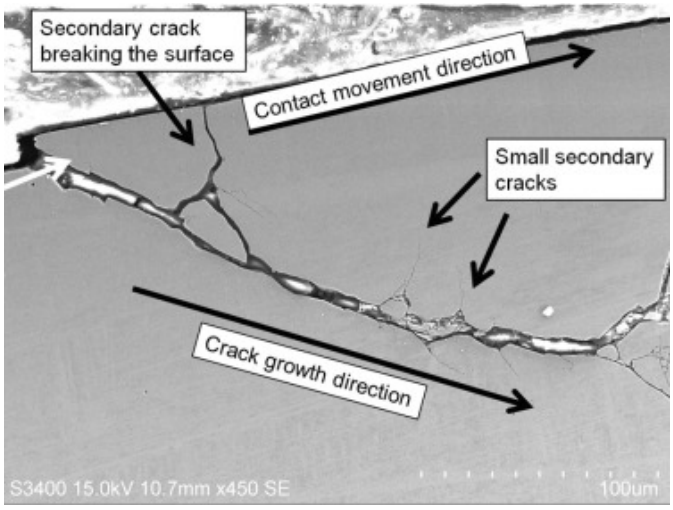

Figure 2.12: SEM image of sub-surface fatigue cracking. Secondary cracks can be seen to branch off the main crack [60].

In martensitic steels, crack initiation during rolling contact fatigue is characterised by microstructural alterations in the form of white etching areas (WEA), dark etching regions (DER) and white etching bands (WEB) [61]. Operating conditions are crucial factors that trigger the formation of such alternations [62]. Figure 2.13 shows fatigue failure in the form of spall formation for elevated temperatures and loads, while Figure 2.14 summarises the microstructural alterations at different number of cycles.

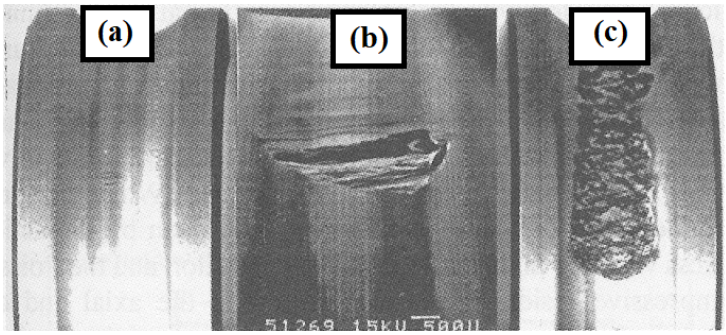

Figure 2.13: Surface fatigue in ball bearings: a) 3.3 GPa at 45 °C for 15 x 10^8 revolutions, b) 4.8 GPa at 55 °C for 2 x 10^8 revolutions, and c) 3.3 GPa at 90 °C for 1 x 10^8 revolutions [63].

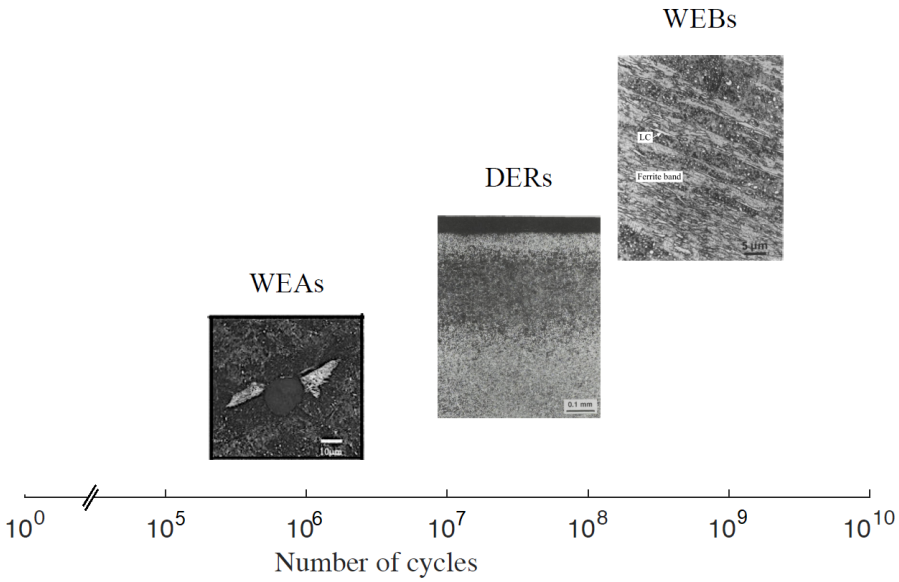

Figure 2.14: Occurrence of different types of microstructural alterations at different RCF stages with respect to number of cycles [64].

White etching areas, also known as butterflies, appear at early stages of bearing life, often after 10^5 cycles [65]. They form around large carbides or non-metallic inclusions (NMIs) such as Al_2O_3 and MnS, and are usually found at certain angle relative to the contact surface [62], $\sim 45°$ to the rolling direction, which correlates to the maximum shear stress under Hertzian contact [66]. WEAs, Figure 2.15, always appear in pairs either on both sides of inclusions or carbides, or only at one side of a crack [67]. WEAs are thought to be responsible of 5 to 10 % failures of the calculated L_{10}[1] life as a network of cracks known as white etching cracks (WEC) can nucleate from them reducing fatigue life [68].

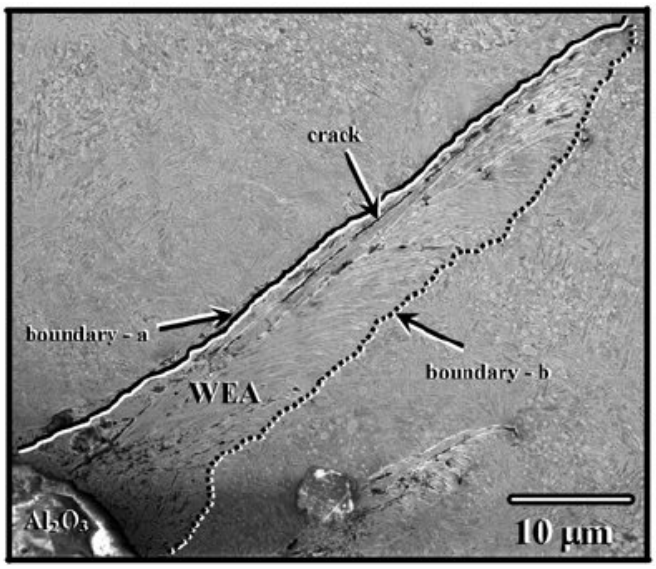

Figure 2.15: SEM image of one butterfly around an Al_2O_3 inclusion. The image shows two types of boundaries: boundary-a with a crack, and boundary-b without a crack [67].

Dark etching regions start to form after around 10^7 to 10^8 cycles. The size of DER increases with increasing stress cycles as a result of cyclic plastic deformation of the original martensitic microstructure [62]. DERs start to form around 100 μm beneath the contact surface reaching their peaks at about 200 μm, after this depth they start to fade until they disappear at 500 μm [69, 70].

White etching bands form after more than 10^8 cycles. They form on top of DERs at

[1] L_{10} value is used to describe bearing life as it relates more to early failures [229]

a similar subsurface depth where DER leans 30° to the rolling direction [62,65,71]. This type is described as low angle bands (LABs). Another type of WEB known as high angle bands (HABs) appears after $\sim 5 \times 10^8$ cycles, inclined 80° to the rolling direction [64]. The two types of WEBs are illustrated in Figure 2.16a, and the geometric relationship between LABs and HABs is in Figure 2.16b.

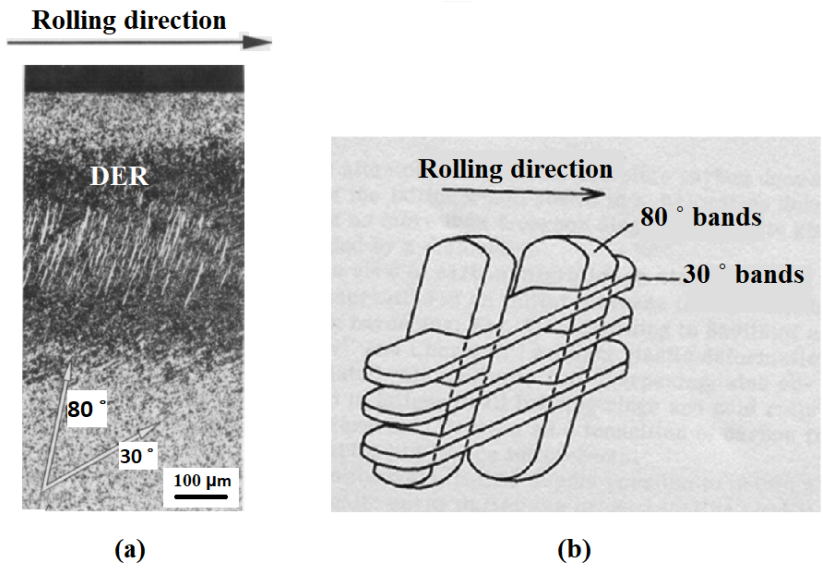

Figure 2.16: a) Optical image taken from 52100 bearing inner ring samples showing 30° and 80° WEBs formed on the top of DER. The sample ran to 10^9 cycles [70]. b) The geometric relationship between HABs and LABs [72].

Effect of inclusions on fatigue properties

In advanced high strength steels, NMIs are considered as a possible source of internal cracks as they generate stress concentrations around/inside them [73], and subsequently accelerate rolling contact fatigue in bearing steels. NMIs in 52100 bearing steels may form voids upon fine grinding when they are removed from the surrounding steel matrix, Figure 2.17a. These voids react as microcrack initiators, and eventually break through the raceway surface which leads to spalling and bearing failure [74], Figure 2.17b.

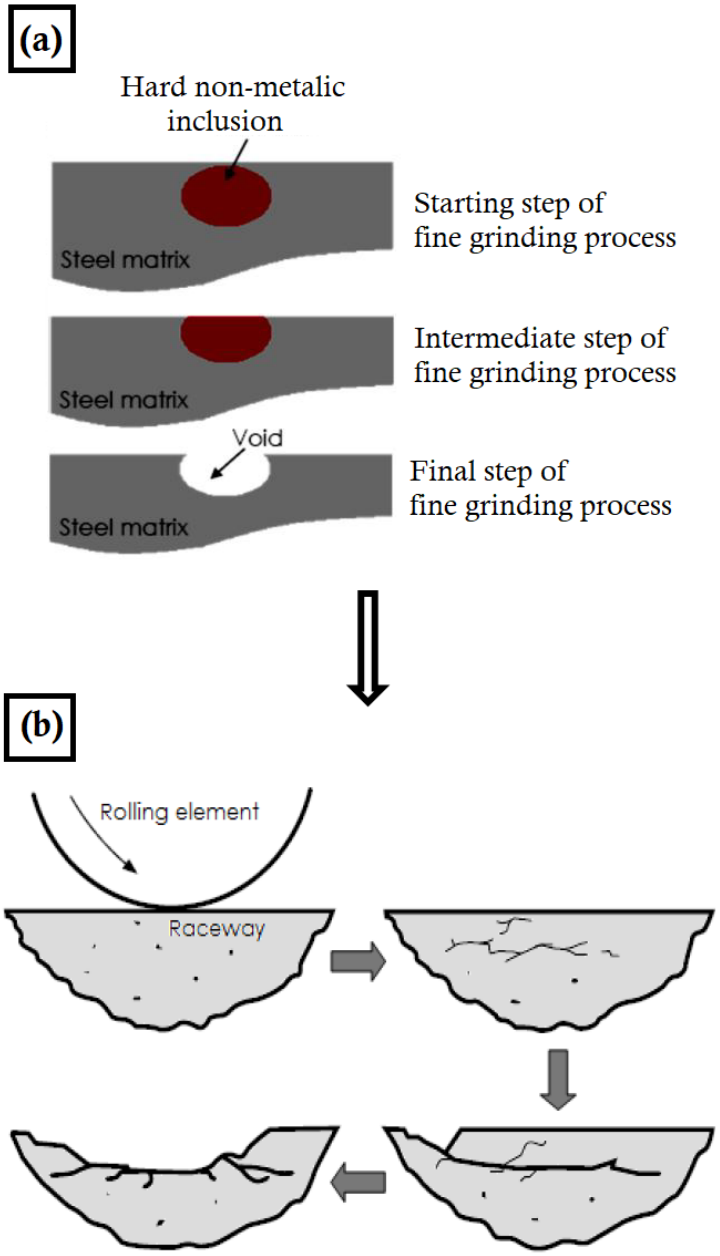

Figure 2.17: a) Voids forming process from a NMI [74]. b) The progressive stages of spalling forming in relation to NMIs [75].

NMIs are either endogenous or exogenous. Endogenous NMIs, such as SiO_2, Al_2O_3 and MnS form during the steelmaking process [76]. Oxygen and sulfur are soluble in the liquid phase of iron but they have very low solubility in the solid phases, therefore, they become rejected to the liquid phase upon solidification and finally form hard separate phases [77]. Exogenous inclusions form as a result of mechanical and chemical corrosion during final finishing operations like heat treatment and deformation processing that may cause surface oxidation, surface sulphurisation or inner oxidation. They are generally larger in size than endogenous inclusions with irregular shape and complex structure [78].

For structural applications, inclusions negatively impact the steel tensile strength and fatigue properties and, needless to say, its hydrogen embrittlement resistance. Stresses around inclusions usually relax during the hot rolling process of the steel. However, following cooling of the steel regenerates tensile residual stresses around the inclusion which is attributed to the thermal expansion coefficients of the inclusion and the surrounding matrix [73]. Later, when the material undergoes deformation at room temperature, stresses increase and voids start to form by matrix/inclusion decohesion or fracture of inclusion particles [79]. Hydrogen also increases NMIs decohesion or cracking when it concentrates in voids around inclusions, and initiating cracks under external tensile loading [80].

Guetard and Rivera-Díaz-del-Castillo [81], observed the formation of oxide inclusions during rolling contact fatigue tests on bearing steels, Figure 2.18. They suggested that an oxide layer formed as oxygen - either from the air and/or the lubricant - entered the material through an initial surface-breaching crack, and with continuous rolling contact, the brittle oxide layer is broken into fragments, followed by the formation of a new oxide layer, sequentially. The oxide formation leads to a local volume expansion which can accelerate the crack propagation.

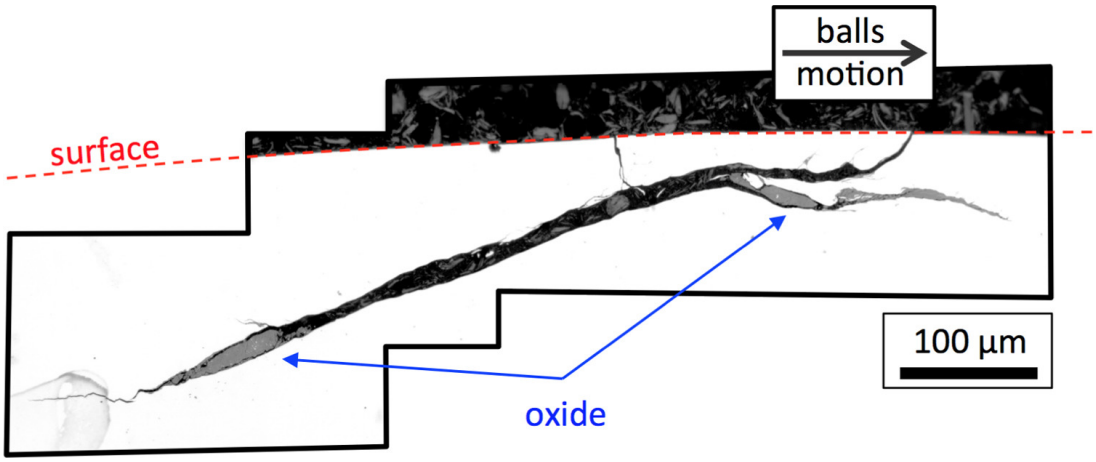

Figure 2.18: Optical micrograph of a 100CrMnMo8 RCF rod section showing oxide near subsurface crack tips (Contact pressure=5.6 GPa, number of cycles= 140×10^6 stress cycles) [81].

In their study on high-carbon chromium-bearing steel, Nakai *et al.* [82] described the spalling mechanism from inclusions. The cracking process observed in their study is summarised in Figure 2.19. Vertical crack forms first from an inclusion that has a length of 30 μm, the crack was also adjacent to the rolling surface. Under normal stress, the crack propagates vertically in the depth until reaching a critical depth of $\sim$ 50 to 60 μm when the horizontal crack starts to form parallel to the rolling surface. The horizontal crack propagates under shear stress and eventually forms a spall. The depth where the shear stress had the maximum value was 67 μm which indicates that the formation and propagation of horizontal crack is controlled by shear stresses.

Steel cleanliness is of vital importance in the development of high quality bearings with excellent operating performances [74], and in order to attain clean grades it is important to control and improve operating applications during the steel manufacturing process, such as deoxidisation, alloying additions, heat treatments and casting activities [74, 83]. A steel is considered clean if the content of impurities such as aluminum, sulphur or sil-

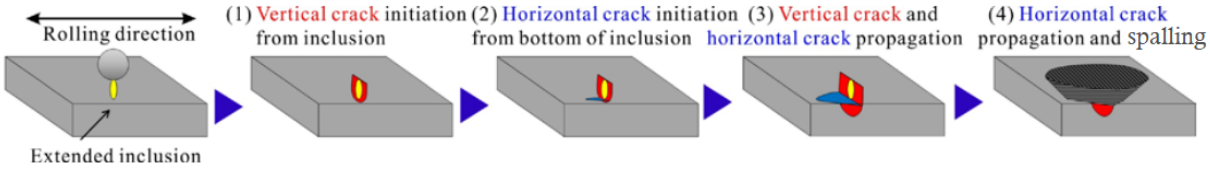

Figure 2.19: Spalling mechanisms from extended inclusion [82].

icon is very low, because these impurities form NMIs in combination with oxygen [84]. Today, new clean steels with very low oxygen (< 10 ppm) and sulfur (< 10 ppm) contents have been developed by steel producers with remarkably improved mechanical properties like fatigue strength and corrosion resistance [85]. Nonetheless, the driving mechanism of RCF failure in the presence of hydrogen and its interaction with NMIs remains controversial, although it is widely acknowledged that under cyclic stresses, hydrogen can enter the bulk of high strength steels causing a sudden RCF failure driven by crack propagation as hydrogen diffuses into the lattice and accumulates at the tips of microcracks that already been initiated from NMIs. More details of this phenomenon is discussed in the next section 2.2.2.

2.2.2 Rolling contact fatigue in the presence of hydrogen

Under constant load, high-strength engineering materials undergo a severe failure as a result of hydrogen-induced delayed fracture, during which the time to failure significantly decreases as the hydrogen content increases. Vacancies are thought to form due to hydrogen/dislocation interactions and act as trapping sites for hydrogen [86]. Moreover, in steels containing NMI like TiN and Al_2O_3, hydrogen was found to enhance decohesion and cracking as it concentrates in the voids around inclusions, and under tensile loading, voids grow due to high hydrogen concentration causing embrittlement [80].

When hydrogen is present in a bearing steel, clusters of WECs form during bearing operation as hydrogen accelerates butterfly formation and growth causing damage to occur at lower bearing load levels. This is more likely to happen in the steel matrix adjacent to oxide inclusions. WECs continue to grow deeper below the raceway surface until they reach considerable sizes before they eventually find their ways to the raceway surface and trigger spalling failure. This was not observed in hydrogen-free bearings that were tested under the same conditions which led to the conclusion that hydrogen in bearings steels has a strong effect on fatigue life [87].

The effects of hydrogen on microstructural changes and rolling contact fatigue life of hydrogen-charged bearing steels were investigated under clean lubrication conditions by Uyama *et al.* [88]. Subsurface cracking occurred with white structures formed causing reduction in the rolling contact fatigue life as the hydrogen content increased. WEAs were formed adjacent to the area of cracking in the hydrogen-charged specimens. Transmission electron microscopy (TEM) observations Figure 2.20 showed that WEA consisted of an ultra fine grained structure which is suggested to be part of a dislocation structure which changed during cyclic plasticity. There were no microstructural changes observed in the areas adjacent to the these structure, which suggested that the localised microstructural changes were caused by hydrogen and that the role of hydrogen in the process of rolling contact fatigue is to localize plasticity.

Rolling four ball tests conducted on hydrogen charged AISI 52100 lubricated with mineral oil showed that fatigue life is inversely proportional to the hydrogen content in the steel [89]. Therefore, it is of critical importance to consider a new strategy to improve hydrogen embrittlement resistance in high strength bearing steels. One remarkable approach is the use of hydrogen traps in steels in order to immobilise the diffusible hydrogen.

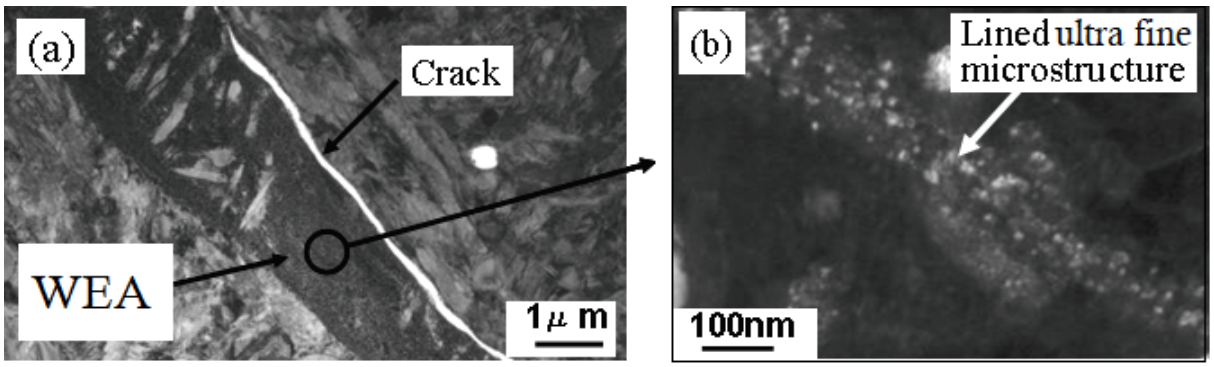

Figure 2.20: TEM images showing: a) white-etching area adjacent to a crack, b) ultra fine grained structure in WEA [88].

2.2.3 Hydrogen trapping phenomena in high strength steels

Several fundamental studies have been carried out on trapped hydrogen. It has been proved that alloy carbides significantly mitigate hydrogen embrittlement susceptibility of steels because they act as traps that tie up diffusible hydrogen which is thought to contribute to hydrogen embrittlement. Hydrogen that enters into steel is inhomogenously distributed either in the lattice interstitial positions, or in microstructural defects such as dislocations and grain boundaries [90]. In general, traps are classified into two categories: (1) shallow traps with low trapping (binding) energy. Due to their low energies, they are considered as reversible traps. Examples of these include dislocations, grain boundaries and coherent precipitates. (2) Deep traps with high trapping energy in which hydrogen atoms are strongly bonded and no longer contribute to the diffusion process. Retained austenite and incoherent precipitate traps fall under this category [91, 92].

Pressouyre and Bernstein [93] found that titanium carbide particles act as strong hydrogen traps, and, with a binding energy of 95 kJ mol^{-1}, they are considered irreversible traps at room temperature. In addition, Yoshino [94] found that fine coherent carbides

such as vanadium, molybdenum and niobium carbides are highly efficient in increasing the stress corrosion cracking resistance. Aoki and Tanino [95] found that vanadium carbides V_4C_3 in low carbon steels containing > 0.10 wt.% vanadium were coherent and formed parallel to $\{100\}$ planes in the iron matrix.

Generally speaking, smaller and globular carbides are preferable for hydrogen trapping, while large grain sizes are deleterious because they provide lower grain boundary area, thus fewer trapping sites. In addition, stable carbides that do not dissolve and re-precipitate during elevated temperature service prevent the segregation of undesirable impurities, and therefore inhibit the formation of local hydrogen concentrations which will later increase the susceptibility to hydrogen embrittlement [96].

Role of vanadium carbides in hydrogen trapping and mechanical properties enhancement of a high strength steels

Primarily, vanadium is added to steel for grain size refinement. Vanadium carbide precipitates are very stable and do not dissolve below 1200 °C [97], which is above normal service temperatures. At high temperatures such as 1050 °C, vanadium tends to form vanadium nitrides (VN). These nitrides preferred nucleation sites are the austenite grain boundaries and they therefore pin (restrict) the prior austenite grain coarsening. The mechanism by which the grain boundaries are pinned by second phase carbide particles is known as Zener pinning [98–100]. The level of precipitation strengthening at a given vanadium content depends on the carbon and nitrogen content in the alloy [101].

Fine vanadium carbides precipitate coherently within the steel lattice. Their distribution scatters hydrogen, therefore, hydrogen atoms do not concentrate in one area raising the resistance to hydrogen-induced damage [96].

It has been reported that adding vanadium with a proper heat treatment process enhances not only the mechanical properties of high strength steels but also their resistance to hydrogen embrittlement [102]. A remarkable decrease of hydrogen embrittlement in vanadium-added steels has been shown in atmospheric exposure tests. This is, according to Yamasaki and Takahashi [103], because hydrogen is trapped by V_4C_3.

However, hydrogen trapping properties are influenced by different parameters, but the most significant two are the carbide size and their number density [104]. Literature reports stated that the preferable V_4C_3 precipitate size to trap hydrogen is $\sim$ 10 nm diameter where the total precipitate/matrix interfacial area is large, therefore, the trapping potential is maximum [105, 106].

The exact location of hydrogen, whether trapped at the carbide/matrix interface or within the carbide, is still controversial among researchers. A recent attempt to reveal that was by charging a bearing steel needle-geometry specimen that contains V-Mo-Nb carbides in its ferrite matrix, with deuterium to mimic a high hydrogen concentration, followed by atom probe tomography (APT) analysis [107]. Composition profiles were collected from each particle (and surrounding matrix) along the Z-axis of the particle. The results showed deuterium restriction to the interior of the carbide which means, according to the authors, that hydrogen is trapped in the core of these carbides. They claimed that the single profile shown in Figure 2.21 reaches a maximum before decaying, and if hydrogen was restricted to the interfacial region at the surface, the profile would have appear in a U-shape, which is clearly not the case in the data presented in their work [107].

Almost all steels are exposed at one time or another to hydrogen embrittlement, but hydrogen trapping behaviour becomes more complicated in multi-phase steels because

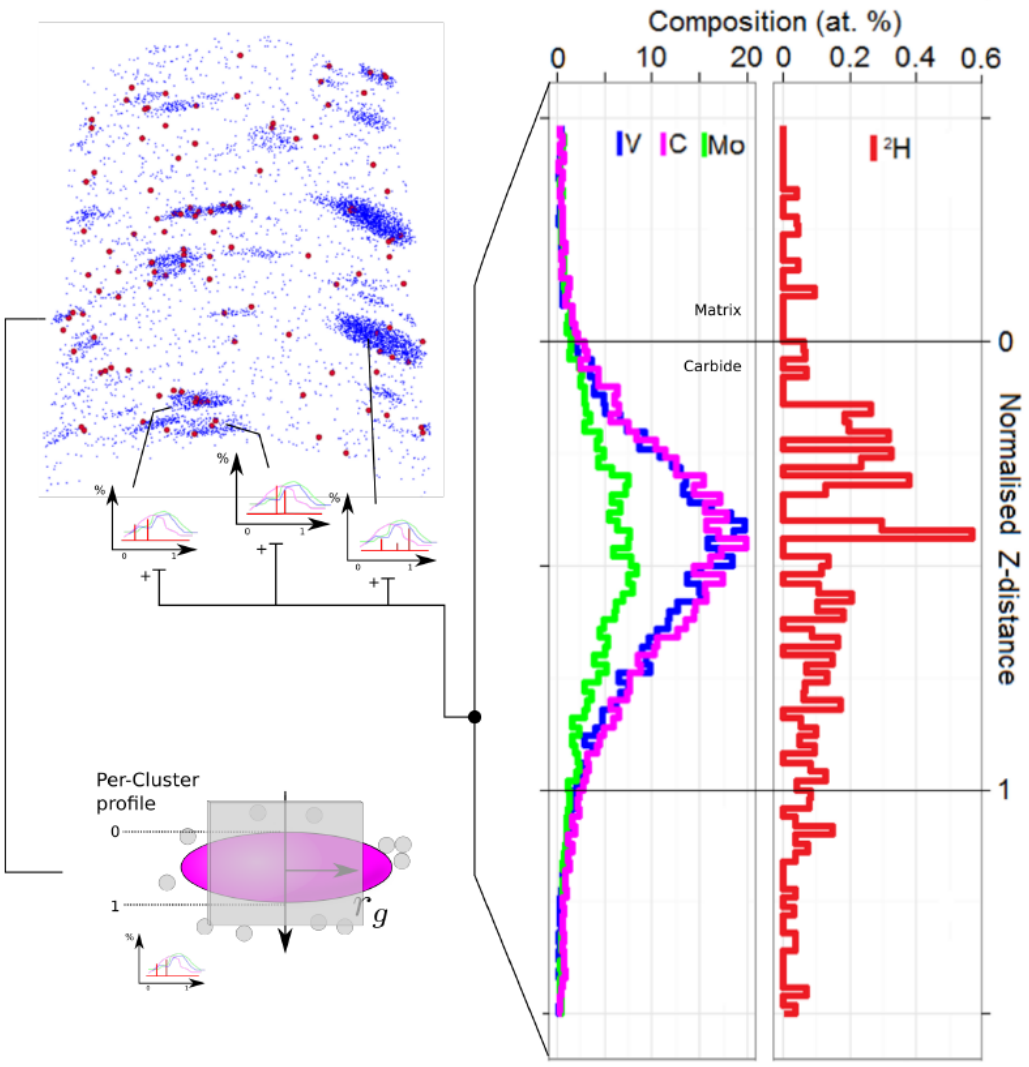

Figure 2.21: Combined analysis of deuterium charged carbides. Superimposed profile of carbides, generated by normalizing and combining multiple individual profiles from each vanadium carbide ($>$ 100 atoms). Resultant profile shows deuterium within the carbide, at $\approx$ 0.5 at% concentration. Atom map shows approx 10 nm slice through dataset [107].

trapping sites include not only defects like carbides and dislocations, but also different fractions of microstructural constituents such as retained austenite. The next section will discuss in more detail hydrogen embrittlement in multiphase TRIP steel.

2.3 Transformation-induced plasticity (TRIP) steels

TRIP steels emerged at 1987 by Matsumura *et al.* with a microstructure consisting of 50 - 60 vol.% allotriomorphic ferrite, 20 - 30 vol.% bainite and the remaining percentage being retained austenite and some martensite, Figure 2.22 [108]. It was primarily designed for the automotive industry with an outstanding combination of strength and ductility [109].

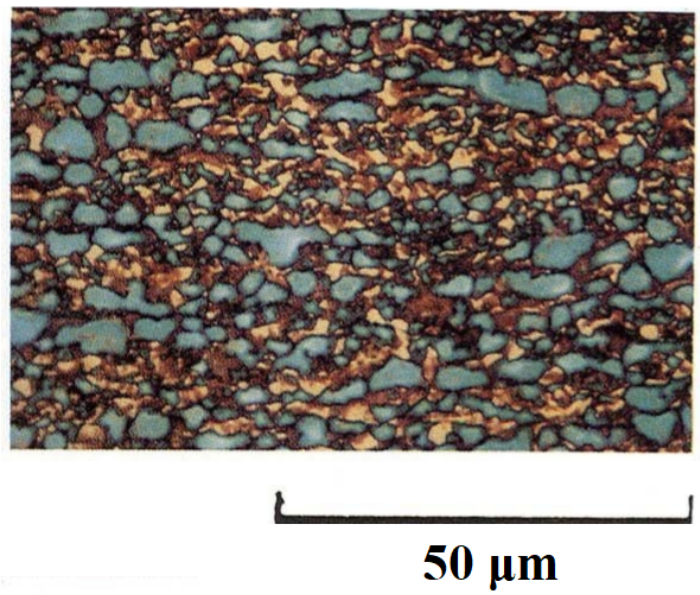

Figure 2.22: Optical microscopy showing the microstructure of TRIP steel developed by Matsumura *et al.* (blue: ferrite, brown: bainite, and white: retained austenite). [108].

Later, it was developed to contain 10 - 30 vol.% austenite [111, 112]. The role of austenite is very important as it boosts the ductility through the TRIP effect [113–116]. During plastic deformation, it transforms into martensite providing the steel with high

hardening, and with the presence of a high volume fraction of ferrite, both phases provide the material with high plasticity raising its elongation (transformation induced plasticity effect) [117].

Although a large volume fraction of retained austenite is believed to enhance both the elongation and the ultimate tensile strength of TRIP steels [118] it could, however, reduce the bainite formation resulting in a loss of strength [119]. The relative fractions of individual phases dominate the mechanical properties of TRIP steel, especially the fraction of retained austenite [120–122].

Moreover, elongation can be affected by temperature because it is a key factor in the stability of retained austenite, therefore on the transformation induced plasticity [123]. Austenite to martensite transformation takes place in two ways. The first is upon quenching to martensite start temperature (M_s), where the cooling process time scale is insufficient for carbon diffusion to start. The transformation driving force increases when cooling continues below M_s. The second way of transformation is by external stresses [124], and takes place above M_s where the stress supplies the driving force needed for austenite to martensite transformation.

Martensite formation is dominated by the mechanical driving force generated through external stresses U. Applied stresses compensate for the thermodynamic driving force needed for the reaction to start above M_s [125]. Considering that $\triangle G_1$ is the critical driving force available at M_s, T_1 is a temperature above M_s where the transformation is taking place, and $\triangle G_2$ is the amount of driving force needed for transformation at T_1 (where $\triangle G_2 < \triangle G_1$), Figure 2.23, therefore martensite can form at T_1 if the following condition (eq. 2.1) is met [126]:

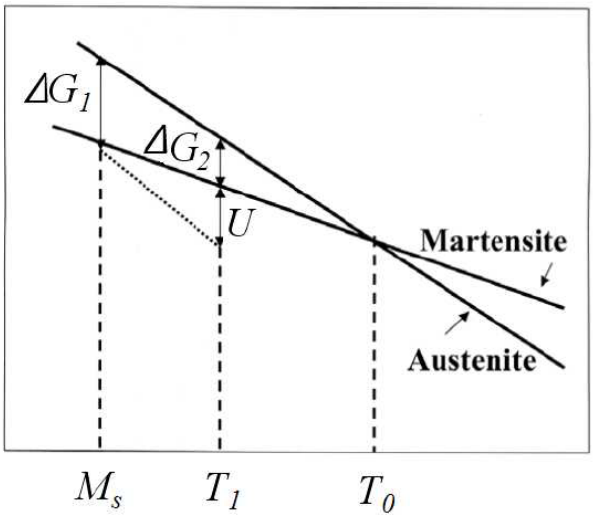

Figure 2.23: Martensitic transformation above the M_s temperature by applying external stress (U). T_0 is the temperature where ferrite and austenite of identical chemical composition have the same free energy [127].

$$U + \triangle G_2 = \triangle G_1 \tag{2.1}$$

Today, with the increasing demand for lighter and higher strength steels, TRIP steels are made through a fundamental heat treatment to obtain the desired mechanical properties by ensuring appropriate volume fractions of individual phases and stabilised retained austenite to produce the TRIP effect [117]. This heat treatment consists of two stages, intercritical annealing and bainite isothermal transformation [125], Figure 2.24. The purpose of intercritical annealing stage is to obtain a ferrite and austenite ($\alpha + \gamma$) microstructure with the austenite having a considerable carbon enrichment [109], thus enhancing hardening. Followed by controlled cooling to the bainitic transformation region for the retained austenite to transform to bainitic ferrite during continuous heating at a moderate temperature [117].

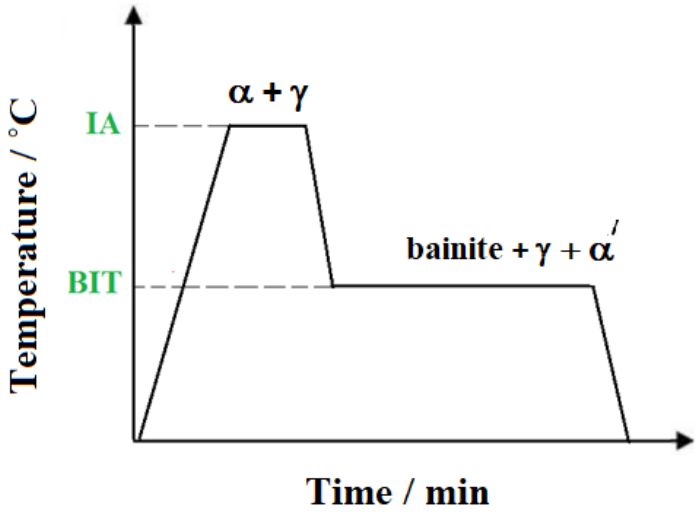

Figure 2.24: General heat treatment diagram of TRIP steel consisting of two stages: intercritical annealing (IA) and bainite isothermal transformation (BIT). α: ferrite, γ: austenite, and α': martensite.

Prolonged heating at this temperature increases the amount of retained austenite that decomposes to bainite [127]. Retained austenite in TRIP steel occurs due to an incomplete bainitic transformation [128]. Bainitic growth is known to be a diffusionless process, it continues by consecutive nucleation of bainite until the carbon concentration of the retained austenite reaches the value where the free energy of bainite becomes less than that of retained austenite of the same composition. Because the transformation ends before the carbon concentration of retained austenite reaches the equilibrium value, the excess carbon is partitioned to the surrounding austenite soon after the diffusionless growth of a bainitic ferrite is over [129]. Bainitic isothermal transformation microstructural evolution is illustrated in Figure 2.25 [130].

TRIP microstructure often contains two types of retained austenite. The first type is a carbon enriched austenite films located between ferrite plates [131] and it is more stable during deformation [132]. The second is a blocky austenite isolated from bainite and is

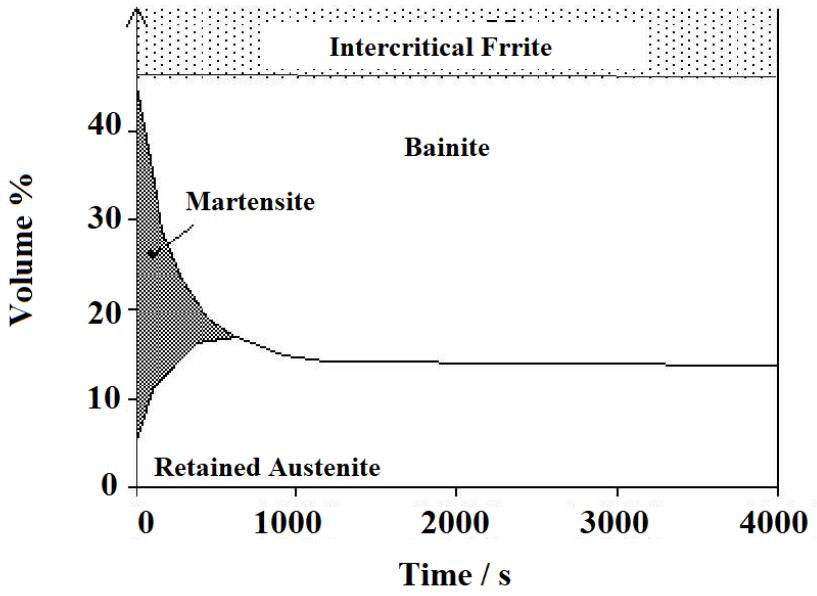

Figure 2.25: Typical microstructural evolution during bainite reaction [130].

not rich in carbon [133], this type transforms first during deformation and it is thought that it is the austenite type that contribute to the TRIP effect.

Ferrite plates that form bainite are called sub-units. They are separated by untransformed (retained) austenite. Sub-units, together with austenite, form what is called sheaf, Figure 2.26. Bainite grows by fresh sub-units which nucleate at the tip of the pre-sub-units [128].

When designing TRIP steel alloys, alloying elements such as manganese, silicon, and aluminum are carefully chosen in order to attain improved properties. Manganese stabilises austenite, while silicon restrains precipitation of cementite helping to retain carbon enriched austenite [111,134]. Likewise, aluminum suppresses cementite precipitation [135] but does not strengthen ferrite as silicon does [136,137].

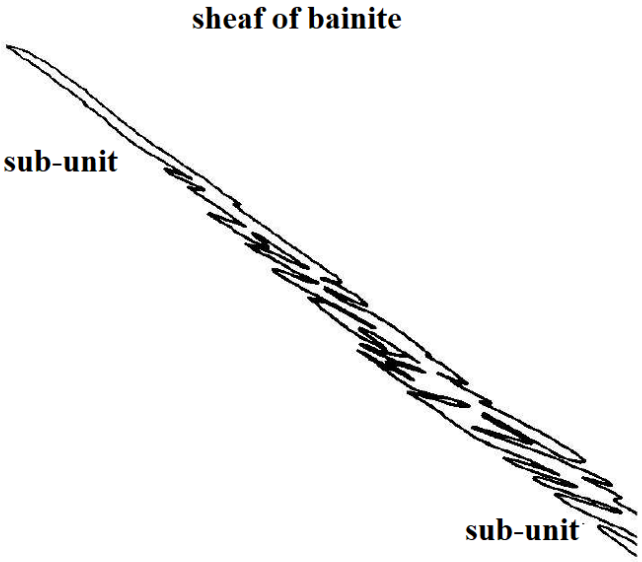

Figure 2.26: Sub-units and sheaf of bainite [128].

2.3.1 Hydrogen embrittlement in TRIP steels

Hydrogen is known as a deleterious agent for martensitic alloys [138, 139]. Moreover, austenite to martensitic transformation increases diffusible hydrogen in steels because trapped hydrogen in retained austenite escapes and diffuses with high mobility [140], which assists continuous crack propagation by accumulating at the crack tip [141,142]. Hydrogen diffusivity increases exponentially after cold deformation of metastable austenitic stainless steels as a result of martensite formation, Figure 2.27 [143].

Hydrogen diffusivity and solubility varies between ferrite (bcc) and austenite (fcc) due to their different crystal structures [144]. Its diffusivity in ferrite is 3 to 4 orders of magnitude greater than in austenite at 50 °C (323 K) [145], and 10 to 1000 times more soluble in austenite than in ferrite [144, 146]. On the other hand, martensite has a hydrogen diffusion rate between that of austenite and ferrite as the hydrogen diffusion coefficient is 2 to 3 orders of magnitude lower than the diffusion coefficient in ferrite

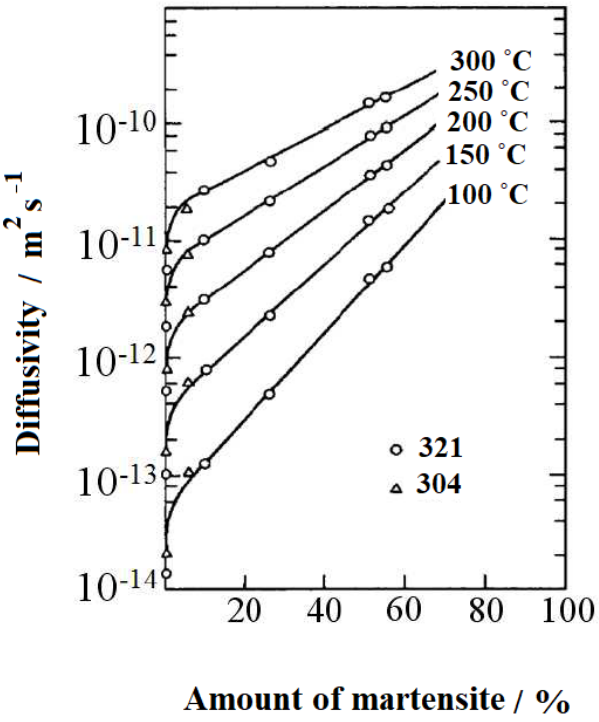

Figure 2.27: Effect of martensite fraction on hydrogen diffusivity on cold rolled 321 and 304 stainless steels [143].

[147, 148], which could have a significant role in the slower release of hydrogen from the martensite phase of TRIP steel. According to this, hydrogen is supposed to become strongly trapped in martensite. It is noteworthy to mention that hydrogen is expected to be inhomogeneously distributed in TRIP steel microstructures due to its multi-phase feature and may be trapped in either reversible or irreversible traps [149]. Traps with activation energies less than 60 kJ mol^{-1} are classified as reversible hydrogen traps, such as grain boundaries, dislocations and microvoids with binding energies 17.2, 26.8 and 35.2 kJ mol^{-1}, respectively [150]. Above 60 kJ mol^{-1}, traps are classified as irreversible hydrogen traps such as MnS inclusion that has a binding energy of 72.3 kJ mol^{-1} [151].

The influence of hydrogen on the mechanical properties and fracture behaviour of martensitic advanced high strength steels was studied by Venezuela *et al.* [152], 20 % static stress of the yield strength was applied to a 24 hours hydrogen charged specimen.

The experiment resulted in a decrease in the yield stress and ductility, and in a change at the fracture mode from ductile to brittle shear fracture. The deterioration was attributed to solid solution softening by hydrogen resulting from a dynamic interaction of hydrogen with the dislocation substructure. The authors suggested that the interaction process is similar to the HELP mechanism for sub-critical crack growth influenced by hydrogen.

Another study on the mechanical properties of TRIP steels was performed by Duprez *et al.* [153]. They compared the steel behaviour at hydrogen free, immediately after hydrogen charging, and one week after charging. The steel lost its ductility immediately after charging. Though, when the specimens were kept at room temperature for one week after hydrogen charging to remove diffusible hydrogen, the researchers found that a large part of the ductility was regained, Figure 2.28. They concluded that the ductility loss was caused by mobile hydrogen present in the steel just after the charging.

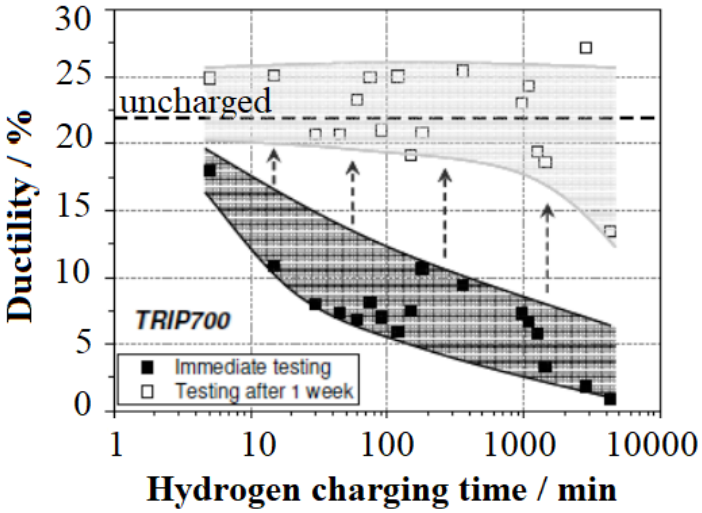

Figure 2.28: Ductility evolution as a function of hydrogen charging time for immediate tensile testing and one week after hydrogen charging [153]. Dashed line indicates the ductility level of the uncharged specimen.

Ronevich *et al.* [154] found that approximately 50 % of the total elongation of TRIP

steels was lost at low quantities of hydrogen, i.e., 1 to 2 ppm. This was attributed to the embrittlement of strain-induced martensite formed during deformation. Most of the ductility was regained when specimens were aged at room temperature for 24 hours after charging [154]. Likewise, a study was done to examine the effect of hydrogen on TRIP 980 steel [155]. A noticeable decrease in the ductility was found with increasing hydrogen content, Figure 2.29. Fractography analysis showed an increase of brittle mode associated with increasing hydrogen content as shown in Figure 2.30 [154].

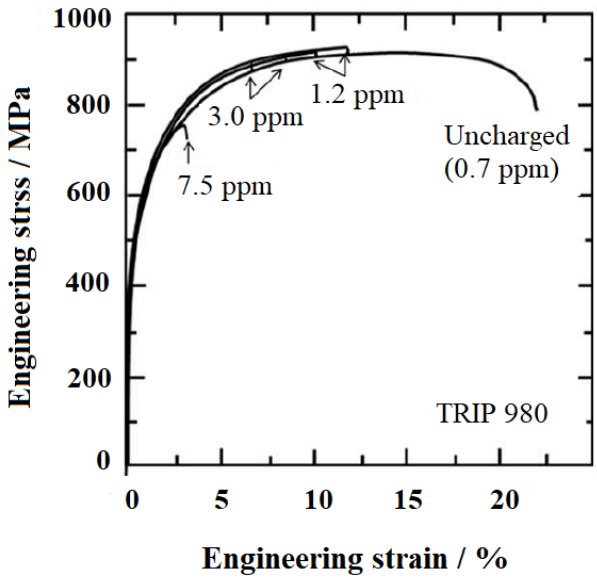

Figure 2.29: The effect of hydrogen on engineering stress-strain curves with the measured hydrogen contents on hydrogen charged TRIP 980 steels [155].

Many researchers reported that cathodic hydrogen charging induced martensite transformation in austenitic stainless steels [156–158], as solute hydrogen can increase the M_s temperature and decrease the stability of austenite [159, 160]. Others [157], however, deduced that hydrogen induced martensitic transformation does not occur in higher stability austenite steels that were alloyed with solutes such as Ni and Mn. Additionally, surface cracking was observed in 304 stainless steel only after hydrogen charging [158].

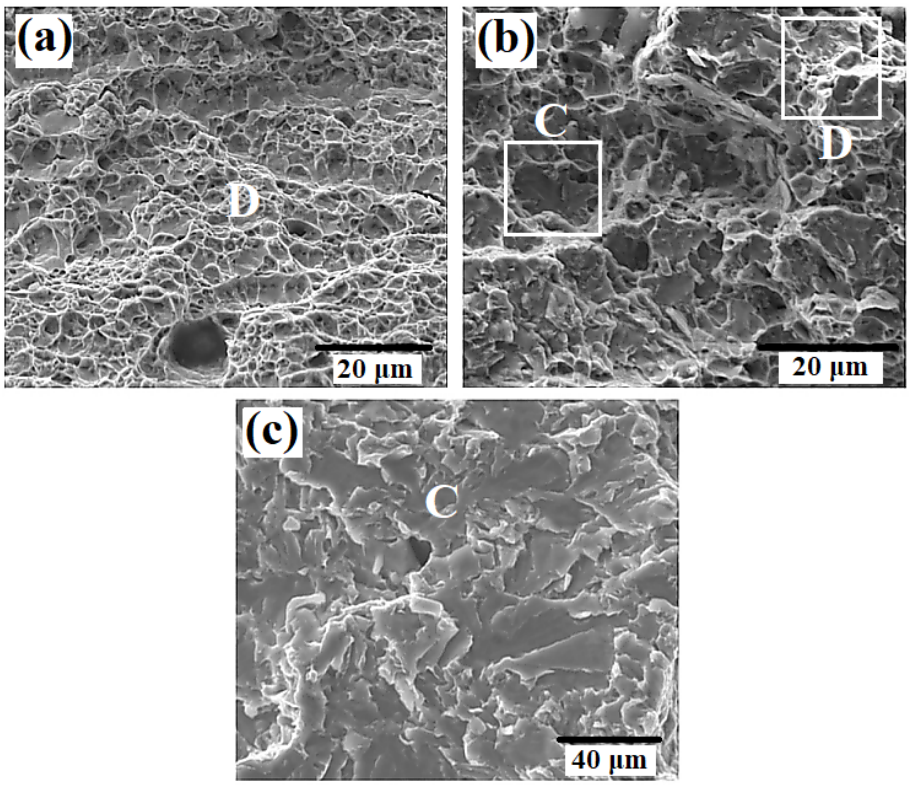

Figure 2.30: TRIP fracture surfaces: a) uncharged, ductile void coalescence, b) 1.2 ppm H, mixed mode of voids and cleavages, and c) 4.5 ppm H, complete cleavage [154]. [D: ductile voids and C: cleavages].

The conclusion was that hydrogen causes mechanical degradation by decreasing the stability of austenite.

A recent study on TRIP steel using electron backscattered diffraction (EBSD) revealed that the crack initiation mechanism is dominated by decohesion of martensite/martensite interfaces. 85 % of crack initiations occurred in or along martensitic regions, Figures 2.31 a and b, and that 15 % of crack initiations were localised at the ferrite/bainite centers, Figures 2.31 c and d, while no cracks were observed along non martensitic grain boundaries [161]. The points where cracks initiate at martensitic islands varied from martensite/martensite interface, martensite/ferrite interface, or passing through the martensite. The study pointed out that the hydrogen which is present in martensite is greater than neighboring phases which are ferrite and bainite for the following reason. After deformation, the fresh martensite will be supersaturated with hydrogen since it formed from transformed retained austenite already containing hydrogen. Moreover, martensite is very prone to hydrogen embrittlement, and when applying stress, this hydrogen-enriched martensite will be very vulnerable to hydrogen induced cracking. Crack propagation occurs when small initiated cracks grow then coalescence to form larger ones. Both HELP and HEDE mechanisms seem to take place in hydrogen-induced crack propagation in TRIP steels. HELP mechanism applies when the growth propagates in the ferrite phase, because crack tips are surrounded by high strain fields. However, HEDE mechanism acts when the crack tip propagates through martensite interfaces or the martensite matrix, causing decohesion of this interface [161].

A mixture of transgranular and intergranular cracking in TRIP steel was observed without applying external load when the material was hydrogen charged [162], and that increasing hydrogen content in the material caused the fracture mode to change from in-

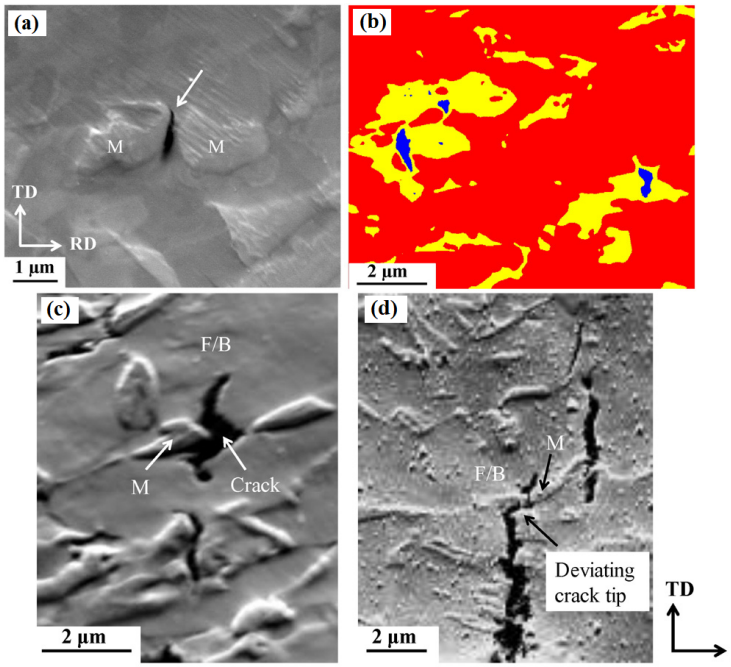

Figure 2.31: Initiating cracks in TRIP steel: a) SEM image of initiating crack (indicated by arrow) between two martensitic regions (indicated by M). b) KAIQ (kernel average image quality) map, where blue is cracks, yellow is martensite, and red are other constituents such as bainite, ferrite or austenite. c) and d) martensite/ferrite or martensite/bainite interface decohesion (M: martensite, F/B: bainite or ferrite) [161].

tergranular and transgranular to only transgranular in automotive advanced high strength steels [163]. It appeared that the fracture mode depends not only on the amount of hydrogen, but also on the amount of brittle martensite present in the TRIP steel [164].

Deformation of TRIP steels not only increases dislocation density but also induces phase transformation of retained austenite to martensite depending on the stability of the retained austenite [165]. Meanwhile, the behaviour of hydrogen in TRIP steels is of great importance since the ductility of such steels is notably affected by the deformation-induced transformation of retained austenite to martensite and, in this context, TRIP steels can aid in understanding the effect of austenite transformation in bearing steels due

to its hydrogen release. Therefore, it is of critical importance to consider a new strategy to improve hydrogen embrittlement resistance in high strength steels. One significant approach is the use of hydrogen traps in steels in order to immobilise diffusible hydrogen.

2.3.2 Hydrogen trapping phenomena in TRIP steels

It is well established that retained austenite is a strong trapping site for hydrogen in multi-phase steels [166, 167] because hydrogen has high solubility in austenite, it could increase the resistance to hydrogen embrittlement [168, 169] in TRIP steels. Besides austenite, defects such as grain boundaries and dislocations traps hydrogen in TRIP steels. The challenge here emerged from the fact that the fractions of microstructural constituents change during and after deformation in addition to generating new defects. The role of retained austenite on hydrogen trapping can be revealed via thermal desorption analysis (TDA) for multi-phase steels. Thermal desorption rate was reported to have increased with one large peak appearing in the TDA profile due to the presence of retained austenite that traps more hydrogen [160, 170]. Distribution of hydrogen in different trapping sites and their contributions to changing the desorption curves was not evaluated quantitatively because the desorption from different trap sites, such as retained austenite, grain boundaries and dislocations, overlapped at almost the same temperature interval. Therefore, the effect of deformation on the hydrogen behaviour in the multi-phase steels remained ambiguous over several years [126].

In several cases it was revealed that retained austenite is beneficial in hydrogen embrittlement resistance because it strongly traps hydrogen [171, 172]. Conversely, austenite in TRIP steels is a metastable phase and transforms to martensite during deformation, which is deleterious for the ductility in the presence of hydrogen. Pérez Escobar *et al.* [173]

compared the TRIP grade with pure iron in terms of hydrogen trapping. They observed that TRIP steel held more hydrogen than the pure iron, Figure 2.32, and that deformation of TRIP 700 steel caused a significant increase in the amount of trapped hydrogen. This trend does not exist for pure iron. However, the peak temperature remained the same which indicates that the trapping sites did not change with increasing deformation. It was then concluded that the increasing amount of hydrogen in TRIP steels is probably attributable to the martensite that formed from retained austenite and not from increasing the amount of dislocation density in ferrite.

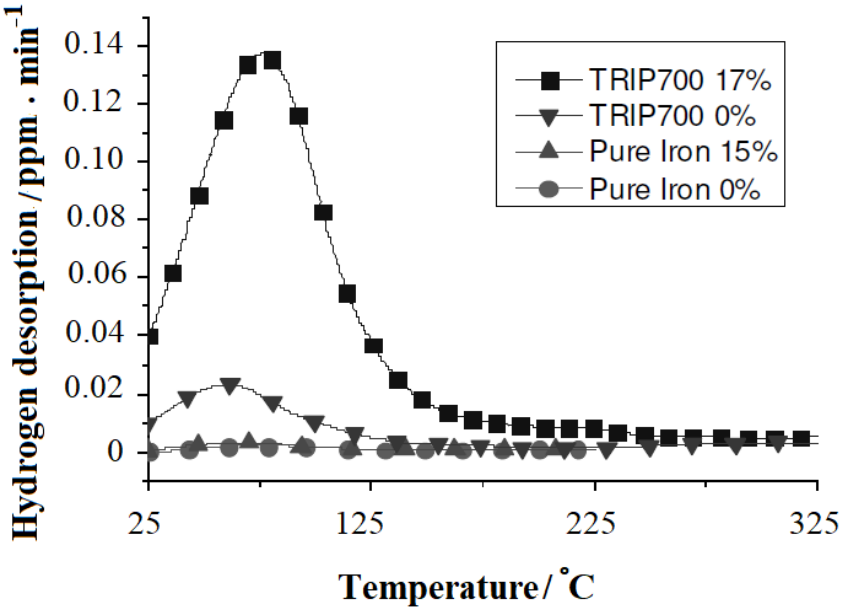

Figure 2.32: TDA results of pure iron, pure iron 15 % deformed, TRIP700, and TRIP700 17 % deformed [173].

In another study, Luppo and Garcia [174] found that as-quenched martensite attracts more hydrogen and acts as weak reversible trapping sites providing new hydrogen sources in the material, which explains the reason why fresh martensite is more susceptible to hydrogen embrittlement. Consequently, hydrogen easily initiates cracks and promotes crack propagation. Pressouyre [175] suggested that hydrogen embrittlement resistance could be

achieved through a uniform distribution of traps to prohibit accumulated hydrogen from reaching critical concentrations that could cause cracking.

2.4 Summary

Bearings are subjected to complex and repeated contact loads during service life, this results in microstructural damage in the form of hard regions of WEAs, DERs and WEBs. These regions are believed to eventually cause early rolling contact fatigue failure. Adding vanadium to AHSS, and in particular bearing steels, provides precipitation strengthening and grain refinement by forming vanadium nitrides and carbides. The final product will offer distinctive properties of strength and toughness as a result of forming V_4C_3 carbides. These precipitates have also a remarkable role on the hydrogen embrittlement resistance because they act as strong trapping sites for diffusible hydrogen, leading to delayed fracture resistance of high strength steels.

There are many issues concerning hydrogen embrittlement and delayed fracture in TRIP steels for automotive applications that must be addressed. TRIP steels are more vulnerable to hydrogen embrittlement due to their multiphase nature. The mechanical deterioration is more pronounced in TRIP steel that contains metastable austenite since it transforms to martensitic during deformation releasing the trapped hydrogen within the material, and yet the role of hydrogen remains questionable and poses several experimental and theoretical challenges.

Chapter 3

Kinetic and thermodynamic modelling

Designing new alloy with an appropriate heat treatment that ensures superior mechanical properties is a complicated procedure involving couplings between multiphysics processes such as heat transfer, phase transformations, and diffusion. Because of the complexity, modeling work for the potential alloys and heat treatments is usually performed before the experimental application, typically, to validate the expected microstructures in the final products and to limit the costs and the time spent in the alloys production. Therefore, the purpose of the kinetic and thermodynamic modelling carried out in this chapter is to design a hydrogen embrittlement resistant TRIP steel for bearing application. The principles of kinetic and thermodynamic calculations are described in the following sections, whereas the experimental applications of the models are described in details in chapter 4.

Modeling of bearing alloys was done with the aid of MatCalc 5.61 software with thermodynamic database (mc_fe_2.023.tdb) and diffusion database (mc_fe2.006.ddb)] [176]. The thermodynamic basis of MatCalc is the CALPHAD method and CALPHAD-type databases [177]. The kinetic modules of MatCalc are developed within the framework of solid-state phase transformation multi-component systems [176].

For TRIP steel, the equilibrium phase diagram for the alloy were calculated in the Department of Materials Science and Engineering, Texas A&M University, using Thermo-Calc® with (TCFE6 v.6.2) database for steels [179]. Thermo-Calc® software is used for thermodynamic and phase equilibrium calculations in unary and multicomponent systems. They are based on thermodynamic data assessed with the CALPHAD technique [177] and incorporate Gibbs free energy minimisation algorithms.

3.1 Principles of thermokinetic modelling

MatCalc precipitation kinetics concepts were founded in a comprehensive multicomponent nucleation module, and in computationally efficient evolution equations for precipitate growth derived from thermodynamic principles [180]. Kampmann-Wagner Numerical (KWN) model is a key simulation approach for non-isothermal second phase precipitation. The model allows to describe nucleation, growth and coarsening of precipitation hardened in metal alloys based on a size distribution for every phase which produces precipitations. More details about the model can be found in Ref. [178]

The typical precipitation from a supersaturated solid solution is a diffusion reaction that involves three stages:

Precipitate nucleation

The number of precipitates increases due to the nucleation of precipitates during the nucleation stage and decreases due to the dissolution of precipitates during the coarsening stage. The steady state nucleation rate J (m^{-3} s^{-1}) - which describes the rate at which nuclei are created per unit volume and time in a binary system- [181] is controlled by

diffusion of micro alloying elements [182] and is given by the classical nucleation theory [180] as:

$$J = ZN_{\circ}\beta^{*} \cdot \exp\left(-\frac{\triangle G^{*}}{k_{\beta}T}\right) \cdot \exp\left(-\frac{\tau}{t}\right) \tag{3.1}$$

where Z is the non-equilibrium Zeldovich factor which quantifies the ability for a nucleus to become destabilised by thermal excitations in comparison to its inactive state [183], $N_{\circ}$ is the total number of potential nucleation sites, β^{*} is the atomic attachment rate taking into account long-range diffusive transport of atoms that is needed for nucleus formation if the chemical composition of the matrix is different from the chemical composition of the precipitate, k_{β} is the Boltzmann constant, T is the absolute temperature, τ is the incubation time, t is the time, and $\triangle G^{*}$ is the nucleation barrier given by:

$$\Delta G^{*} = \frac{f\gamma_{k}^{3}}{F^{2}} \tag{3.2}$$

f is the shape factor of the nucleus ($f = 16\pi/3$ for homogeneous nucleation of spherical nuclei and $f < 16\pi/3$ for heterogeneous nucleation), γ_{k}^{3} is the interface Gibbs energy density, and F is the driving force [180, 181].

In MatCalc, the number of nucleation sites $N_{\circ}$ depends on their type, which includes the bulk, dislocations, grain boundaries, subgrain boundaries, grain boundary edges, and other precipitates. In the case of V_4C_3 and cementite growth, grain boundaries and dislocations are the nucleation sites acting simultaneously [92].

Precipitate growth

MatCalc incorporates the Svoboda - Fischer - Fratzl - Kozeschnik (SFFK) model. Once a precipitate has nucleated, further evolution of its radius and chemical composition is evaluated [92, 184].

In a closed system, under constant temperature and pressure, the independent state parameters q_i (i = 1, . . . , m) can be chosen. Then under several assumptions for the geometry of the system, the total Gibbs free energy G of the system can be expressed by means of the independent state parameter q_i [G = G(q_1, q_2, . . ., q_m)], and the rate of the total Gibbs energy dissipation Q can be expressed by means of q_i and $\dot{q}_i$ [Q = Q(q_1, q_2, . . ., q_m, $\dot{q}_1$, $\dot{q}_2$, . . ., $\dot{q}_m$)], where the dots refer to the time derivative, $\dot{q}_i$ to the kinetic parameters, and m is a fixed number of precipitates [185]. Three dissipative processes are operating during growth of the precipitate: (a) interfacial movement which depends on the interfacial mobility, (b) diffusion inside the precipitate, and (c) diffusion in the matrix, and is influenced by the diffusivity in the matrix [186]. The flux in the matrix is radial, and the precipitate particle lies at the centre of the coordinate system. While the particle grows, the solute amount in the sphere changes and the soft impingement is taken into account indirectly. If Q is a positive definite quadratic form of $\dot{q}_i$, then:

$$\frac{\partial G}{\partial q_i} = -\frac{1}{2}.\frac{\partial Q}{\partial \dot{q}_i} \tag{3.3}$$

If r_k (k= 1, . . . , m) is the precipitate radius and C_i^k is the concentration of component i in the precipitate k, and if both are considered to be the independent state

parameters to give a set of linear equations:

$$\frac{\partial G}{\partial r_k} = -\frac{1}{2}.\frac{\partial Q}{\partial r_k^{'}} \tag{3.4}$$

and

$$\frac{\partial G}{\partial C_i^k} = -\frac{1}{2}.\frac{\partial Q}{\partial C_i^{'k}} \tag{3.5}$$

By solving the previous equations both growth rate of the precipitate $r_k^{'}$, and the evolution rate of its composition $C_i^{'k}$ can be calculated [184].

Precipitate Coarsening

It is described as the dissolution of smaller precipitates in favour of the growth of larger particles as a result of an overall reduction in interfacial energy per unit volume [92]. Dissolution in MatCalc is modelled by creating an artificial heat treatment through which particles are grown into a desired size [184]. Their dissolution can then be simulated by applying an isothermal holding at a high temperature predicted via thermodynamic modelling. The holding temperature is defined as the temperature that the phase starts to become unstable and its Gibbs free energy increases [92]. Equation 3.6 is the linearised form of the Gibbs-Thomson equation used in MatCalc for calculating precipitate coarsening in a closed system of component B:

$$X_B^{M'} \approx X_B^M \left(1 + \frac{2Iv^B}{(X_B^\beta - X_B^M)RT} \cdot \frac{1}{r_k}\right) \tag{3.6}$$

where X_B^M and X_B^β are equilibrium composition of component B in matrix M and precipitate β, respectively, I is the interfacial energy, and r_k is the radius of the precipitate k [180].

3.2 Design and modelling of 100Cr6 steels

Thermodynamic and kinetic modelling performed in this section is directed toward a twofold aim. First: to design a martensitic 100Cr6 bearing steel alloy that is resistant to hydrogen embrittlement with lower vanadium content, and hence, lower treatment temperatures beneficial to optimise industrial processing. Second: to improve the heat treatment of 100Cr6+0.5V alloy that was originally designed by Szost [10,11]. The chemical composition of 100Cr6+0.3V was chosen to produce an alloy similar in mechanical and hydrogen trapping properties to the original 100Cr6+0.5V alloy but with lower vanadium content in order to study the influence of vanadium reduction on the hydrogen trapping efficiency. Therefore, the chemical composition used for 100Cr6+0.3V designing model was similar to that of 100Cr6+0.5V but with vanadium being reduced to 0.3 wt.%, Table 3.1.

Table 3.1: Chemical composition of the investigated steels (wt.%).

Alloy	C	Si	Mn	Al	Cr	Ni	Cu	V
100Cr6	0.97	0.28	0.28	0.042	1.38	0.18	0.21	-
100Cr6+0.3V	0.98	0.16	0.38	-	1.39	-	0.12	0.3
100Cr6+0.5V	0.97	0.26	0.39	0.02	1.48	0.16	0.19	0.49

3.2.1 Design and modelling of 100Cr6+0.3V alloy

The calculations simulated the precipitation of V_4C_3 in the studied steel, assuming local equilibrium and cementite enrichment and dissolution. Figure 3.1 shows the algorithm that was followed to design the heat treatment of 100Cr6+0.3V.

Three temperatures (1040 °C, 1070 °C, and 1090 °C) were selected in the austenite-phase region with different holding times (20, 10, and 5 min) in order to dissolve coarse carbides that formed during casting. Among the three selected temperatures 1090 °C with holding for about 10 minutes was sufficient to completely dissolve the carbides, while with 1040 °C the calculations showed incomplete dissolution of carbides even with the longest holding duration. However, 1070 °C with holding for 20 min was shown to be enough to dissolve the coarse carbides, but latter TEM investigations showed coarse V_4C_3 and cementite in the microstructure with relatively low hardness.

The heat treatment of 100Cr6+0.3V is illustrated in Figure 3.2. It starts with heating the alloy from room temperature (RT) to 1090 °C with a relatively slow heating rate of 1.0 °C s^{-1} during which carbide coarsening continues until dissolution. Slow heating allows carbon diffusion and austenitisation to be achieved (advantage). By reaching 1090 °C, almost all carbides are dissolved (Figure 3.3 point 1). The alloy is held at this temperature for 10 minutes to ensure complete dissolution of carbides from the subsurface to the core and to obtain a homogeneous microstructure. The dissolution stage is ended by quenching to RT to form hard martensite with high dislocation density, and to inhibit the formation of any intermediate phases.

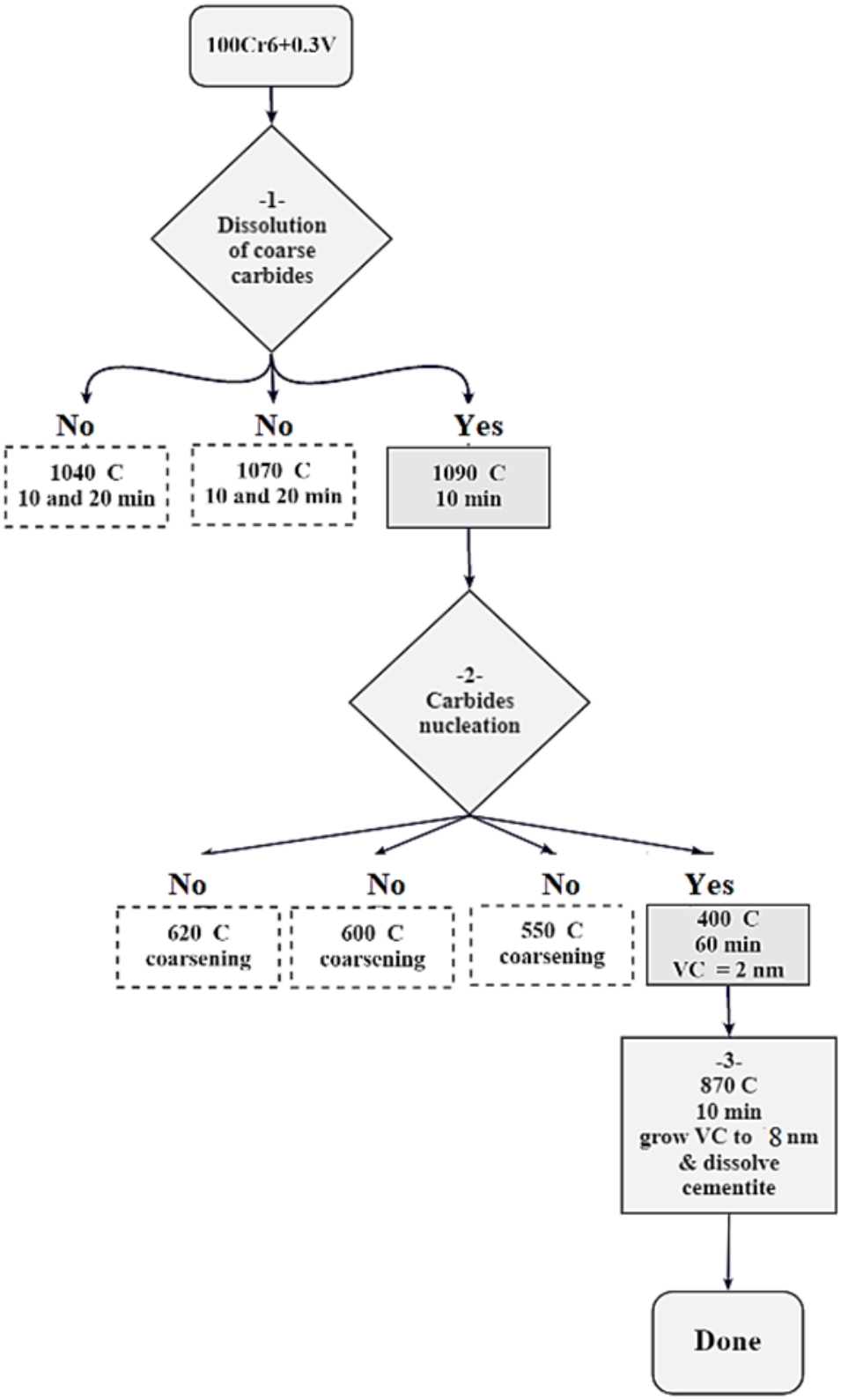

Figure 3.1: Algorithm for investigating the temperatures and holding durations to design a heat treatment for 100Cr6+0.3V alloy.

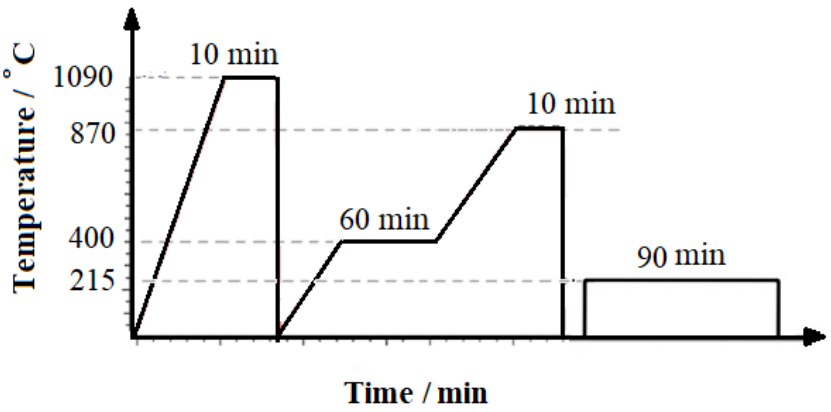

Figure 3.2: A schematic illustration of the new designed 100Cr6+0.3V heat treatment.

The second stage of the heat treatment involves the nucleation and growth of V_4C_3, in addition to dissolve coarse cementite that grows simultaneously with V_4C_3. Several temperatures, heating rates, and holding times were carefully chosen and tested through the model. The temperature was chosen to be in the ferrite-phase region. To start with, 550 °C, 600 °C, and 620 °C were examined but all resulted into coarse V_4C_3 in a very short holding time. An attempt with 400 °C and various holding times were examined and it was found that holding for 60 minutes was sufficient to nucleate a high density of V_4C_3. Accordingly, the alloy was slow heated to 400 °C where the V_4C_3 particles started to nucleate with a very small radius of 1 nm and their number density increased significantly, Figure 3.3 point 2. The alloy was held at this temperate for 60 minutes to increase the population of V_4C_3. At the beginning of the precipitation process stage, which is located between points 2 and 3 in Figure 3.3, the nucleation rate increased steadily, V_4C_3 size increased to $\sim$ 4 nm, and cementite became unstable. It is notable that the V_4C_3 precipitation is synchronous with cementite nucleation, and bulky cementite is not beneficial in advanced high strength steels because it is responsible for initiating fracture [129]. In order to dissolve such cementite a second but slower heating (0.5 C s^{-1}) to 870 °C is required. During this, V_4C_3 grows at the expense of cementite to the required

size for hydrogen trapping, which can be seen between points 3 and 4 Figure 3.3, where stable V_4C_3 precipitates reach $\sim$ 8 nm with a number density of $\sim$ 2 $\times 10^{22}$ m^{-3} and a molar phase fraction of $\sim$ 0.004. This stage ended with quenching to RT. Finally, the alloy was tempered at 215 °C for 90 minutes to reduce the hardness of fresh martensite and to preserve toughness. The obtained hardness is 751 HV30 ($\sim$ 61.8 Rc).

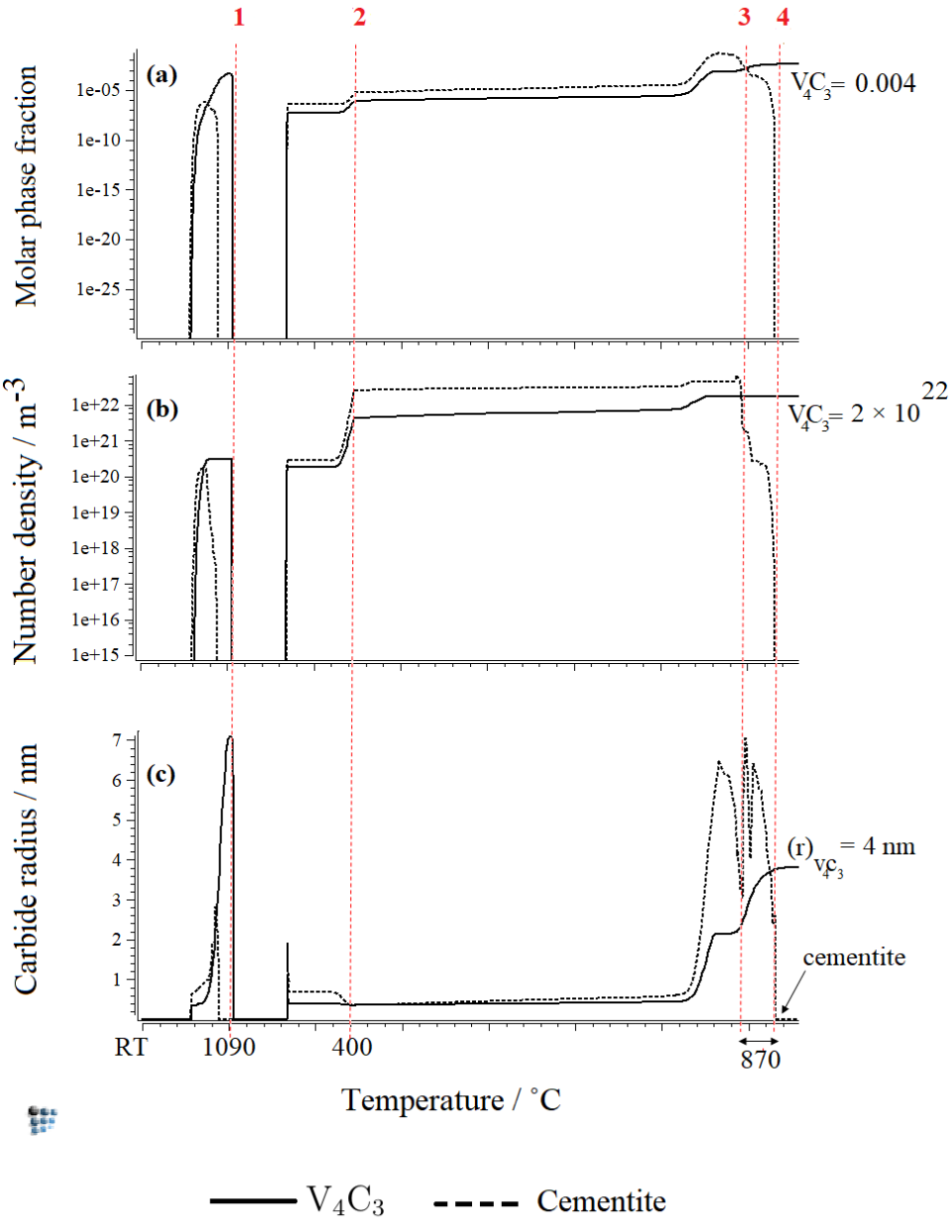

Figure 3.3: Kinetic calculations of carbide evolution during the heat treatment of 100Cr6+0.3V alloy. Carbides: a) phase fraction, b) number density, and c) radius (r).

3.2.2 Heat treatment design for 100Cr6+0.5V alloy

The purpose of this section is to reduce the complexity of 100Cr6+0.5V alloy heat treatment procedure developed in earlier work [92]. Basically, the precipitation kinetics principles and choosing the heat treatment parameters approach are similar to those described in section 3.2.1. Figure 3.4 represents the original heat treatment of 100Cr6+0.5V alloy [10, 11] alongside the newly designed one.

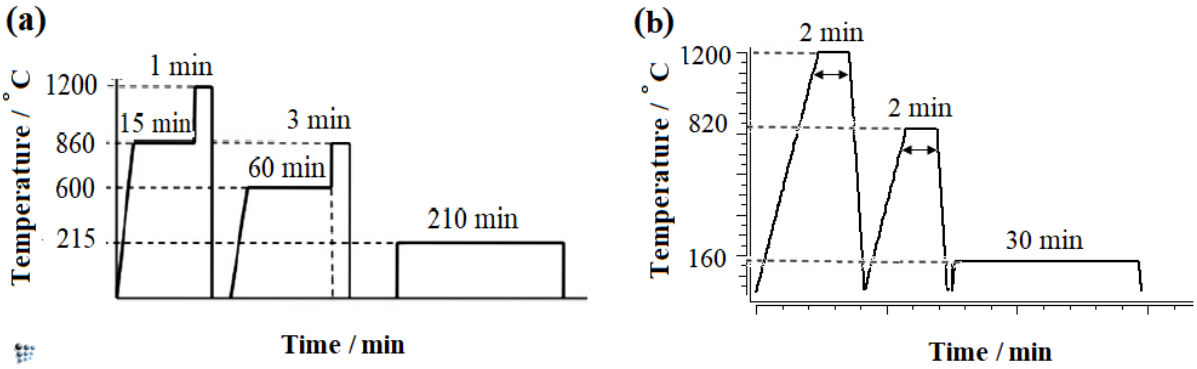

Figure 3.4: Heat treatments of 100Cr6+0.5V alloy: a) original schedule [10, 11], and b) new designed schedule.

Austenitisation at 1200 °C for 2 minutes dissolved all the coarse V_4C_3 and cementite, Figure 3.5 point 1, then a fully martensitic microstructure was produced by quenching to RT. Tempering at 820 °C for 2 minutes re-nucleates a series of nano V_4C_3. During this holding time V_4C_3 precipitates grow to $\sim$ 10 nm in size, with a number density of $\sim$ 1.2 $\times 10^{21}$ m^{-3} and a molar phase fraction of $\sim$ 0.0002. This is followed by a final quench to RT, before tempering for 30 min at 160 °C. The hardness obtained is 765 HV30 ($\sim$ 62.5 Rc).

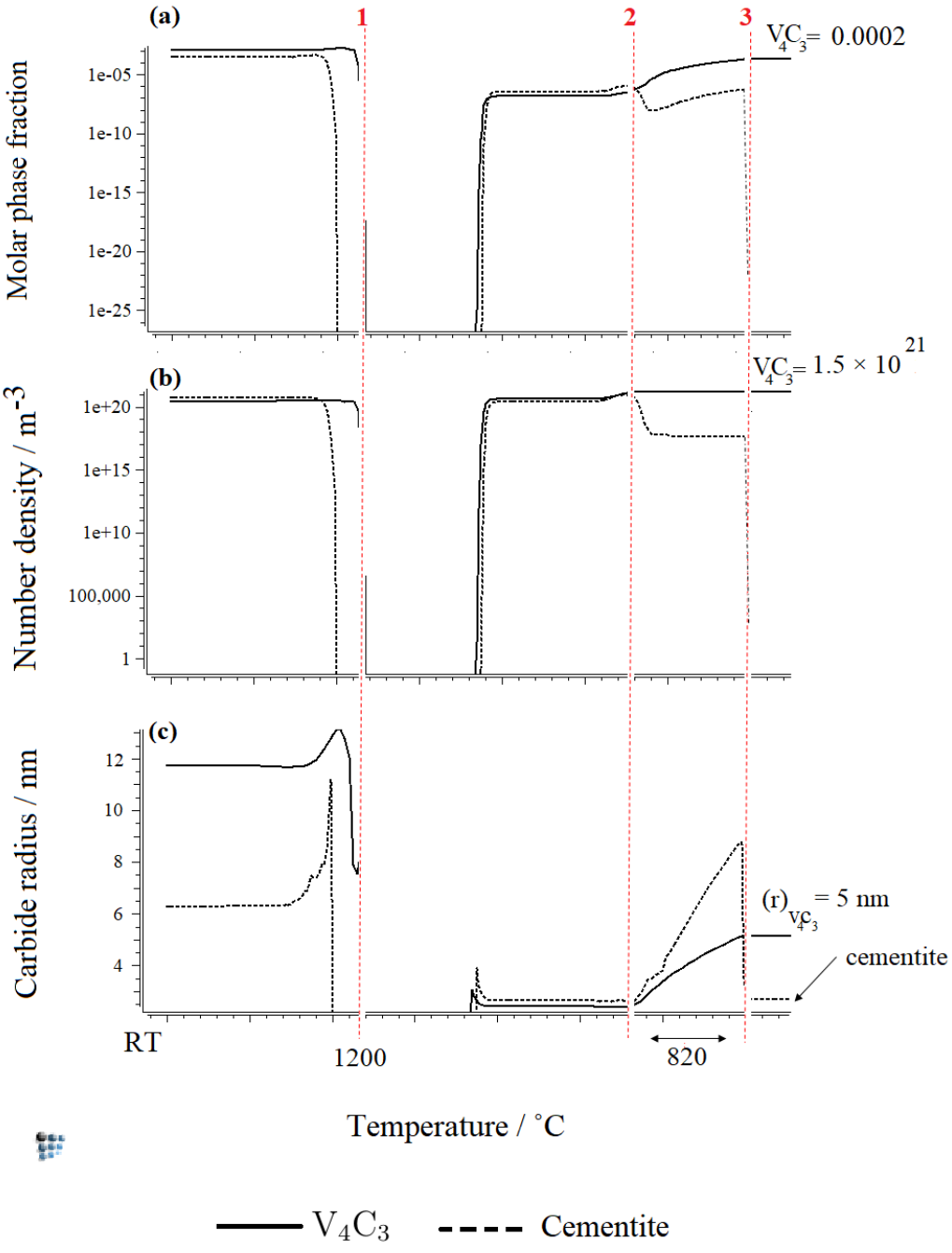

Figure 3.5: Kinetic calculations of carbide evolution during the new heat treatment of 100Cr6+0.5V alloy. Carbides: a) phase fraction, b) number density, and c) radius (r).

3.3 Design and modelling of new Fe-C-Mn-Si-Al TRIP steel

This section was written based on an unpublished work -at the time of writing this thesis. The modelling was done by Sheng-Yen Li at the Department of Materials Science and Engineering, Texas A&M University. The experimental application and analysis were done in the University of Cambridge and will be detailed in the next chapter.

Thermodynamic calculations were used for phase fraction prediction during the intercritical annealing (IA) stage of the designed Fe-0.5C-1.25Mn-1.45Si-0.75Al TRIP steel. The chemical composition of the alloy is presented in Table 3.2.

Table 3.2: Chemical composition (wt.%) of the studied TRIP steel.

Alloy	C	Si	Mn	Al	Cr	Ti	V	W
Fe-C-Mn-Si-Al TRIP	0.52	1.45	1.25	0.75	0.01	0.0010	0.003	0.001

Target temperature for the IA treatment should be between A_{c1} (760 °C) and A_{c3} (820 °C) of the alloy in the ferrite/austenite two-phase region in order to obtain a high volume fraction of ferrite. Different holding times were also examined. Among the selected temperatures, 771 °C was expected to provide the maximum ferrite fraction since it is very close to the eutectoid point [187]. Higher temperatures, however, resulted in a low ferrite content since it is close to A_{c3}. Additionally, it was expected that short IA holding durations should lead to more ferrite than longer times at the same temperature as longer durations bring the microstructure closer to the equilibrium state [188]. Figure 3.6 shows the predicted phase diagram after intercritical annealing stage. After holding at 771 °C

for 900 seconds, about 86 % of the transformation is completed, and 62 % volume fraction of austenite should be obtained. The current procedure also aims at completely avoiding pearlite formation during the IA stage.

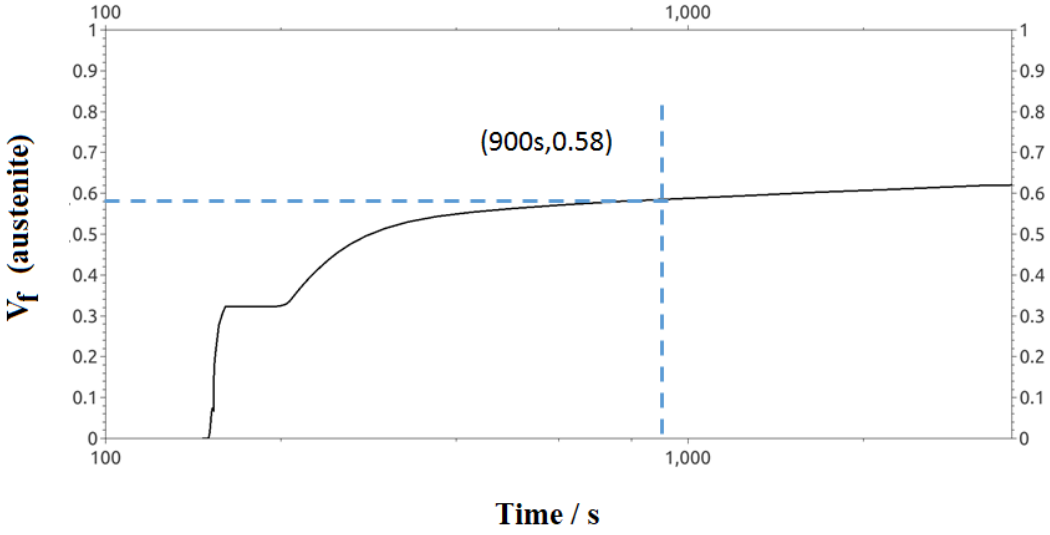

Figure 3.6: Estimated volume fraction of austenite vs. time at inter-critical annealing stage (Courtesy of Sheng-Yen Li, Texas A&M University).

The next stage of the thermodynamic analysis was calculating the austenite stability after IA against martensitic transformation as well as the maximum carbon enrichment of austenite during the bainite isothermal transformation (BIT) treatment. Ferrite that formed during IA was not included in this calculation since it was assumed that it is stable between the end of IA and BIT (assuming sufficient fast quenching). The composition of the austenite after the IA with the designed heat treatment parameters was taken as the initial state for the BIT. However, because it was difficult to predict the composition during non-equilibrium conditions, the chemical composition of austenite was calculated assuming that the equilibrium condition is reached [187], Table 3.3.

It is also important while designing the alloy to maximize the retained austenite content, thus, martensite formation needs to be suppressed before and after the BIT.

Table 3.3: Expected microstructure and ultimate tensile strength.

Austenite vol.%	**Bainite vol.%**	**Ferrite vol.%**	**Martensite vol.%**
0.36	0.32	0.32	0.00
Carbon wt.% in retained austenite		**UTS (MPa)**	
1.36		1303	

With this aim, M_s temperature of the alloy after the IA must be lower than the BIT temperature, and lower than room temperature [187] after the BIT. Also, the carbon concentration of austenite after the BIT should be at least 1.36% as shown in Table 3.3 to fully suppress the martensite formation. Based on these assumptions, calculations predicted that the corresponding BIT temperature should not be higher than 302 °C.

The steel is expected to achieve an ultimate tensile strength (UTS) around 1303 MPa, with a final microstructure consists of 0.36, 0.32 and 0.32 volume fraction of retained austenite, bainite and ferrite, respectively. Retained austenite is expected to contain 1.36 wt.% of carbon, Table 3.3.

3.4 Summary

Thermodynamic and kinetic modelling was employed to design a new 100Cr6+0.3V with a lower vanadium content. The model showed a reduction on V_4C_3 dissolution temperature with the reduction in vanadium content in the cast. Thus, a new bearing steel with 0.3 wt.% was designed. In addition, a new heat treatment was proposed for the novel industrial cast 100Cr6+0.5V in order to develop the vanadium containing hydrogen embrittlement resistant steels. Thermo-Calc and kinetics calculations were carried out in

the Department of Materials Science and Engineering, Texas A&M University in order to design a new Fe-0.5C-1.25Mn-1.45Si-0.75Al TRIP steel with an expected UTS around 1303 MPa.

Chapter 4

Experimental methods

This chapter describes the experimental procedures including microstructural observations, mechanical properties measurements and hydrogen embrittlement testing for 100Cr6 bearing and TRIP steels.

4.1 100Cr6 bearing steels

In the framework of this research, three grades of high strength bearing steels were studied, Table 3.1. 100Cr6 is a vanadium-free steel, it was employed as a reference in this study and was supplied by Ovako. 100Cr6+0.5V supplied by Tata steel and provided by Professor Mark Rainforth, University of Sheffield. Their compositions were provided by the suppliers. The new alloy 100Cr6+0.3V is a lab cast and was prepared in Edmund Buhler Arc Melter in the Process laboratory of the University of Cambridge, where it was melted in vacuum and finally produced in finger-shaped rods. The elements compositions were weighed only before casting with no further measuring of the chemical composition for the final product. After casting, the structure was then homogenised by holding it at

1200 °C for 48 hours and slow cooling to room temperature (RT), and finally swaged to 4 and 8 mm diameter rods.

4.1.1 Heat treatment and morphology characterisation

Before applying any heat treatment (HT), all steels were spheroidized in accordance to the scheme shown in Figure 4.1 [189] to boost their machinability [14]. Following the spheroidization treatment, the specimens were cut to a cylindrical dilatometery shape, typically 8.0 mm diameter and 12.0 mm length, then heat treated in vacuum in Thermecmastor-Z dilatometer (Version 3.471). This equipment allows design and control simulations of thermo-mechanical treatments. To make it comparable, the four heat treatment schedules for the steels are put together in Figure 4.2.

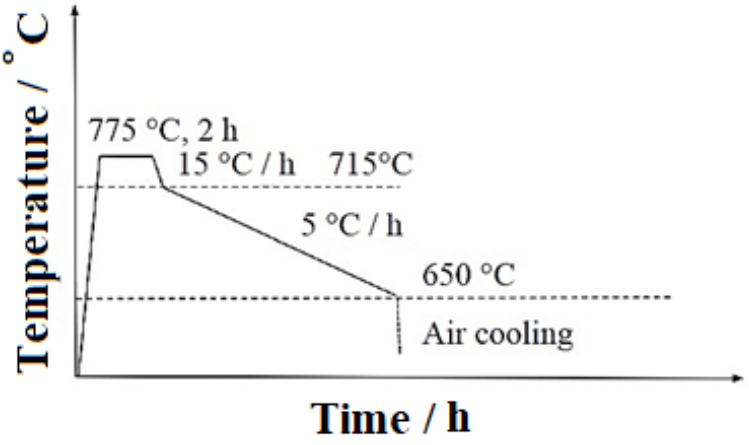

Figure 4.1: Soft annealing (spheroidization) applied before machining and hardening of 100Cr6, 100Cr6+0.5V and 100Cr6+0.3V steels [189].

To characterise the steels after applying full heat treatments, metallographic observations were carried out as following.

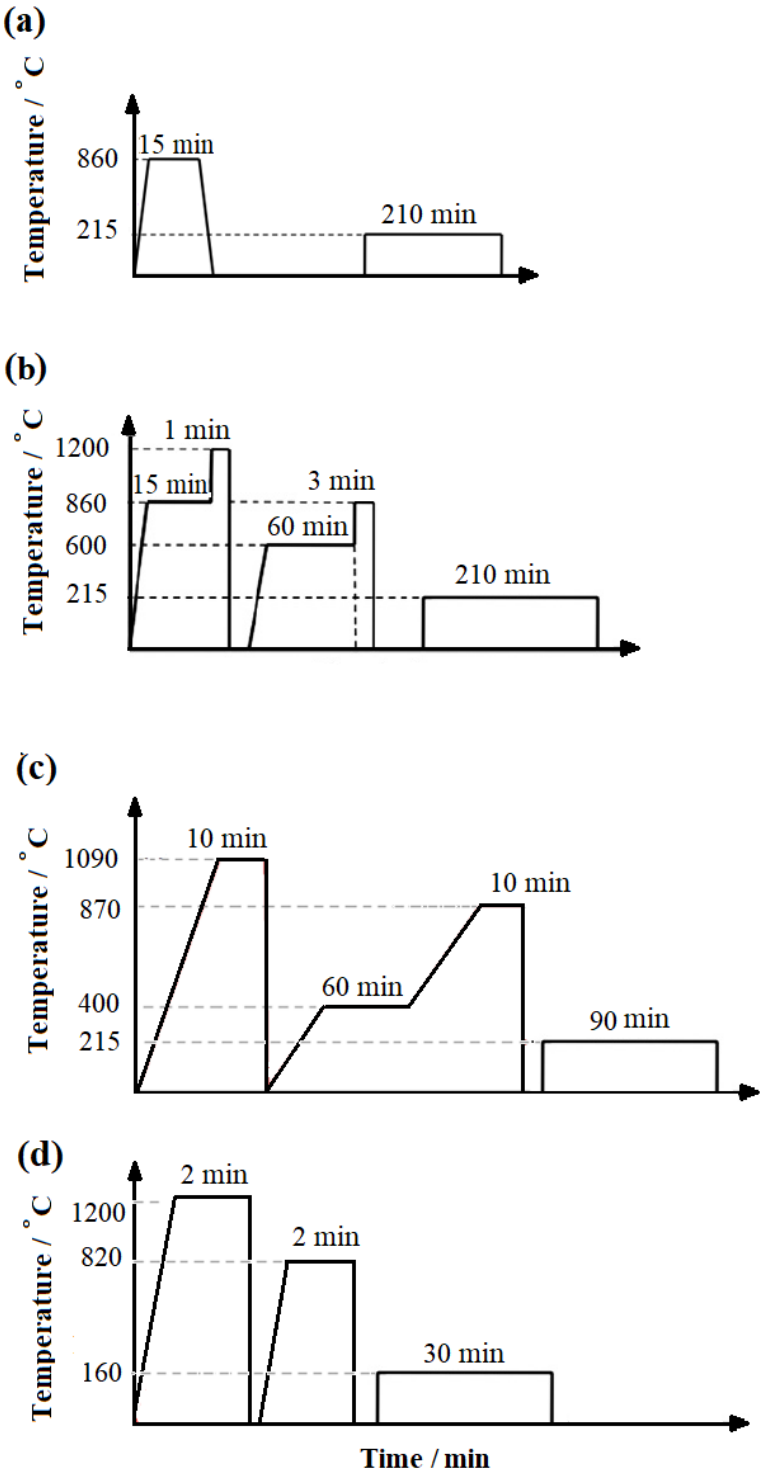

Figure 4.2: Heat treatment schedules of: a) 100Cr6, b) 100Cr6+0.5V (original HT designed by [10, 11]), c) 100Cr6+0.3V, and d) 100Cr6+0.5V (new HT).

Scanning electron microscopy

FEI Nova Nano scanning electron microscope (SEM) with a 20 kV electron beam voltage in secondary electron mode was used. Chemical analysis was done by using energy dispersive X-ray spectroscopy (EDX). SEM specimens were polished using 1200 and 2500 grit SiC paper, then with 6 μm and 1 μm diamond paste for a scratch-free surface. In order to reveal the microstructure, the specimens were etched in 2 % nital etchant (2 % nitric acid and 98 % methanol), rinsed with acetone, and finally dried in hot air.

X-ray diffraction

Bruker D8 DAVINCI with position sensitive detector (LynxEye EX) was used for X-ray diffraction (XRD) measurements. X-ray data were obtained between 35° and 110° with a step size of 0.05° and a dwell time of 1 second. The phase fractions in the final structure were determined using Rietveld method. To prepare the specimens for the scan, they were polished using 1200 and 2500 grit SiC paper, then with 6 μm and 1 μm diamond paste for a scratch-free surface, rinsed with acetone, and finally dried in hot air.

Transmission electron microscopy

FEI Tecnai F20 and FEI Tecnai Osiris transmission electron microscopes (TEM) were employed to verify that the desired microstructure had been obtained. The nature of carbides were confirmed by TEM/EDX measurements in STEM mode with 2.7 nA probe current. TEM specimens were mechanically polished with coarse grit SiC papers in order to reduce their thickness to 100 μm. After, they were punched into 3 mm diameter discs then manually ground on 1200 grit paper to around 50 μm. Finally, a twin-jet electropol-

isher was used with an electrolyte prepared of 5 % perchloric acid, 25 % glycerol and 70 % ethanol. The electrolyte was cooled to around 10 °C. In order to obtain specimens that are electron transparent, it is important before starting the process to scan the voltage used for each material. For 100Cr6, 100Cr6+0.5V and 100Cr6+0.3V steels, 22.5 Volt was a sufficient value.

Atom probe tomography

Vanadium carbides were analysed for 100Cr6+0.5V steel using atom probe tomography, with a stoichiometry of M_4C_3. 100Cr6 was used as a baseline. The specimens were heat treated in the Department of Materials Science and Metallurgy at the University of Cambridge, and afterwards sent to the Department of Materials at the University of Oxford for the analyses by CAMECA^{TM} LEAP 5000XR instrument with a pulse frequency of 200 kHz, specimen temperature set to 50 K, and a laser pulse energy of 44 pJ [190]. The 100 nm needles "matchsticks" specimens for atom probe tomography were prepared using a standard two-stage electropolishing procedure [191].

4.1.2 Hydrogen charging experiments

Hydrogen was introduced to the specimens cathodically in an aqueous solution. To this aim, the cylindrical specimens were firstly polished using 1200 grit SiC paper, cleaned ultrasonically in acetone, then dried. The recommended technique here is to charge each specimen individually at RT for 5 days to reach a saturation state. The saturation steady state was examined by hydrogen charging three specimens individually for 1, 2 and 3 days, then place each specimen in the thermal desorption analysis (TDA) equipment. The measurements were performed with Agilent Technologies 7890B GC system, which is

shown in Figure 4.3. The inlet is where the carrier gas carries the hydrogen injected into the GC [192], GC column is the gas chromatography unit, MFC is the mass flow control (for desorption flow), and HSTD is the tank with a standard gas mixture to calibrate the hydrogen content [92]. During the process, status messages from the GC are displayed, and parameter settings are controlled through the operating panel or data system [192].

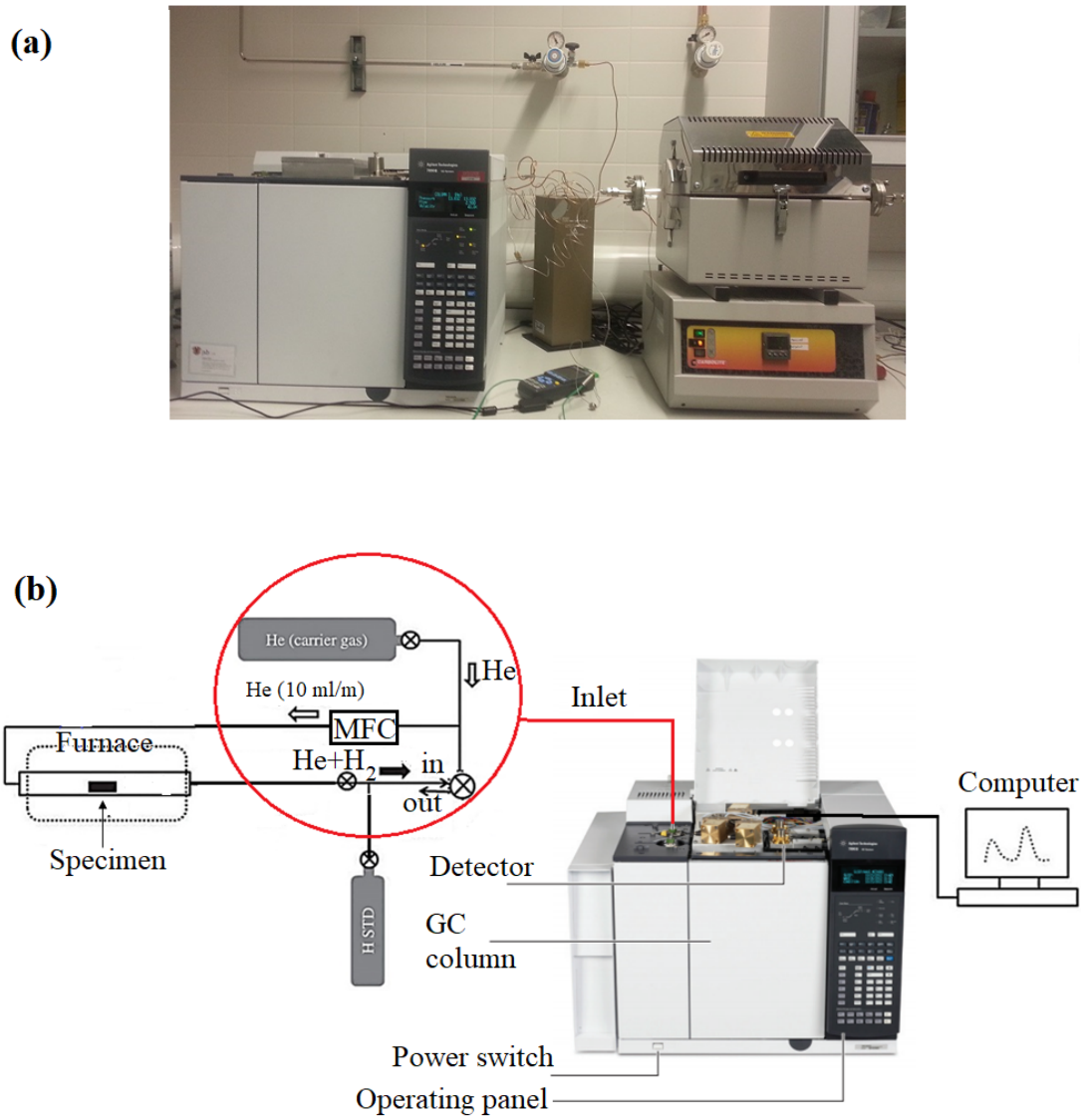

Figure 4.3: a) Thermal Desorption Analysis equipment, Agilent Technologies 7890B GC. b) Schematic diagram showing of TDA [192].

The data corresponding to hydrogen desorption rate versus desorption time are collected, as shown in Figure 4.4. Clearly, the specimens reached the saturation state after

3 days of charging as the two TDA curves of 2 and 3 days of charging ended meeting at almost a negligible value of hydrogen desorption rate. Five days were therefore selected as a standard for hydrogen charging to suit specimens with different sizes in this study.

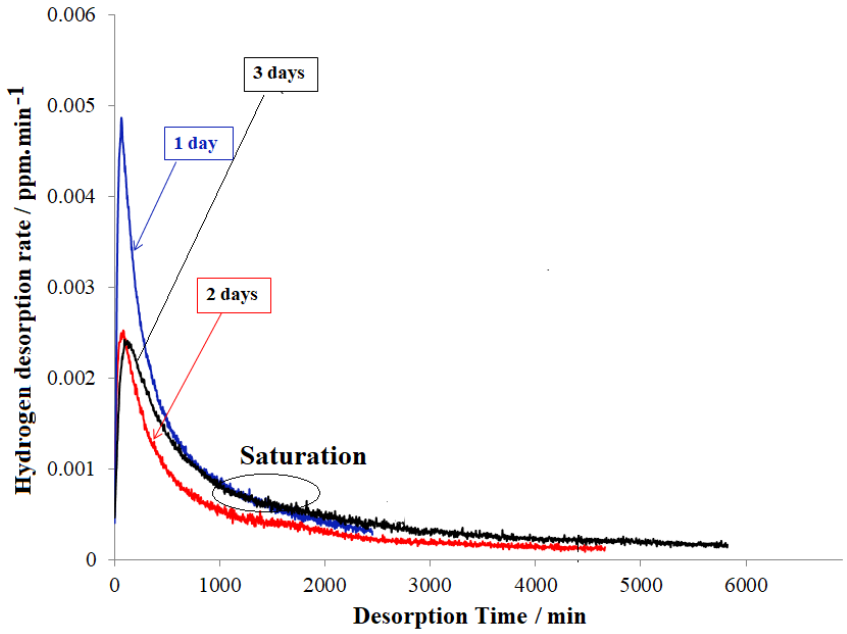

Figure 4.4: Hydrogen desorption rate in ppm min^{-1} (parts per million per minute) as a function of time (in min).

In this work, the time to saturation was shortened by increasing the cathodic current density to 10 mA cm^{-2}. During charging, hydrogen is introduced to the specimen from a water-based electrolyte of 3.0 % NaCl + 0.3 % NH_4SCN (ammonium thiocyanate) by connecting the specimen to the cathode and the platinum wire to the anode. At the end of charging duration, the specimen is washed and ground with 2500 grit SiC paper to remove any oxidation layer, washed with acetone, and dried. Given that this work focuses on the amount of hydrogen trapped within the material, specimens were left at RT for an average of 4 days to allow diffusible hydrogen (hydrogen trapped in shallow/weak traps) to leave the specimens. Due to its high mobility, diffusible hydrogen will immediately start to leave the charged specimens.

The net weight of each specimen was measured after being hydrogen charged and cleaned. This value was subsequently used as a reference for calculating the amount of trapped hydrogen. Hydrogen within the specimens was measured by means of TDA. Hydrogen charged specimens were placed into the TDA system within 2 minutes after charging. The TDA system consisted of an inert 99.9999 % helium gas that acts as a carrier gas, with a controlled flow 10 ml min^{-1}, a temperature controlled furnace, and a gas chromatograph for hydrogen detection [149]. The procedure starts with 20 minutes of helium purging, followed by 10 minutes to enable the gas flow to stabilise in the system. Specimens were then heated from RT up to 400 °C with various heating rates depending on the purpose of each test which will be explained in subsequent sections. Hydrogen content was measured in three minutes intervals. In order to define the total hydrogen content from the specimen, the calculations for all the hydrogen peaks need to be performed and summarised [92]. Areas under the hydrogen peaks were integrated and their average area calculated, this area is subsequently used as a reference for calculating the hydrogen desorption rate and hydrogen amount released from the charged specimen. By dividing the average area by the specimen's net weight, then multiplying the final result by three minutes the amount of hydrogen content in parts per million (ppm) for the considered peak is achieved.

Activation energy measurements

The activation energies (E_a) for hydrogen egress in 100Cr6 and 100Cr6+0.5V steels were determined experimentally using TDA. Three specimens of each grade were heat treated according to Figure 4.2 a and b, without the final martensite tempering stage. Tempering martensite was skipped to avoid the formation of low temperature iron carbides that could trap some hydrogen content, therefore, most of the measured hydrogen will be de-trapped

from V_4C_3 or dislocations. The specimens were hydrogen charged following the protocol described in section 4.1.2. For each grade, three specimens were heated in TDA to 285 °C at three heating rates: 25, 50, and 75 °C h^{-1}.

4.1.3 Mechanical properties testing

Hardness measurements

The hardness obtained after each heat treatment was measured by Vickers Instruments 255873 with a 30 kg load. Before placing the specimen into the hardness testing machine, it should be polished to flatten its surface and to remove any deep marks or debris that could give inconsistent results. For each case, Vickers hardness was obtained by calculating the surface area (d) of the indentation: $d = (d_1+d_2)/2$, where d_1 and d_2 are the indentation two diagonals. The corresponding Vickers hardness is then calculated by applying the formula $1.8544F/d^2$, where F is the used load [193]. For each specimen, an average of 10 readings were calculated for high reliability measurements.

Hydro-Hardness test

A new technique adapted from an earlier work [92] was used to examine the nature of crack propagation and hydrogen embrittlement mechanisms in 100Cr6, 100Cr6+0.3V and 100Cr6+0.5V steels. Vickers indentation was used to induce cracks propagating from the indentation in specimens before and immediately after hydrogen charging. Hydro-hardness method allows visualisation the hydrogen degassing from a specimen on the macro-scale which could be used for further analysis. When introducing surface cracks on hydrogen-charged specimens, hydrogen bubbles appear gathering around the crack tips

which shows that hydrogen tends to diffuse towards the high-stressed areas, such as the crack tip. Also, for a given crack length, hydrogen content and recorded bubbles around the crack tip, the hydrogen-induced cracking phenomena can be determined.

With this intention, specimens from 100Cr6, 100Cr6+0.3V and 100Cr6+0.5V were tested in three different conditions: (1) hydrogen-free, (2) hydrogen-charged for 24, 48 and 72 hours, and (3) one week at RT after being hydrogen charged.

Before charging, the specimen surface was polished to a scratch-free level, and after charging the surface was re-polished with 6 μm and 3 μm diamond paste. An indentation was made with 120 kg load. This load was chosen after testing 30, 60, 90 and 110 kg loads where all were not sufficient to introduce cracks into hydrogen rich specimens. Cracks were observed by using Leica DFC 295 optical microscope. To reveal and foster the formation of hydrogen bubbles around cracks, one drop of immersol (TM) 518F oil for optical microscope Zeiss was put on the top of the specimen. The crack length and bubbling rate were measured for each case [92].

Tensile tests

To evaluate the hydrogen embrittlement susceptibility of high strength bearing steels, slow strain rate tests on notched round bar specimens, Figures 4.5 and 4.6, were carried out at a constant tensile cross head speed of 0.005 mm s^{-1} at RT. 100Cr6 and 100Cr6+0.5V specimens were machined according to ASTM E8/E8M [194] for test specimens with gauge length four times the notch's diameter. The length of the reduced parallel section was altered to follow the standard size of Bähr dilatometer where the specimens were heat treated in CENIM laboratories. The specimens special geometries were carefully studied and chosen to meet the dilatometer and ASTM standards, concurrently. The

original heat treatment of 100Cr6+0.5V in Figure 4.2b was adjusted by reducing the carbide dissolution temperature from 1200 °C to 1100 °C with holding time of 10 minutes instead of 1 minute. This was suggested and thermodynamically approved to bring the temperatures closer to Bähr dilatometer maximum capability with a comparable amount of precipitated V_4C_3. After heat treatments, the hardened tensile specimens were polished in Finishing Techniques Limited to remove oxidation layer and scratches for a uniformly smooth surface.

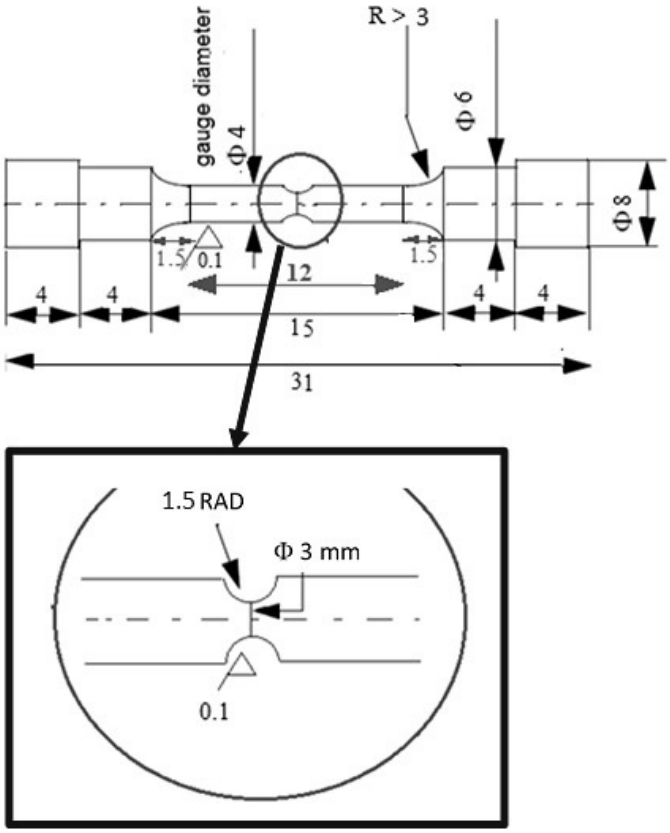

Figure 4.5: Schematic sketch of the tensile test specimens. Dimensions according to ASTM E8/E8M [194].

Each grade was classified into two groups, hydrogen-free and hydrogen-charged, for comparison purposes. In the case of hydrogen-charged specimens, the notch and both fillets were painted by lacomit varnish to avoid embrittlement resulting from corrosion/oxidation during charging. Specimens were charged for 24 hours with a current

Figure 4.6: Shoulder-end round cross-section tensile specimens made from 100Cr6 alloy (Courtesy of David San Martín, CENIM).

density of - 1.0 mA cm^{-2} to reduce the formation of oxidation layer on the specimen surface. Tensile specimens were removed from the hydrogen charging cell, dried, and tested within 5 minutes. Similarly, a separate specimen was hydrogen charged to measure the total hydrogen content and correlated mechanical results. About 3.6 ppm of hydrogen was charged into a specimen that weights 60 grams. Weakly trapped hydrogen released during transporting the specimens from the charging cell into the tensile test system was neglected when the total hydrogen in the sample was measured.

Uniaxial tensile test was performed at ambient temperature on hydrogen-free and hydrogen-charged notched tensile specimens using Instron 8800 low cycle fatigue (LCF) machine with Bluehill 3 static testing software, and a 2 mm × 135 mm 99.7 % alumina extensometer was used in all tensile tests. The strain rate was calculated from the ratio between the cross head speed and specimen's gauge length. The test was repeated three times for each case. After failure, an intensive investigation was carried out using SEM/EDX on the fracture surface of tested specimens. For this purpose, fracture surfaces were cleaned using acetone without any further treatment.

Rolling contact fatigue tests

RCF tests were performed on two grades, 100Cr6 and 100Cr6+0.5V. 100Cr6 rods were provided by Jakub Rydel. Typical RCF specimen geometry -as provided by SKF company- is shown in Figure 4.7. Heat treatments were carried out at Summitglow Ltd. in Sheffield in a salt bath. 100Cr6 rods were heat treated according to Figure 4.2a.

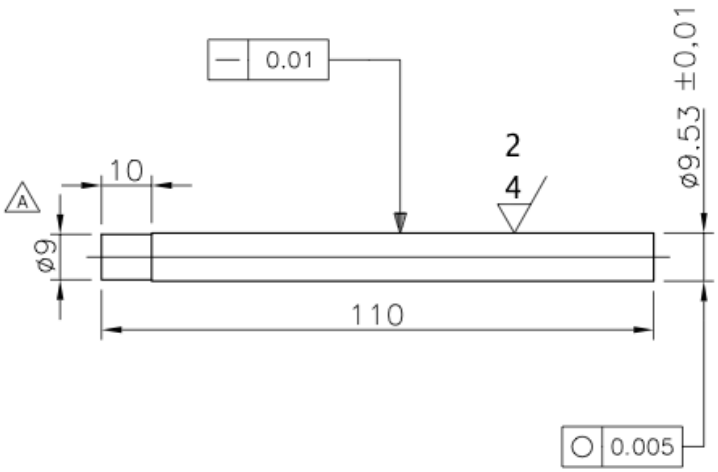

Figure 4.7: Geometries of rolling contact fatigue specimen used for RCF testing.

100Cr6+0.5V heat treatment was, however, slightly altered to bring the treatment closer to industrial reality, Figure 4.8 [92]. Later, the rods were machined to specification and to remove possible oxides remaining after processing. RCF experiments were conducted in two conditions, hydrogen-free and hydrogen-charged for 24 hours. Before hydrogen charging, the middle section of the rods was painted by lacomit varnish to avoid a decrease in surface roughness due to oxidation, Figure 4.9, thereby hydrogen is allowed to ingress into the rods from parts that are out of the testing range. The rods were held rigidly by their flat base to help maintain a proper vertical alignment. After that they were charged individually with a current density of - 1.0 mA cm^{-2} for 24 hours similar to the tensile test specimens. At the end of the charging process, it is advisable to clean the specimen by removing the paint with acetone without grinding to maintain the final

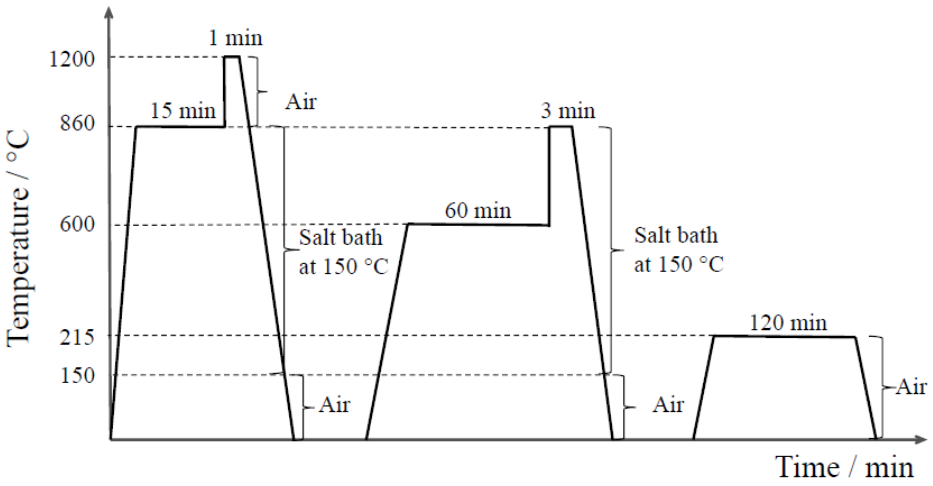

Figure 4.8: Altered heat treatment of 100Cr6+0.5V performed in the salt bath furnaces [92].

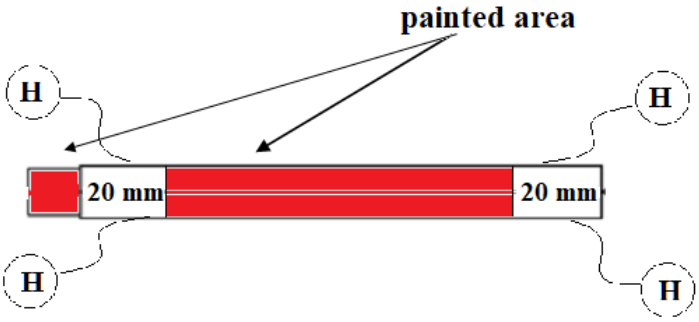

Figure 4.9: Painted parts of RCF rods during hydrogen charging process.

surface roughness. The total hydrogen in RCF rod was around 5.6 ppm

Tests were performed on a rolling contact fatigue tester by Delta Research Corporation Model BR-4. This consists of four test stations allowing different loads and speeds to be run simultaneously. A description of RCF equipment was detailed by Glover [195]. The maximum contact stress used was 4.2 GPa, the speed of rotation 3600 rpm and BP2380 turbine oil was used as a lubricant at 10 drops per minute. The total time from the end of hydrogen charging to the beginning of the test was around 20 minutes

4.2 TRIP steel

0.5C-1.25Mn-1.45Si-0.75Al TRIP alloy was supplied by the University of Sheffield, Department of Engineering Materials by Prof. Mark Rainforth, and was cast at Tata Steel who provided the chemical composition in Table 3.2.

Before investigations started, the cast was subjected to an equal channel angular extrusion (ECAE) at Texas A&M University Laboratories. ECAE involves inserting the specimen in a die that has two channels with equal cross section intersecting at an angle ranges from 60° to 150°. During the extrusion, the specimen undergoes no change in cross section, and therefore it can be reinserted into the die resulting in a very large plastic strains and a considerable grain refinement of a polycrystalline metal. The microstructure also changes substantially and the ultimate tensile strength significantly enhanced [196], Figure 4.10. ECAE process here is a non-isothermal extrusion carried out in a decaying temperature from 950 °C. Inserting the billet into the die from the furnace took about 2 to 3 seconds, followed by another 6 seconds for the whole extrusion. The billets were still red hot after being removed from the die, and left for air cooling. The final product has dimensions of 25.4 mm × 25.4 mm × 177.8 mm.

Studies [197] showed that the bainite plates size and dislocation density are principal parameters that influence the hardness of bainitic structure, and since the high strength of these steels is due to their very fine structure, bainite obtained after a longer holding time has greater plates size and lower dislocation density, thus lower hardness.

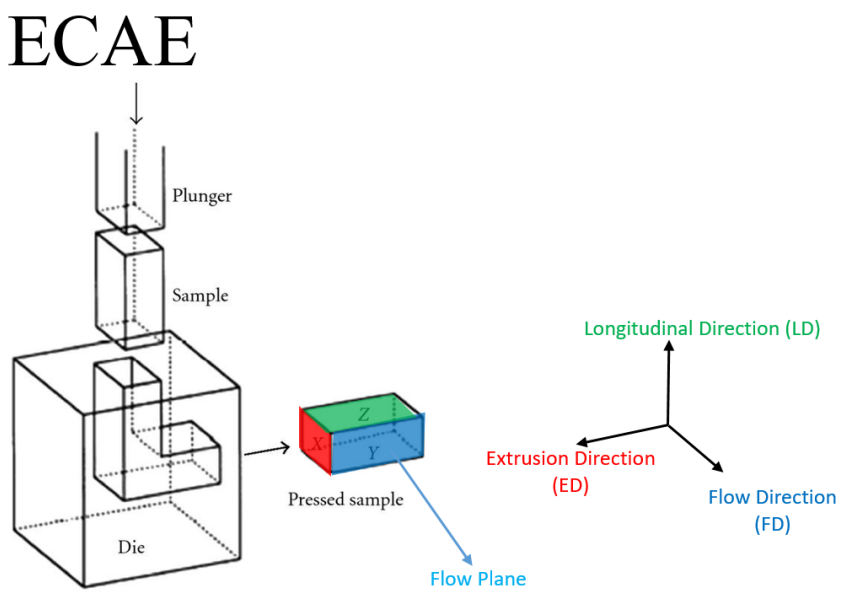

Figure 4.10: Schematic of the equal channel angular extrusion process. Cast dimensions at the end of the process are 25.4 mm × 25.4 mm × 177.8 mm (Courtesy of Taymaz Jozaghi, Texas A&M University).

4.2.1 Heat treatment and morphology characterisation

This section covers the experimental analysis of two-stages heat treatment of the studied TRIP steel.

Optimising intercritical annealing stage and the influence of the heating rate on $\alpha + \mathbf{p} \rightarrow \alpha + \gamma$ transformation

The influence of heating rate (HR) on pearlite + ferrite → austenite transformation was studied by two methods. First, by austenitising two specimens to 1000 °C, one with HR = 3 °C s^{-1} and the other with HR = 10 °C s^{-1}, then analysing the dilation curves. This was done by means of dilatometer DIL805 (v10.2), with standard cylindrical specimen of 4 mm in diameter and 10 mm in length. The second method is a microstructural

measurements after running a full heat treatment (intercritical annealing IA + bainitic isothermal transformation BIT) applying the previous heating rates, 3 and 10 °C s^{-1}. Two specimens were subjected to identical annealing by heating to 771 °C, holding at 771 °C for 15 minutes, followed by a rapid cooling that was interrupted at 302 °C, holding at 302 °C for 30 minutes for bainitic transformation, and finally quenched to room temperature. The variation was in the heating rate from room temperature to 771 °C, HR = 3 °C s^{-1} for specimen 1, and HR = 10 °C s^{-1} for specimen 2. Later, microstructures were studied using SEM. Based on the SEM image analysis for both specimens, one of the previous heating rates was chosen to be applied in the next step.

To confirm the transformation of pearlite + ferrite into austenite shown in Figure 3.6, an additional specimen was heated to 771 °C with a HR = 3 °C s^{-1}, held at this temperature for 15 minutes, then quenched to RT at 20 °C s^{-1} (IA + quenching). To reveal the microstructure, the specimen surface was polished for a scratch-free level, then etched in 2 % nital etchant, rinsed with acetone, then dried with hot air. Metallographic observations were carried out using Leica DFC295 optical microscope and FEI Nova NanoSEM in the secondary electron mode. Quantitative analyses of phases in the microstructure after applying IA stage was done using MagniSci application for microscopic analysis [198] on an average of 10 optical microscopy images with magnification 50x. This method allows evaluating of the phase fractions of various phases in the microstructure.

Bainite isothermal transformation stage

After optimising IA stage of the heat treatment and the optimum heating rate, the following scenarios were prepared for BIT testing. Six specimens were annealed individually in vacuum in the dilatometer. Each specimen was subjected to the optimum IA stage

and heating rate, referred to Section 4.2.1. The variation was in the second stage of the annealing, BIT, that involves bainitic formation. Here, the specimens were isothermally held at 302 °C for 3, 6, 24, 30, 60 and 180 minutes, and finally quenched to room temperature. Figure 4.11 shows a schematic diagram of a complete heat treatment of the steel studied. Specimens were then prepared for metallographic observations. The hardening caused by transformation of austenite to bainite was measured through hardness testing by Vickers pyramid hardness testing machine with a 30 kg load. The hardness number for each scenario is presented in Figure 4.11.

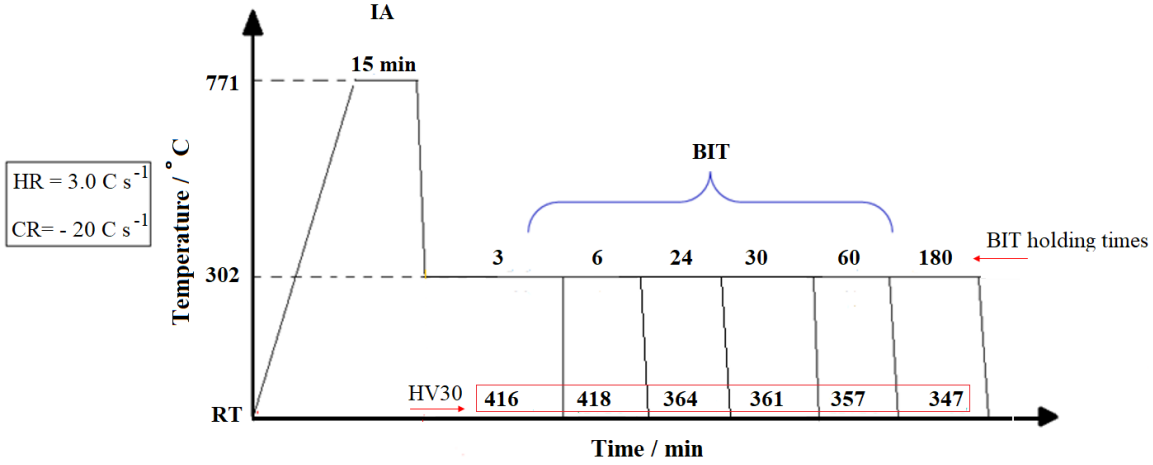

Figure 4.11: Summary of optimising the full heat treatment of TRIP steel (HR indicates heating rate, and CR indicates cooling rate or quenching).

X-ray diffraction was applied for microstructure identification. This was obtained between $2\theta = 40°$ to 120°, step size of 0.02°, a dwell time of 1.0 s, and a Cu target was used (CuKα). Retained austenite fraction in the final structure was determined experientially using X-ray phase analysis adopting the Rietveld method. Finally, Tecnai F20 FEG TEM was employed to verify that the desired microstructure was obtained. Scanning and transmission electron microscopies aided the detection of microstructural evolution during heat treatments.

As a result of the previous extensive analysis, three specimens were selected for hydrogen charging. The specimens were bainitically transformed for 24, 30 and 60 minutes. The activation energy of de-trapping was calculated for one specimen which had had 30 minutes holding time at BIT. Both measurements followed procedures described in section 4.1.2.

4.2.2 Hydrogen embrittlement tests

Characterization of hydrogen induced cracking using hydro-hardness technique

To clarify the effect of hydrogen on the mechanical properties and hydrogen-induced cracking under stress of the studied TRIP steel, hydro-hardness technique was performed following the procedure descried in section 4.1.3. For the TRIP steel, two cases were chosen, BIT for 24 and 60 minutes. These were selected as a lower and higher fractions of retained austenite among the three final cases, 24, 30 and 60 minutes. Each specimen was tested immediately after hydrogen charging and the crack length was measured in both cases.

Hydrogen trapping and de-trapping activation energy

In this work, multiple thermal desorption analysis experiments were performed on the TRIP alloy to reveal the type of hydrogen traps by calculating the corresponding de-trapping activation energy since microstructural defects that act as hydrogen traps correlate to the peak temperatures that appear during TDA. This procedure helps the determination of the location of hydrogen in various microstructural features. Heating is

required to provide the thermal energy necessary to allow hydrogen to overcome the trap activation energy barrier and diffuse out of the steel [149].

Likewise bearing steels in section 4.1.2, a specimen from the final BIT scenarios (holding at 302 °C for 24, 30 and 60 minutes) was charged for five days then left at room temperature for three days to remove diffusible hydrogen. These specimens were used to measure the amount of trapped hydrogen for each case. To make all TDA results comparable, specimens of 12.0 mm length and 8.0 mm diameter were prepared for this test. Each hydrogen charged specimen was placed individually in the TDA, heated up to 400 °C with a constant heating rate, HR = 50 °C h^{-1}, then left to cool to room temperature. The experiment was repeated three times for each case for validation. A second group of specimens with similar dimensions were prepared for measuring the de-trapping activation energy. Accordingly, three specimens of BIT for 30 minute case were hydrogen charged as mentioned before, then individually heated in the TDA in three different heating rates 25, 50 then 75 °C h^{-1}.

4.3 Summary

New heat treatments designed for 100Cr6+0.3V and 100Cr6+0.5V steels were successfully applied and examined. Characterisation techniques were adopted to reveal that the desired microstructures were achieved. The mechanical properties tests were employed to emphasize the role of vanadium in enhancing the hydrogen embrittlement resistance of bearing steels. The heat treatment of TRIP steel was optimised and the hardness was measured. For all steels, the hydrogen trapping capacity as well as the de-trapping activation energies were calculated.

Chapter 5

Results and discussion

5.1 100Cr6 bearing steels results and discussion

5.1.1 100Cr6, 100Cr6+0.5V and 100Cr6+0.3V morphology characterisation

The next step after producing a series of V_4C_3 precipitations is to charactrise the microstructure at the atomic scale. Therefore, a combination of SEM, XRD, TEM and APT was used. For streamlining, the techniques used for each grade are summarised in Table 5.1.

Specimens were heat treated and tempered according to Figure 4.2. Initial examination was done by SEM. Micrographs of all the steels indicated a tempered structure. The beneficial effect of tempering stems from the vulnerability of fresh martensite to hydrogen embrittlement (HE) [201]. Tempering improves the toughness by decreasing the steel hardness [202, 203] hence reducing the susceptibility to HE. However, Figure 5.1a shows

Table 5.1: Characterisation technique used per grade.

Grade	Characterisation technique
100Cr6	SEM - XRD - TEM - APT
100Cr6+0.5V (original HT)	SEM - XRD - TEM - APT
100Cr6+0.3V	SEM - XRD - TEM
100Cr6+0.5V (new HT)	TEM

tempered martensite with coarse spheroidized carbides (average diameter 495 nm).

It is noteworthy that 100Cr6 specimens in Figure 5.1a were the only ones that showed precipitation of coarse cementite particles in martensite, while both vanadium steels in Figure 5.1b and c did not. Earlier studies [199, 200] revealed that vanadium promotes secondary carbide precipitation during the solid-state phase transformation. In such a manner, vanadium homogeneously dissolved across the matrix forming extensive V_4C_3 precipitations, which replace cementite carbides at high tempering temperature [204].

The phase fractions in the final structure were determined by X-ray using Rietveld method, Figure 5.2 and Table 5.2. There were low errors in the calculated parameters which were referred to the instrumental broadening. More than 83 % of the microstructure is martensite, and between 13 to 15.5 % of austenite is retained in martensite, with less than 4 % of carbides. V_4C_3 peaks were not observed in the X-ray diffractogram (XRD). Because of their nanosize, they produce broader and less intense peaks that are much lower than the resolution level of XRD equipment [205]. Hence the need emerged for higher resolution techniques to identify the nature of the nanoparticles that are present in the microstructure.

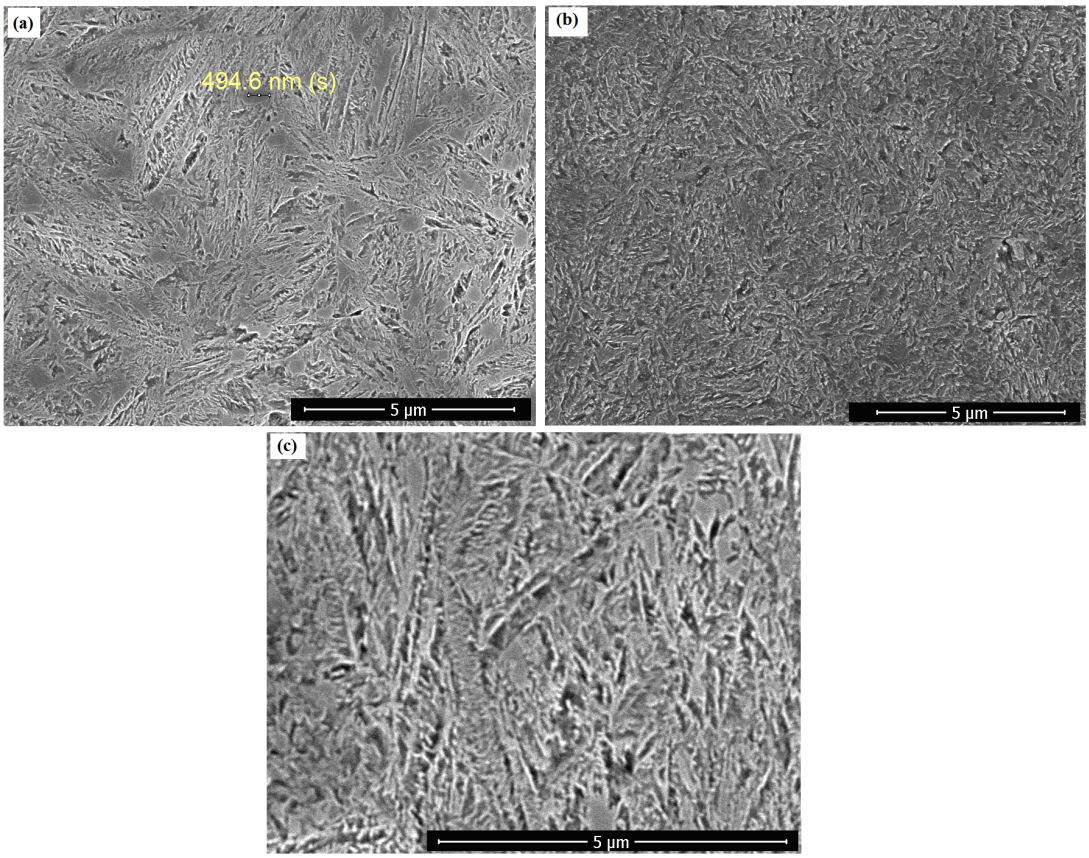

Figure 5.1: Microstructure of martensitic: a) 100Cr6, b) 100Cr6+0.5V, and c) 100Cr6+0.3V steels by SEM. 100Cr6+0.5V steel was heated according to the original heat treatment (HT) [92].

The formation of nanosize V_4C_3 was confirmed by transmission electron microphotographs. Bright field images in Figure 5.3 confirmed the formation of 5 - 10 nm (radius) V_4C_3 precipitates dispersed in the martensitic matrix of 100Cr6+0.5V with original heat treatment (HT) (Figure 5.3b), 100Cr6+0.3V (Figure 5.3c), and 100Cr6+0.5V with new HT (Figure 5.3d). However, it was observed that some V_4C_3 sizes varied between 5 nm in radius which is close to the calculated size in sections 3.2.1 and 3.2.2, respectively, while several other carbides reached 10 nm in radius suggesting that coarsening is in fact much faster than predicted by modelling, hindering precipitation control [206].

TEM/EDX results in Figure 5.4 demonstrate that the investigated carbides are high

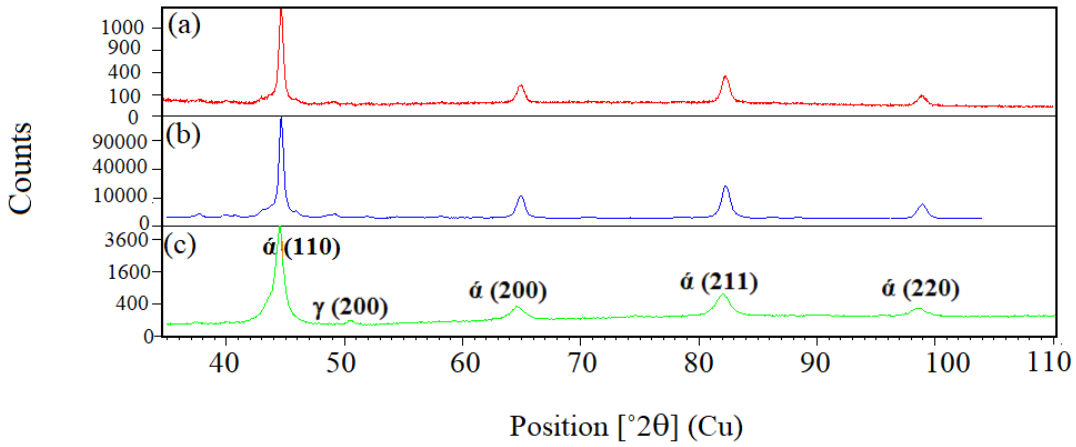

Figure 5.2: X-ray diffraction patterns of: a) 100Cr6, b) 100Cr6+0.5V, and c) 100Cr6+0.3V steels. 100Cr6+0.5V steel was heated according to original heat treatment [92].

Table 5.2: Phase fractions determined from the X-ray data for bearing alloys.

Grade	Austenite	Martensite	Carbides
100Cr6	13	83.2	3.8
100Cr6+0.5V	14.3	85.9	could not detected
100Cr6+0.3V	15.5	84.1	0.4

in vanadium and carbon. Elongated cementite precipitates are not seen in 100Cr6+0.5V and 100Cr6+0.3V steels unlike 100Cr6 which exhibits much higher numbers of cementite particles within its matrix. It is reasonable that cementite carbides were almost completely dissolved in 100Cr6+0.5V and 100Cr6+0.3V steels due to tempering at temperatures $>$ 723 °C [207] which is shown to be enough for cementite dissolution in vanadium bearing steels.

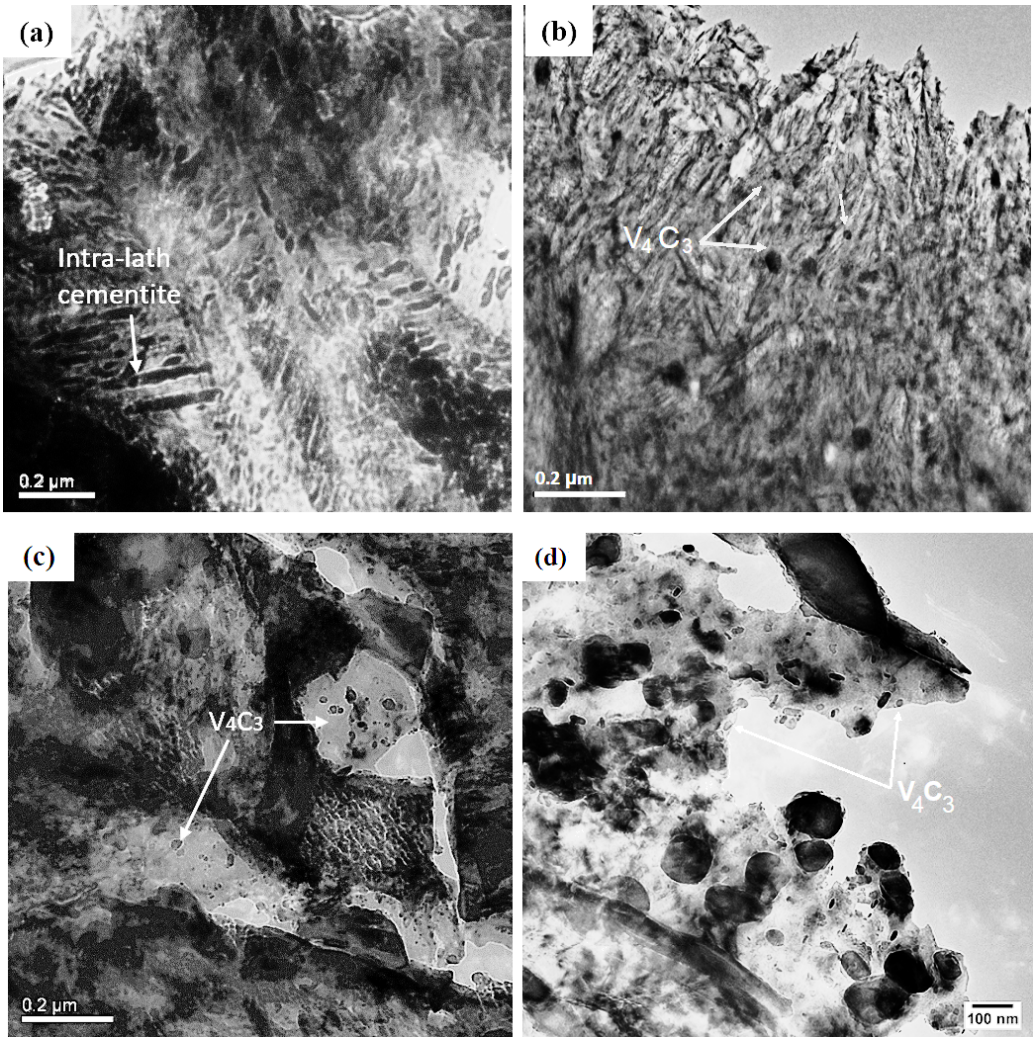

Figure 5.3: TEM bright field micrographs of tempered martensitic: a) 100Cr6 and b) 100Cr6+0.5V original HT, c) 100Cr6+0.3V, and d) 100Cr6+0.5V new HT. Arrows are pointing at V_4C_3 which appear as dark round and cuboid dots in vanadium bearing steels.

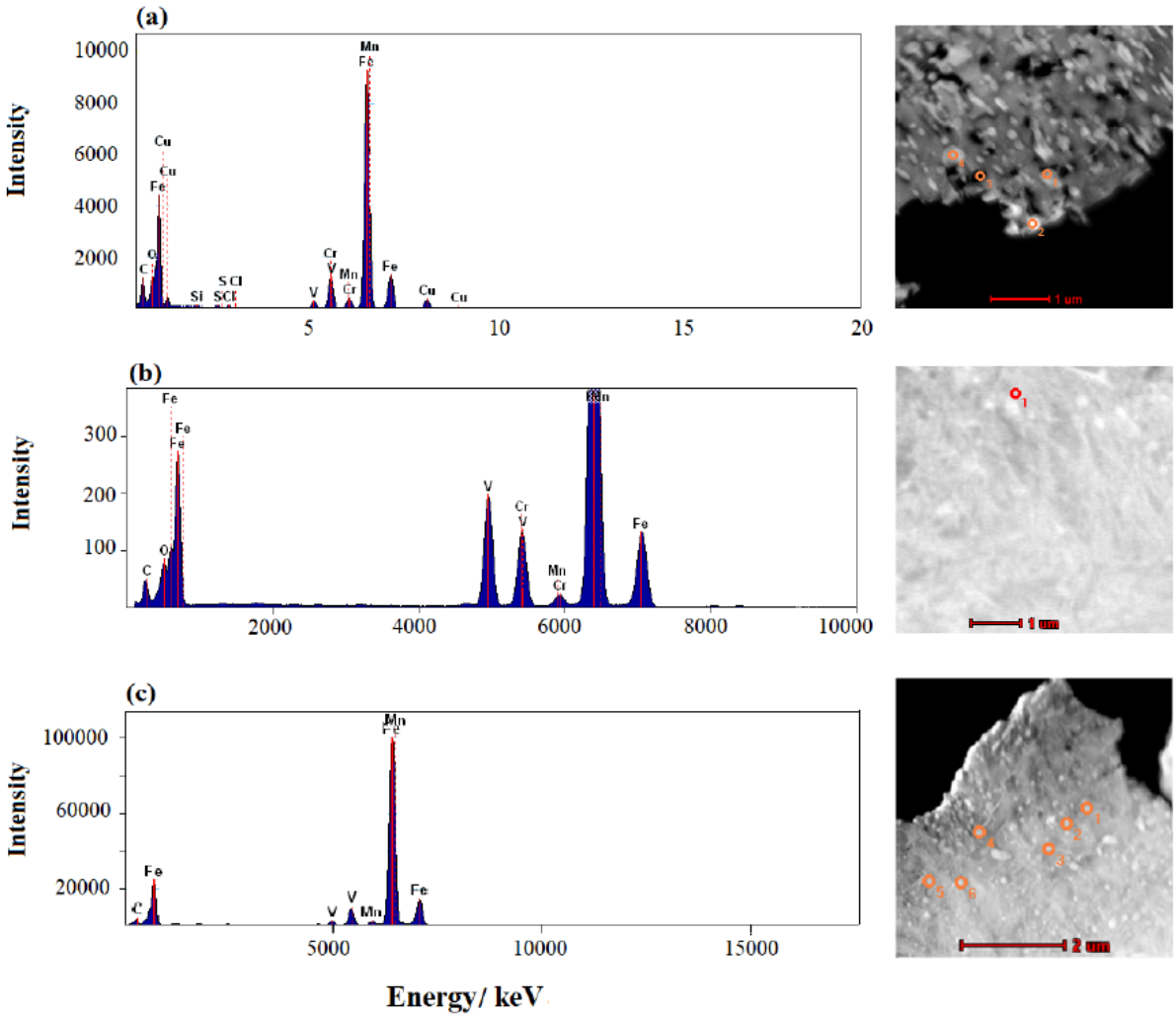

Figure 5.4: TEM with energy dispersive X-ray (EDX) results for V_4C_3 precipitates found in: a) 100Cr6+0.5V original HT, b) 100Cr6+0.3V, and c) 100Cr6+0.5V new HT.

100Cr6+0.5V heated according to original HT was chosen to identify the nanosize vanadium carbides in vanadium-bearing steel experimentally using atom probe tomography, as this technique offers a high spatial resolution required for accurate nanoscale chemical analysis. 100Cr6 steel was examined for comparison purposes.

For 100Cr6, atom maps in Figure 5.5 show carbon-rich regions which are highlighted by isosurfaces in Figure 5.6. An isosurface is a surface of interconnected voxels with the same composition or atomic density as defined by the APT user. In this study, it must be defined to calculate the carbide composition and the regions of higher and lower concentration of carbon. Despite their different morphologies, the carbon-rich regions revealed similar compositions of 72.1 Fe, 25.5 C, 1.4 Cr and 0.50 Si (in at.%), with low chromium segregation and silicon depletion as shown in Figure 5.7. The ratio of the highlighted carbides was very similar to the expected M_3C which suggests these precipitates are cementite. The most accurate method to calculate the volume fraction is to divide the number of precipitate atoms by the total number of atoms (from isosurface value). Accordingly, it is suggested that these particles are cementite with a volume fraction is 0.29 [190].

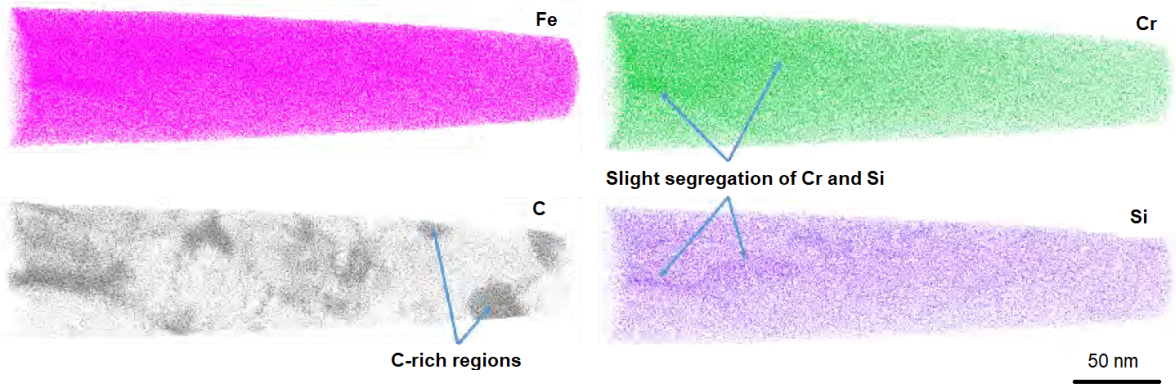

Figure 5.5: 100Cr6 atom maps show the iron matrix and carbon-rich regions and slight segregation in chromium and silicon [190].

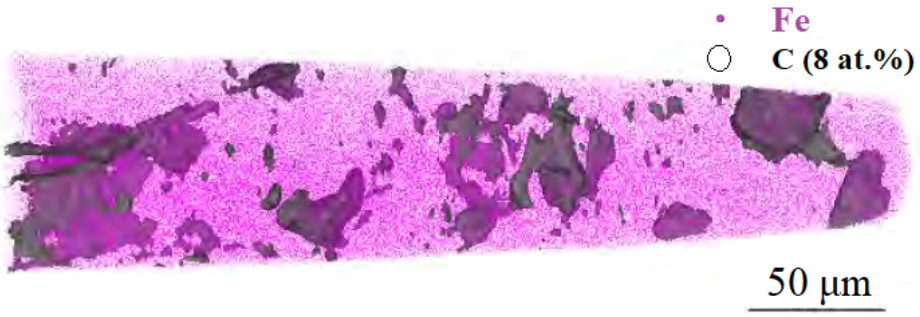

Figure 5.6: 100Cr6 atom map of iron, with an isosurface highlighting carbon-rich regions [190].

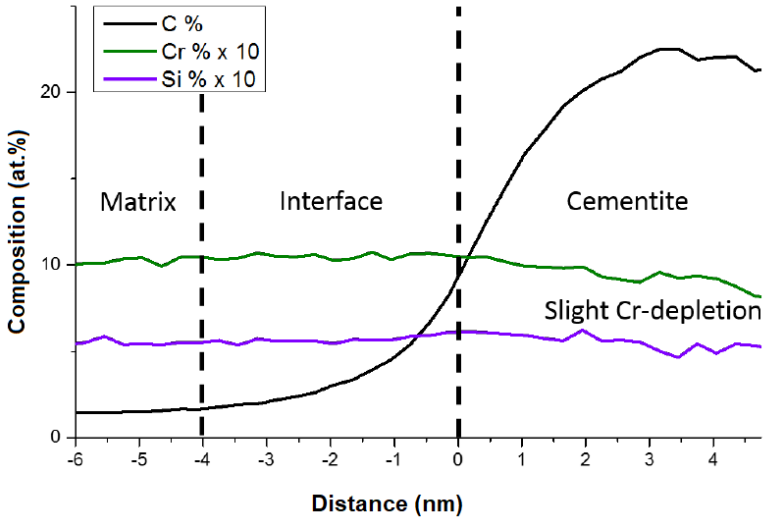

Figure 5.7: Proxigram of cementite in 100Cr6, showing chromium and silicon composition across the interface [190].

On the other hand, two large plate-like precipitates were found in the 100Cr6+0.5V specimen. The precipitates are rich in iron, carbon, chromium, and small spherical carbides containing vanadium and chromium. Vanadium, chromium and carbon were found segregating to a dislocation, Figure 5.8. Figure 5.9 reveals six vanadium-rich carbides in 100Cr6+0.5V with the chemical composition M_4C_3. The average vanadium carbide composition (in at.%) is: 43.0 C, 42.5 V, 6.3 Cr, 4.6 Fe, 1.3 N and 0.15 Mo. Nitrogen segregation occurs because it has a strong affinity for vanadium [208–210]. The average volume fraction of V_4C_3 was ~ 0.0081 [190] which is in a good agreement with the original calculations made by Szost [10]. It was also noted that 100Cr6+0.5V specimen contained a low volume fraction of cementite (less than 100Cr6) [190] since its heat treatment was designed to enhance the formation of fine cementite during the final tempering at 215 °C to ensure hardenability [11]. Finally, V_4C_3 had an average 5 nm radius size, Figure 5.10 [190] which is identical to the 10 nm size ideal for hydrogen trapping [92].

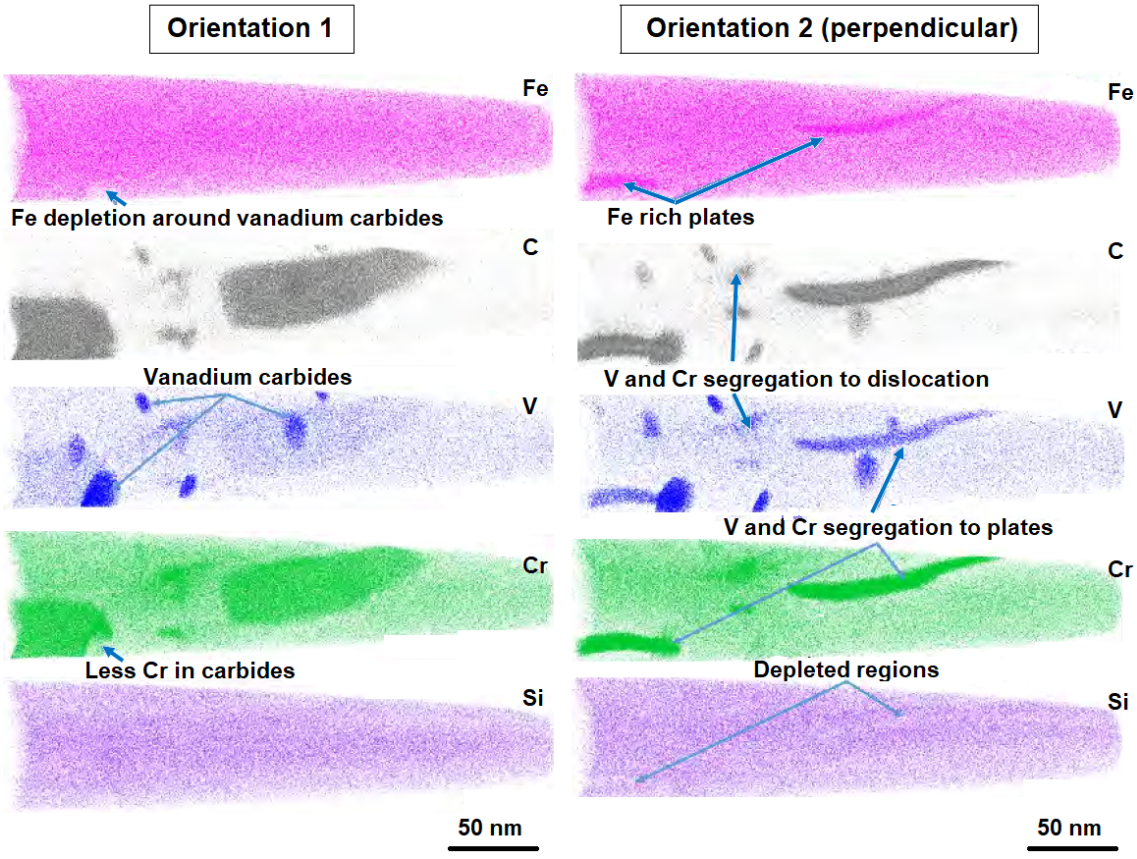

Figure 5.8: 100Cr6+0.5V atom maps in two perpendicular orientations, showing iron, carbon, vanadium and chromium segregation [190].

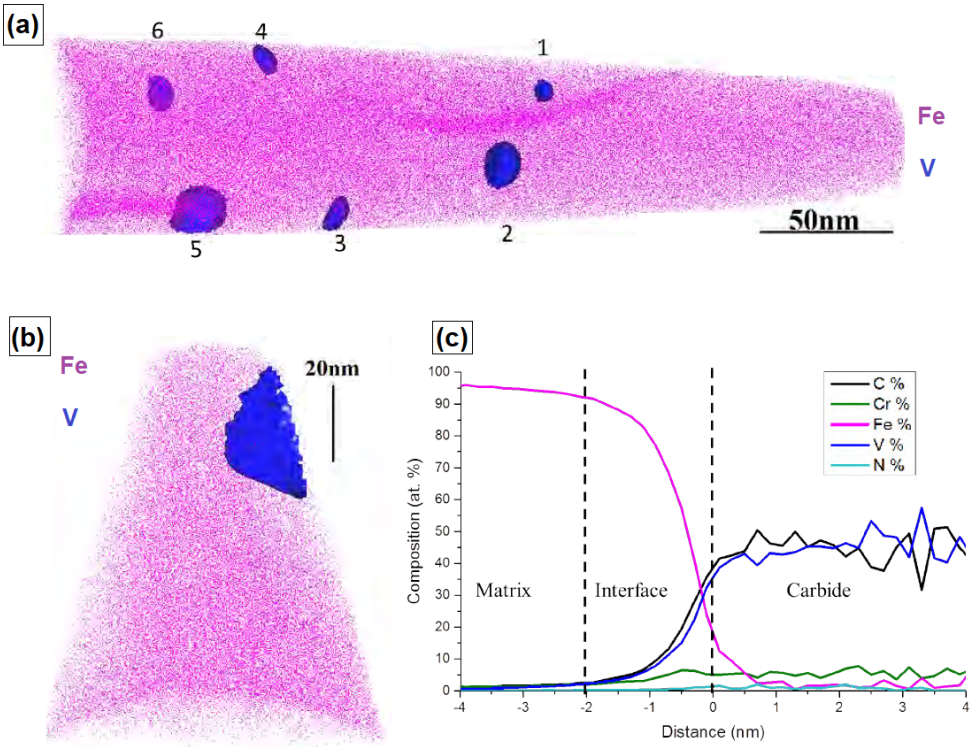

Figure 5.9: a) and b) Vanadium carbides in 100Cr6+0.5V specimen, and c) proxigram across the matrix/carbide interface [190].

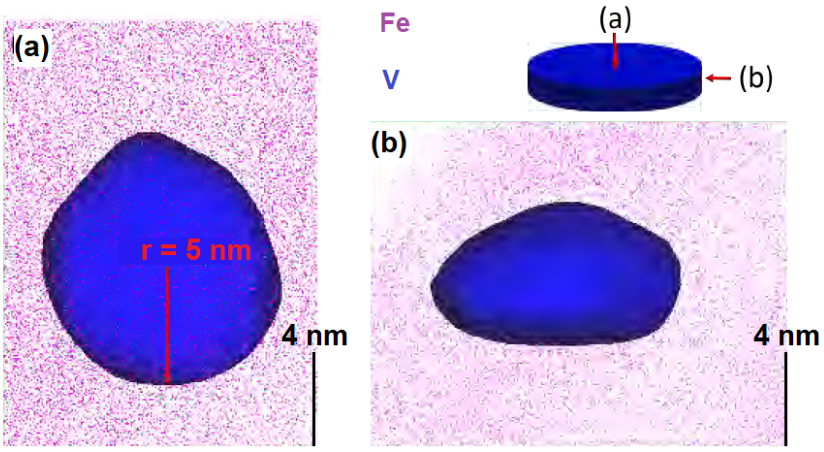

Figure 5.10: Side and top views of a vanadium carbide, with a schematic showing the image orientations [190].

5.1.2 Hydrogen trapping and de-trapping activation energy in bearing steels

Thermal desorption analysis (TDA) results for grades 100Cr6, 100Cr6+0.5V original HT, 100Cr6+0.5V new HT, and 100Cr6+0.3V are compiled in Figure 5.11. For 100Cr6, only 0.6 ppm hydrogen was trapped and the hydrogen peak was observed at 140 °C suggesting that dislocations are the main trapping sites [211] in 100Cr6 steel.

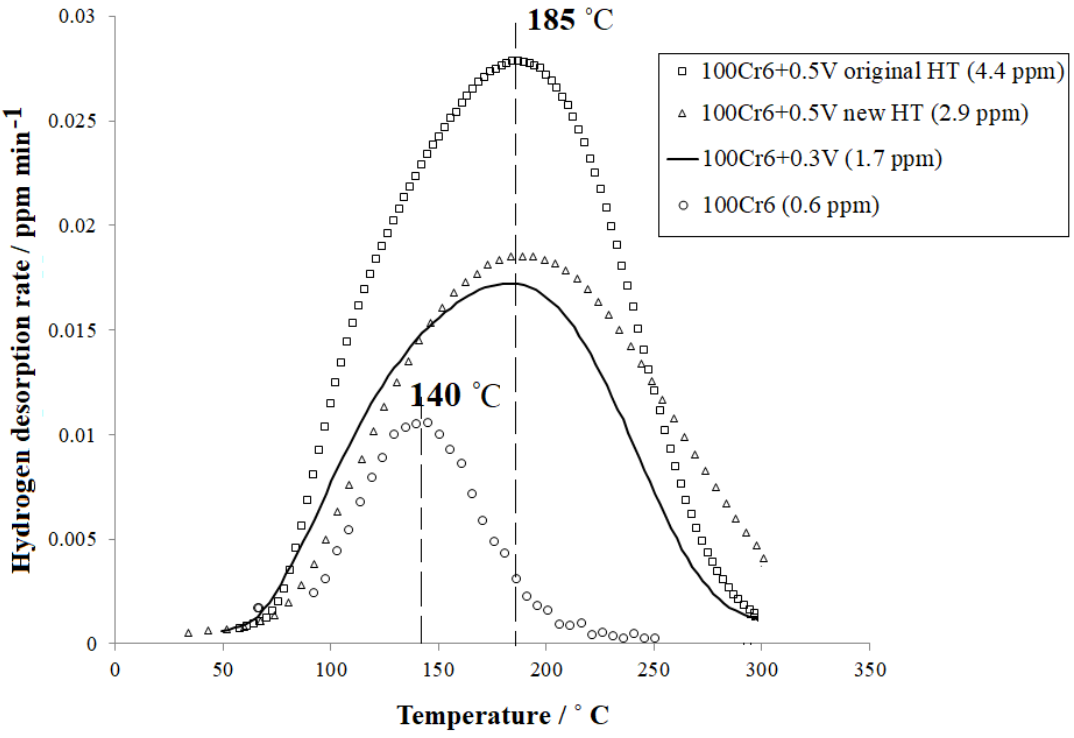

Figure 5.11: TDA profiles of trapped hydrogen for 100Cr6, 100Cr6+0.5V original HT, 100Cr6+0.5V new HT, and 100Cr6+0.3V specimens, each with the corresponding amount of trapped hydrogen. Charging time 5 days. TDA heating rate 50 °C h^{-1} to 285 °C.

It is believed that hydrogen is weakly trapped by the stress field generated by dislocation as explained by Takai *et al.*, causing microcracks to form during service [212, 213]. The most striking feature, however, that TDA peaks increased remarkably in vanadium-

containing steels. 100Cr6+0.5V original HT, 100Cr6+0.5V new HT, and 100Cr6+0.3V trapped 4.4, 2.9 and 1.7 ppm, respectively. Obviously, the amount of trapped hydrogen increased with increasing vanadium content in the steel since 100Cr6+0.5V steel has higher V_4C_3 precipitation contribution compared to 100Cr6+0.3V. V_4C_3 molar fraction is about 0.008 in 100Cr6+0.5V according to Szost [10] in comparison to 0.004 in 100Cr6+0.3V. This was described in sections 3.2.1 and 3.2.2.

The activation energies for hydrogen evolution from trapping sites were calculated for 100Cr6 and 100Cr6+0.5V steels. Three specimens of each steel were hydrogen charged for 5 days, then left at room temperature for 4 days for diffusible hydrogen to leave the specimens. Next, the activation energies (E_a) corresponding to the remaining hydrogen evolution peaks were calculated by the peak shift method using Kissinger equation [214], eq. 5.1:

$$\frac{\partial \ln(\phi/T_p^2)}{\partial \ln(1/T_p)} = \frac{-E_a}{R} \tag{5.1}$$

where ϕ is the heating rate, T_p the peak temperature, and R the gas constant.

The change of hydrogen evolution curves is indicated in Figure 5.12a. The hydrogen evolution rate appears smaller for lower heating rates because the sampling interval is constant (every three minutes) but the total evolved hydrogen amount is not [102]. According to equation 5.1, when ϕ/T_p^2 is plotted versus $1/T_p$ a straight line is obtained, with a slope equal to -E_a/R, Figure 5.12b.

It is reported that the de-trapping activation energy of dislocations is between 20 to 30 kJ mol^{-1} [13]. In this work, the activation energy obtained for 100Cr6 is 32.3 kJ mol^{-1}. Moreover, when considering the TDA temperatures, the peak at 140 °C corresponds to

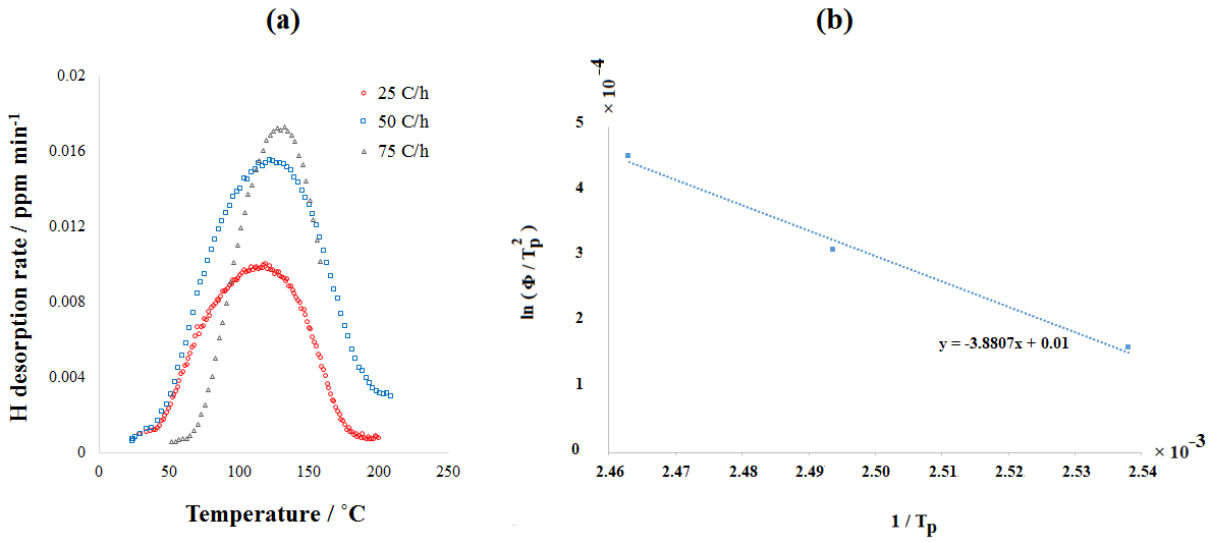

Figure 5.12: a) Change in hydrogen evolution curve with heating rate for 100Cr6. Charging time 5 days, b) determination of the de-trapping activation energy for de-trapping of 100Cr6.

trapping on dislocations in 100Cr6 [211]. Therefore, it is safe to conclude that the primary trapping sites in 100Cr6 are the dislocations in the martensitic structure.

Similarly, the de-trapping activation energy was calculated for vanadium-added steels. 100Cr6+0.5V with original HT was chosen for the calculation. Since V_4C_3 have stronger trapping potency, the de-trapping activation energy for 100Cr6+0.5V steel is expected to be higher and was found to be 35.2 kJ mol^{-1}, which is in good accordance with previously published finding [105].

5.1.3 Mechanical properties testing

Vickers hardness testing

Table 5.3 summarises the differences between the hardness of bearing steel grades studied in this work. The advantage of adding vanadium to 100Cr6 is clear from the increasing hardness. Although 100Cr6+0.3V contains a lower vanadium content, the obtained hardness of this steel is close to the hardness of 100Cr6+0.5V with original HT (751 versus 747 HV30). This is attributed to the heat treatment differences, as the newly designed treatments for both 100Cr6+0.3V and 100Cr6+0.5V have considered minimising coarse cementite in the final product.

Table 5.3: Summary of the hardness results for the studied bearing steels.

100Cr6	100Cr6+0.5V (original HT)	100Cr6+0.3V	100Cr6+0.5V (new HT)
725	747	751	765

Hydro-hardness and hydrogen embrittlement

In order to examine the nature of crack propagation and hydrogen embrittlement mechanisms in 100Cr6, 100Cr6+0.5V and 100Cr6+0.3V bearing steels, hydro-hardness technique was adapted from an earlier work [215]. It has been reported that hydrogen decreases the yield strength (YS) and ultimate tensile strength (UTS) in various materials [216, 217]. Yield strength and Young's modulus are related to the subsurface stresses induced by Vickers indentation [218]. However, in brittle materials a high YS to Young's modulus ratio results in cracking originating from the indentation. Consequently, without

the presence of hydrogen the indentation is not able to reach the tensile strength, and the indentations do not cause cracking [219]. 120 kg Vickers indentation was used here to induce cracks propagating from the indentation in a specimen of each steel: 100Cr6, 100Cr6+0.3V, and 100Cr6+0.5V (original HT). Indentations were applied before and immediately after hydrogen charging. Time between load and unload the 120 kg was around 12 to 13 seconds. Next, the specimens surfaces were observed under the optical microscope (OM).

The first group were observed after applying the indentation on hydrogen-free specimens, Figure 5.13. It is clear that the addition of vanadium to 100Cr6 has improved the strength since no cracks were observed in 100Cr6+0.3V and 100Cr6+0.5V steels, Figure 5.13b and c. **The second** group of the same steels were charged for 1, 2, and 3 days as described in section 4.1.2. Total hydrogen charges were 2.4, 15.0, and 15.5 ppm, respectively. Obviously, the total amount of hydrogen measured after charging for 2 and 3 days remains almost constant, which indicates that the specimens were saturated after 2 days of hydrogen charging. Immediately after charging, Vickers indentation was introduced at each specimen. The indented surface was observed by OM with a drop of an immersol (TM) 518F oil for the optical microscope put on the top of the specimen's surface. The oil drop boosts the formation of hydrogen bubbles around the cracks. Several observations were monitored in the hydrogen-charged case:

(1) Figure 5.14 shows that hydrogen in the microstructure (after 1 day of hydrogen charging) accumulates at the stressed cracks areas around the indentation, then diffuses out of the specimen, often follows the direction of the crack propagation. Embrittlement of vanadium-free 100Cr6 specimen was more pronounced for a relatively low average hydrogen content (2.4 ppm) with two long radial cracks formed on the surface.

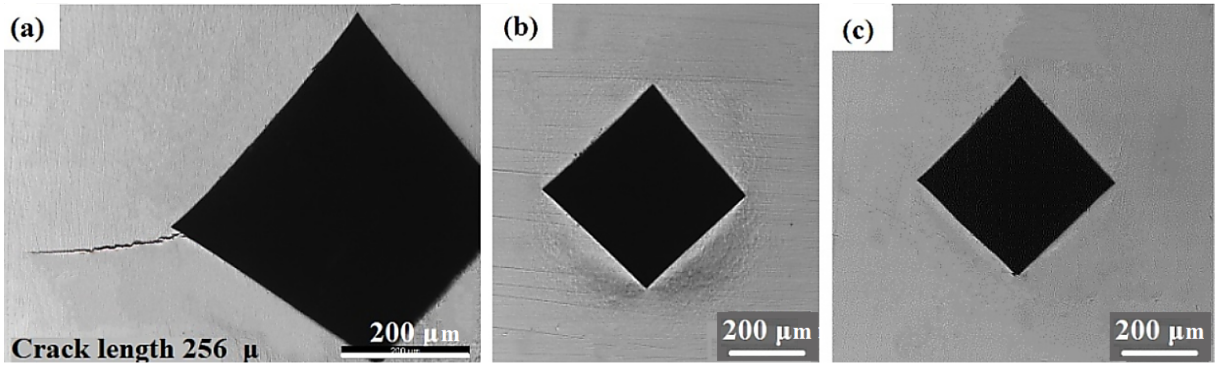

Figure 5.13: Hydro-hardness results without hydrogen charging for: (a) 100Cr6, (b) 100Cr6+0.3V, (c) 100Cr6+0.5V original HT. Load used 120 kg.

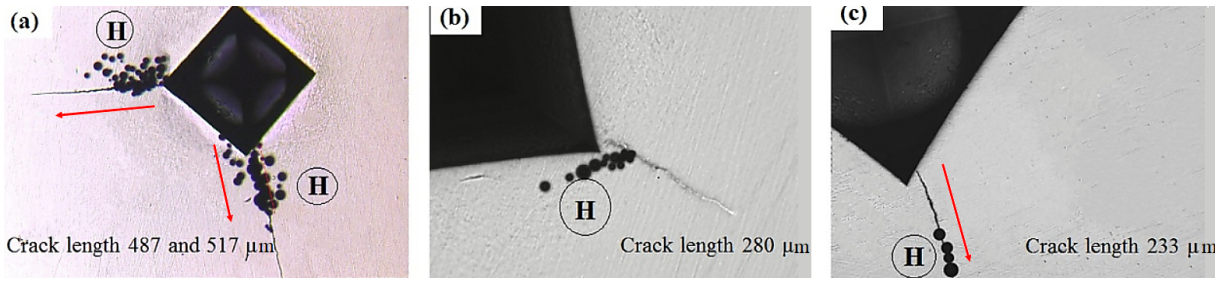

Figure 5.14: Hydro-hardness results just after hydrogen charging for 1 day and covering with immersion oil for: (a) 100Cr6, (b) 100Cr6+0.3V, (c) 100Cr6+0.5V original HT. Load used 120 kg. The arrows point to the crack propagation direction.

(2) For every charging period, the cracks lengths in the 100Cr6+0.5V and 100Cr6+0.3V steels are smaller than in 100Cr6 steel, Table 5.4. Moreover, the diffusion rate of the hydrogen bubbles from the cracks gradually decreases by increasing the vanadium content in the steel. For example, after charging for one day the hydrogen bubbling rates for 100Cr6, 100Cr6+0.3V and 100Cr6+0.5V were 140, 56 and 20 per minute, respectively. The results demonstrate that the more V_4C_3 traps in the material the more hydrogen is trapped and less diffusible hydrogen is found in the bulk.

Table 5.4: Cracks lengths (in μm) with respect to vanadium content and charging time.

	100Cr6	100Cr6+0.3V	100Cr6+0.5V
H-free	256	no cracks	no cracks
24 h charging	517 and 487	281	224 and 351
48 h charging	567, 595 and 646	169, 212 and 264	391
72 h charging	305, 693 and 880	331, 374 and 451	451, 628 and 798

(3) Although the presence of V_4C_3 in the steel reduces the amount of diffusible hydrogen and the crack length compared to the free-vanadium 100Cr6 steel, yet the crack length increases with increasing the charging time. The effect of charging time on HE is plotted in Figure 5.15. This could be ascribed to the supposition that the strong traps V_4C_3 tend to saturate immediately when hydrogen passes through [220], it follows that more diffusible hydrogen is still entering the steel and is free and mobile in the lattice and contributes to HE before they occupy the weak traps.

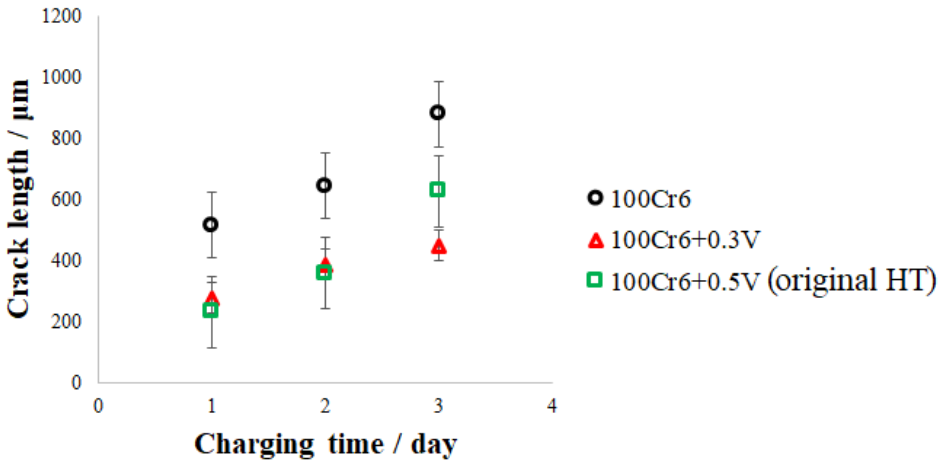

Figure 5.15: Cracks behaviour with respect to hydrogen charging time.

(4) However, the cracking behaviour of 100Cr6+0.3V and 100Cr6+0.5V (original HT) is of primary interest. Table 5.4 and Figure 5.16 show that 100Cr6+0.5V cracks became longer than in 100Cr6+0.3V even though the later has more cracks. Furthermore, 100Cr6+0.5V that was hydrogen charged for 1 day continued to crack as a new crack started to form within 20 minutes of ending the hydrogen charging and applying the indentation, Figure 5.17. The crack grew for about 5 minutes then stopped. Unexpectedly, after another 40 minutes, the same specimen developed a new crack from a point that is close to one of the indentation corners. The crack grew to 228 μm until it linked to the indentation corner in an opposite manner to the rest of the cracks as they tend to grow starting from the indentation corner toward the surrounding surface. The reason for this difference has not been clarified yet. One possibility to explain this behaviour is that 100Cr6+0.5V contains a higher density of V_4C_3 traps than 100Cr6+0.3V, this means more hydrogen is trapped into the former causing high internal pressure which generates high localised stress, hence initiating new cracks along weakness lines in the steel. This result is consistent with previous results by Elboujdaini and Revie [221] who asserted that crack initiation is a competitive process, cracks initiate at the most favorable sites first then at other sites.

(5) The same specimens were left to degas for 2 weeks at room temperature (RT). While some permanent damage remained, much of the embrittlement was recovered, Figure 5.18. 100Cr6+0.5V and 100Cr6+0.3V specimens that were charged for 1 day were fully recovered Figure 5.18d and g, unlike 100Cr6 that formed a single crack (partial recovery) Figure 5.18a. For the case of 2 and 3 charging days, all specimens recovered similarly with a single tiny crack in each steel. This finding is compatible with Duprez *et al.* work [153] who observed a different amount of ductility recovery on advanced high strength steels (AHSSs) when hydrogen charged tensile specimens were left one week in

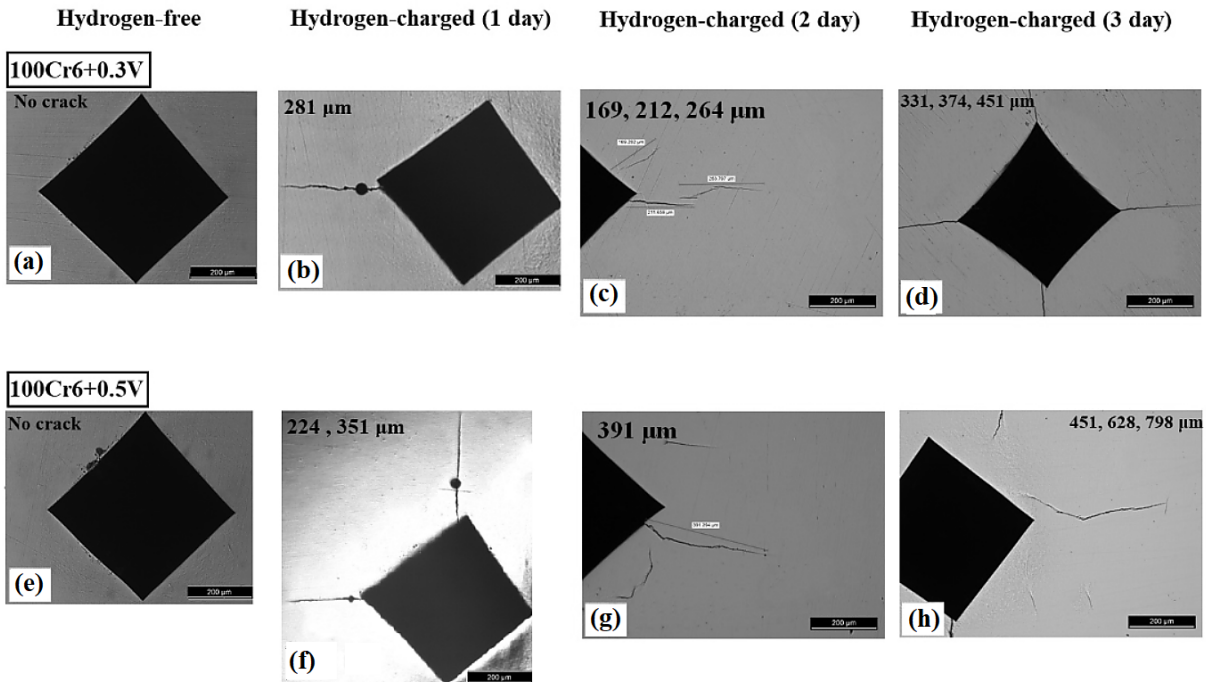

Figure 5.16: Cracks behaviour in 100Cr6+0.3V: a) H-free, H-charged for: b) 1 day, c) 2 days and d) 3 days, and in 100Cr6+0.5V original HT: e) H-free, H-charged for: f) 1 day, g) 2 days and h) 3 days. Load used 120 kg. OM magnification: 200 μm.

air before testing. Also, Depover and Verbeken [222] noted a full ductility recovery after 72 h of discharging tensile specimens and no internal cracks were observed in SEM analysis, which indicated that diffusible hydrogen was responsible for the ductility loss in AHSSs. A similar phenomenon has been noted by Hardie *et al.* [223] when charged high strength low alloy steels were left for 7 days at RT after hydrogen charging.

Tensile testing of 100Cr6 and 100Cr6+0.5V steels

Hydrogen embrittlement was evaluated by means of tensile test at room temperature under a sufficiently slow strain rate in order to allow hydrogen to homogeneously distribute to high

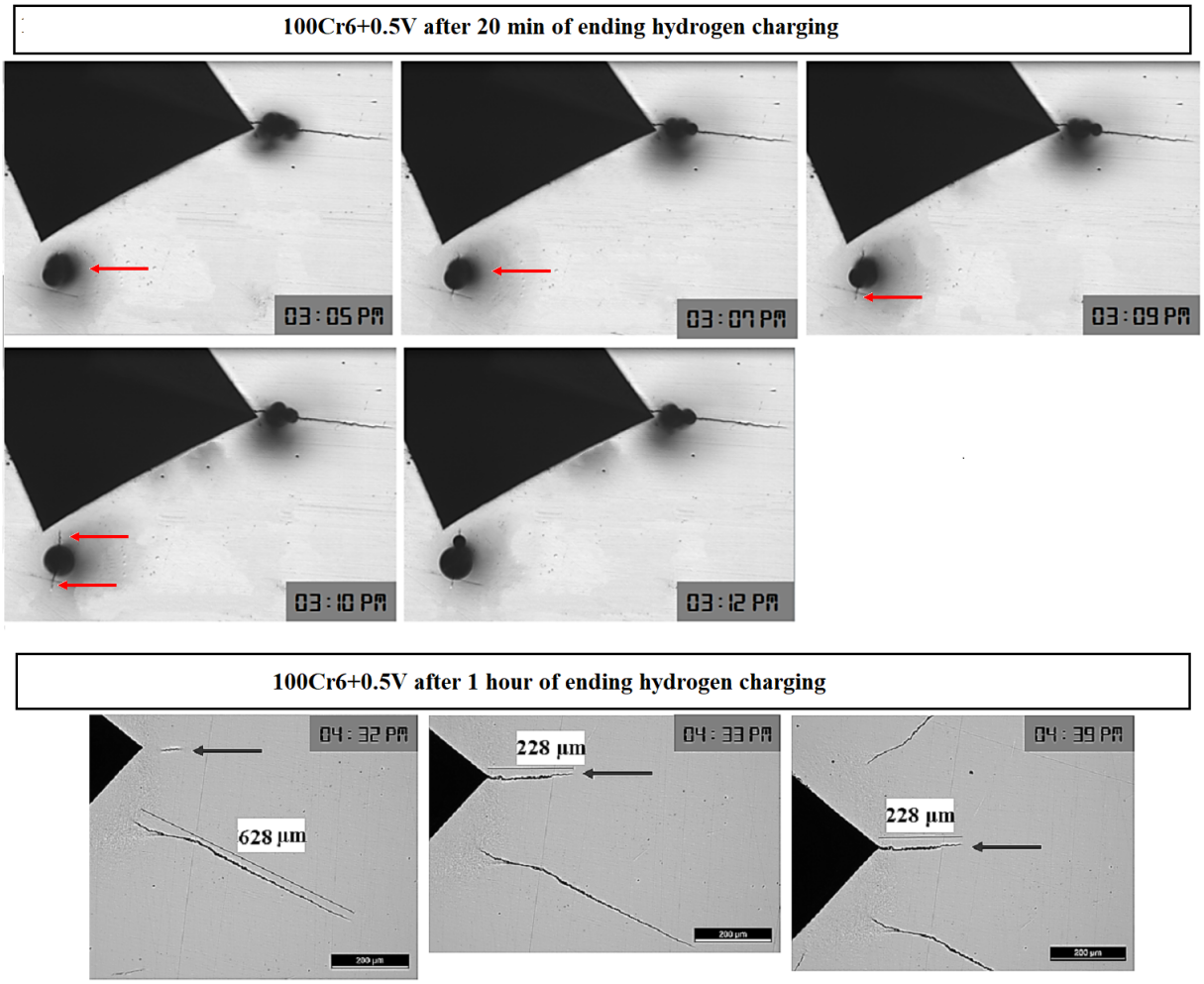

Figure 5.17: OM images showing cracks still forming and propagating after 20 minutes and 1 hour of ending the hydrogen charging. OM magnification: 200 μm

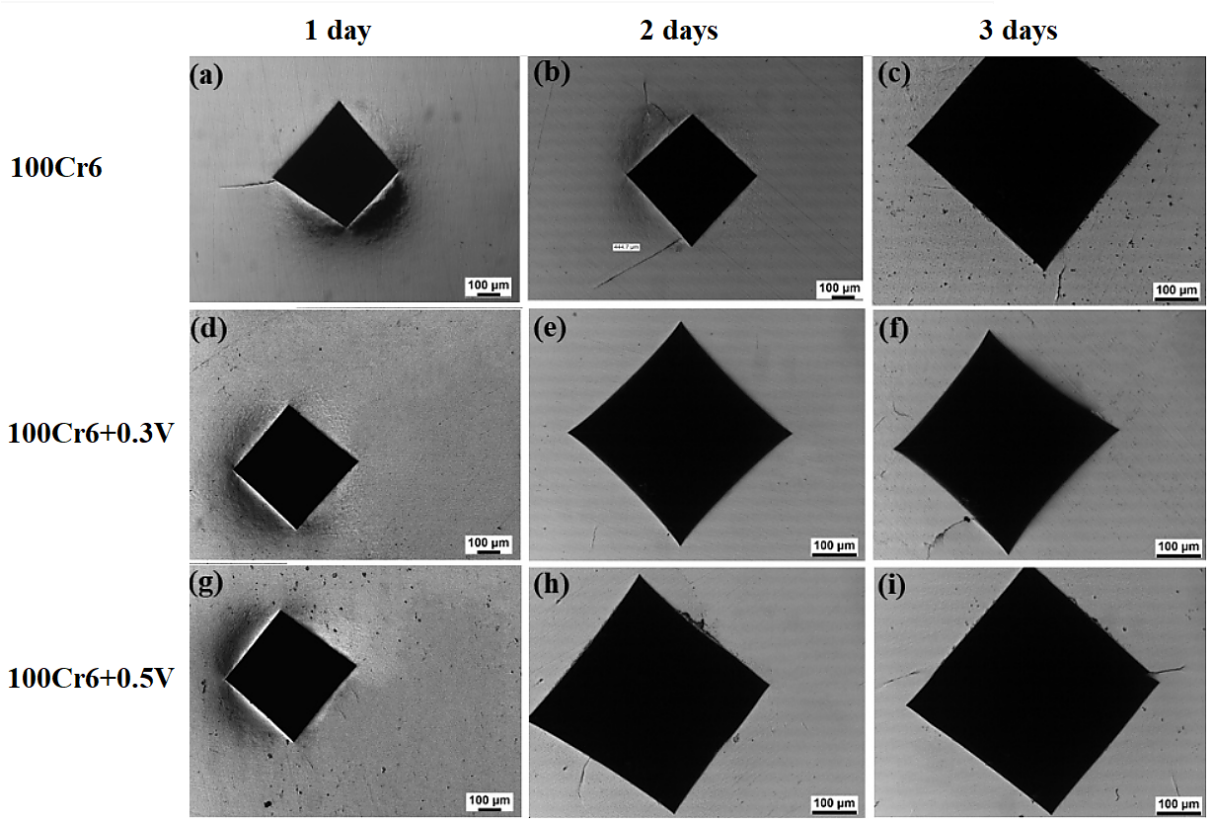

Figure 5.18: Evidence of recovery after two weeks of ending the hydrogen charging. 100Cr6 H-charged for: a) 1 day, b) 2 days and c) 3 days. 100Cr6+0.3V H-charged for: d) 1 day, e) 2 days and f) 3 days. 100Cr6+0.5V original HT H-charged for: g) 1 day, h) 2 days and i) 3 days. Load used 120 kg. OM magnification: 100 μm.

stress areas during the test. 100Cr6 steel (as reference) and 100Cr6+0.5V were tested under two conditions: hydrogen-free and 24 h hydrogen-charged. The test ended when tensile specimens failed. For each condition, one stress-strain curve was selected from three to demonstrate the effect of hydrogen charging. Preliminary results given in Figure 5.19 suggest that early failure was due to hydrogen and it was responsible of the reduction of fracture strain.

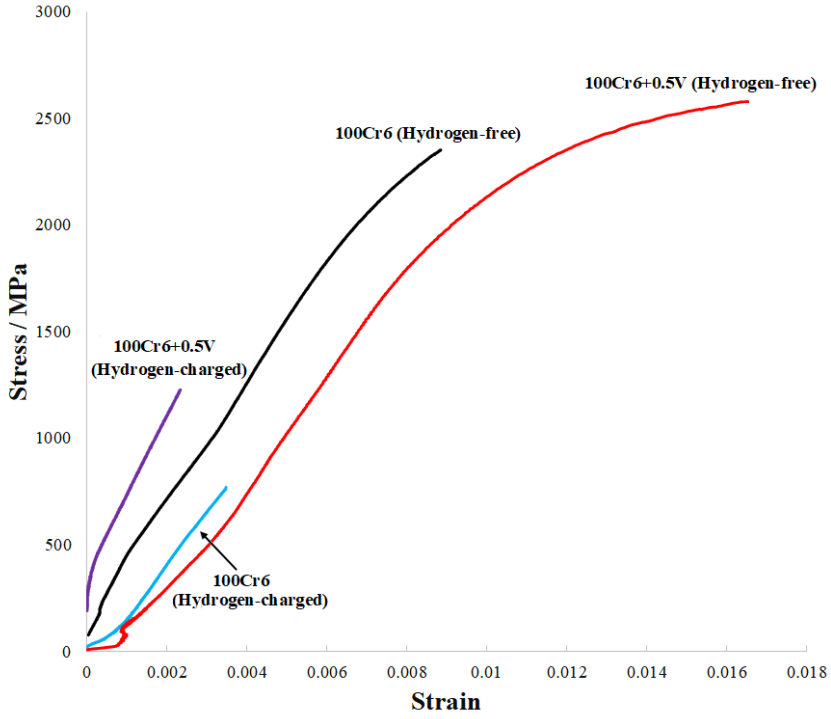

Figure 5.19: Engineering stress–strain curves of 100Cr6 and 100Cr6+0.5V steels straining in air, free and 24 hours hydrogen charged.

The hydrogen-free specimens exhibited continuous yielding and a total strain to failure (total elongation) of 0.9 % and 1.7 % for 100Cr6 and 100Cr6+0.5V, respectively. The ultimate tensile stresses are 2352 MPa for 100Cr6 and 2577 MPa for 100Cr6+0.5V, with corresponding yield strengths of 1812 MPa and 1863 MPa, respectively. It should be pointed out that it was not possible to use the 0.2 percent offset method as the yield stress because of the distortion at the beginning of each curve which was caused by the

movements of the specimens at the beginning of the test until they fully stabilised inside the collets with increasing the tension. Instead, the yield stresses were measured from the point where the curve deviates from the straight line. These results demonstrated that the addition of vanadium enhanced the strength and ductility as the elongation of 100Cr6+0.5V specimen at failure is about 88.8 % higher than the elongation of 100Cr6.

On the contrary, after hydrogen charging, the strain yielding behaviour changed. Although saturation with hydrogen was not achieved, as each specimen (weighs 60 grams) was charged with only 3.6 ppm after 24 h charging, still a small amount of hydrogen caused a remarkable reduction in the tensile strength for all hydrogen-charged specimens, and as a result, brittle fractures occurred in both steels at stresses below the yield strength, which is said to reflect hydrogen embrittlement susceptibility. Hydrogen-charged 100Cr6 specimens were severely embrittled by hydrogen in that UTS dropped from 2252 to 769 MPa. In 100Cr6+0.5V specimens, although a clear reduction was observed in the fracture strain, this steel exhibited better resistance to hydrogen embrittlement with an UTS reduction from 2577 MPa to 1243 MPa. However, the total strain to failure significantly decreased in both steels, from 0.9 % to 0.3 % for 100Cr6 and from 1.7 % to 0.2 % for 100Cr6+0.5V. The results are summarised in Table 5.5. Li and coworkers [224] reported that hydrogen traps stimulated hydrogen absorption from the environment causing a decrease in the fracture stress of their studied 1700-MPa-class ultrahigh-strength steel.

Table 5.5: Summary of tensile test results of 100Cr6 and 100Cr6+0.5V steels.

	Yield strength (MPa)	UTS (MPa)	Ductility (%)
100Cr6 (hydrogen-free)	1812	2252	0.9
100Cr6+0.5V (hydrogen-free)	1863	2577	1.7
100Cr6 (hydrogen-charged)	brittle failure occurs before yielding	769	0.3
100Cr6+0.5V (hydrogen-charged)	the brittle failure occurs before yielding	1243	0.2

For further investigations on hydrogen embrittlement susceptibility of the studied steels, SEM observations were carried out on the fracture surfaces of longitudinal cross sections of the elongated gage of hydrogen-charged 100Cr6 and 100Cr6+0.5V. In general, both steels revealed a large fish-eye surrounded by a quasi-cleavage zone, Figure 5.20. The literature reports that the fish-eye is observed in steels fractured under tensile stress when the strain becomes greater than the elastic limit of the hydrogen-charged steels, often originated from the largest defects present [225]. However, the fracture surface of 100Cr6 in Figure 5.20a appeared with a diverse range of voids, while the fracture surface of 100Cr6+0.5V in Figure 5.20b appeared to be dominated by small dimples.

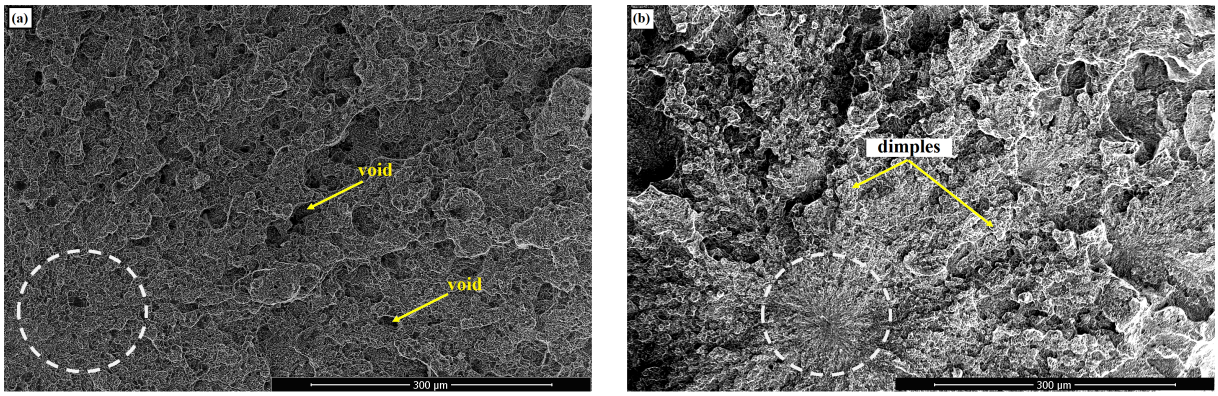

Figure 5.20: General view at low magnification of hydrogen-charged bearing steel fracture surface showing fish-eye in: a) 100Cr6 and b) 100Cr6+0.5V. The dashed circles indicate origin of fracture.

To illustrate the embrittlement caused by hydrogen, observations at a higher magnification on the fish-eye zones for both steels showed a mixture of intergranular ductile dimples and transgranular brittle cleavages, Figure 5.21. Figure 5.21a of the hydrogen-free 100Cr6 specimen revealed that the fracture is dominated by numerous brittle cleavages surrounding fewer ductile areas. The cleavage cracks appeared as straight areas with global fracture surfaces and river pattern strips on the fracture surface, as described by

Chen and Cao [226]. Also, the large void in Figure 5.21a contributes to the fracture growth as it coalesces with newly formed voids causing the fracture to grow further until it reaches the steel surface leading to surface crack [227]. After hydrogen charging the ductile areas almost disappeared and the crack surface transfered into typically transgranular brittle fracture just as shown in Figure 5.21c, which reflects the strong detrimental influence of hydrogen embrittlement in the vanadium-free steel.

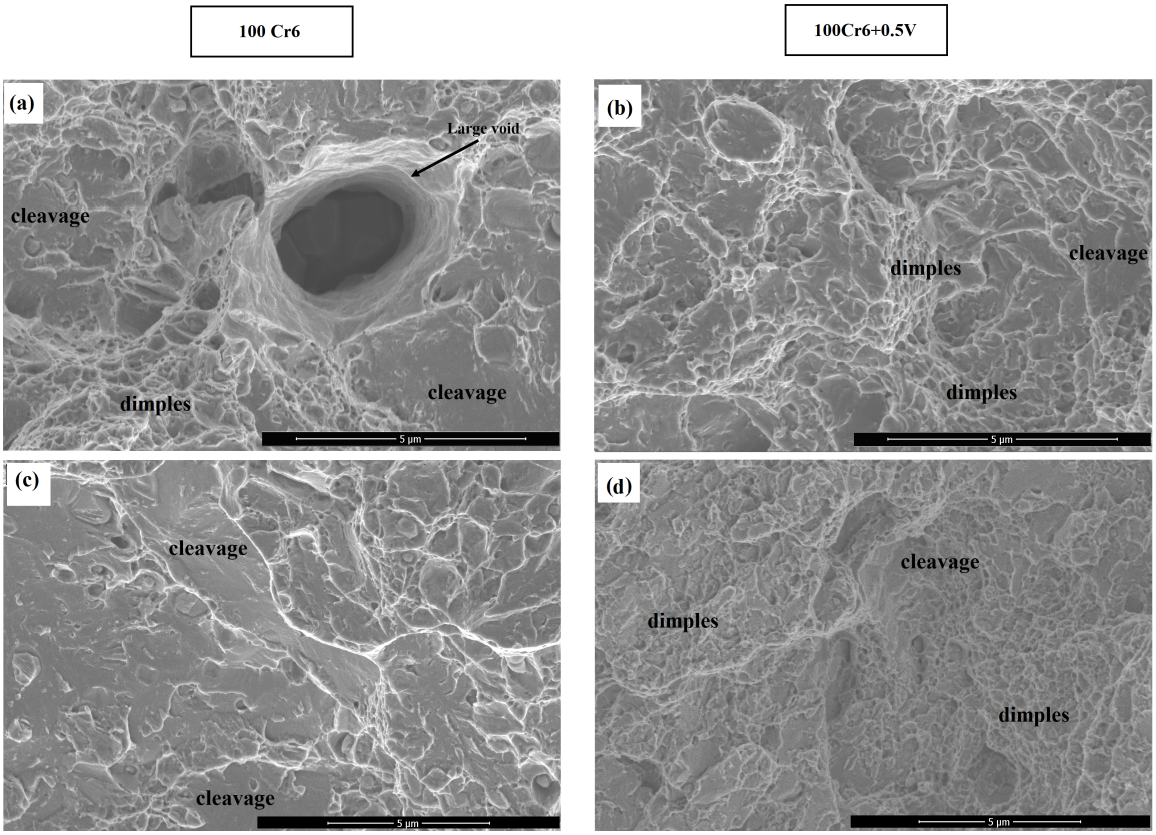

Figure 5.21: SEM fractography of the aureole of the fish-eye zone in: hydrogen-free a) 100Cr6 and b) 100Cr6+0.5V, and in 24 h hydrogen-charged c) 100Cr6 and d) 100Cr6+0.5V.

On the other hand, and despite the hydrogen-charged 100Cr6+0.5V tensile specimens failing at relatively low loads, their fractography showed an interesting behaviour. The fracture pattern of the charged specimen in Figure 5.21d shows a few tiny brittle regions

in the fracture crack propagation path isolated by widely spread ductile regions indicating that the specimen failed in a ductile manner. Furthermore, the dimples in 100Cr6+0.5V specimens were much finer than those in 100Cr6 as the formation of large-size dimples is related to brittle as stated by Sun *et al.* [228]. The fracture is generally intergranular and resulted of separation of the grain boundaries, therefore, the HEDE mechanism [38, 39] should be responsible for the hydrogen-induced fracture of the vanadium-added steel under the hydrogen charging. The fracture morphology of the crack is a typical indication that adding vanadium to the 100Cr6 alloy enhanced the material and reduced the transition from ductile to brittle fracture due to hydrogen embrittlement.

SEM/EDX of fractured specimens disclosed that damage is mainly triggered by non-metallic inclusions (NMIs) in 100Cr6 and by coarse cementite in 100Cr6+0.5V, Figure 5.22. MnS and SiO_2 type inclusions were found in the fracture subsurface of 100Cr6. EDX spectra obtained from several particles in 100Cr6 specimens confirmed manganese- and sulfides- rich particles, Figure 5.22a, and oxide regions rich with silicon, Figure 5.22b. In 100Cr6+0.5V steel, fractures mostly originated from elongated carbon-rich particles suggested to be coarse cementite as demonstrated in Figure 5.22c. When inclusions are very close to the steel surface, the quasi-cleavage area reaches the steel surface straightway causing the crack to occur even before it reaches the ductile to brittle transition [227]. Such inclusions are a significant issue for bearing applications and lead to delayed failure [81] as proved in this study because the interfaces between large inclusions/particles and matrix are preferable locations to accommodate hydrogen.

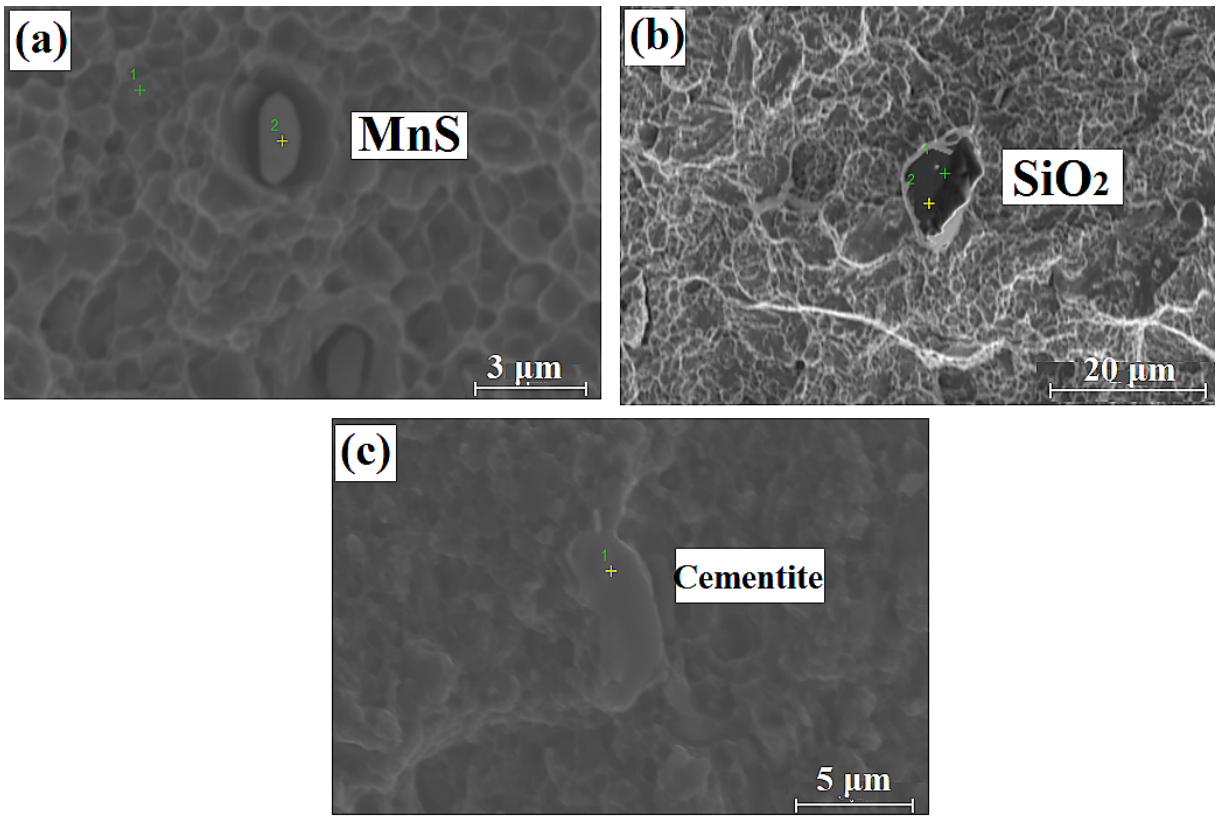

Figure 5.22: SEM images of NMIs observed in: a and b) 100Cr6, c) 100Cr6+0.5V steels.

Rolling contact fatigue results

This work represents the first systematic experimental study for the effect of vanadium on 100Cr6 bearing life. Rolling contact fatigue (RCF) experiments were conducted on 100Cr6 and 100Cr6+0.5V under two conditions, hydrogen-free and 24 h hydrogen-charged. No test was suspended, all specimens failed after different periods of time. After each RCF test, small sections were cut across the raceway to investigate the presence of butterflies, Figure 5.23. These small sections were then cut into halves to expose a plane parallel to the raceway then hot mounted in bakelite resin mounts.

The results obtained from RCF tests for uncharged and charged 100Cr6 and 100Cr6+0.5V steels are summarised in Table 5.6 and Figure 5.24. Data are displayed in a decreasing order for the number of stress cycles. Although hydrogen-charged 100Cr6+0.5V rods,

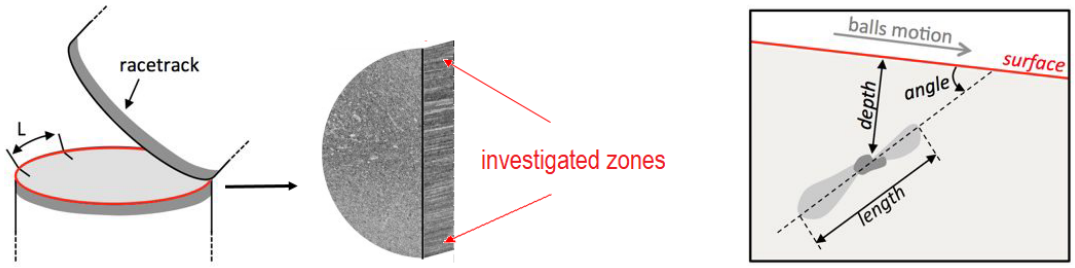

Figure 5.23: Schematics showing sectioning method to study the microstructural transitions during rolling contact fatigue of 100Cr6 and 100Cr6+0.5V steels [229].

Figure 5.24b experienced early stage damage before and after hydrogen charging, the highest embrittlement index was measured for the vanadium-free 100Cr6 steel, Figure 5.24a, meaning that the hydrogen charging had a detrimental effect on the vanadium-free alloy in comparison to 100Cr6+0.5V. The results of charged 100Cr6 rods measured under the same conditions were nearly identical with the bearing life dropping by 99 % for almost all the tests. Interesting results were obtained for 100Cr6+0.5V steel. This high strength alloy containing V_4C_3 precipitates showed longer life with 5.6 ppm trapped hydrogen although it failed in a shorter time and estimated reduction in life ranges between 25 % to maximum 60 %. It should be taken into account that this alloy contains coarse cementite which was described in section 5.1.3 and it was expected that RCF rods will follow a similar trend. Nonetheless, the results demonstrate that V_4C_3 in 100Cr6+0.5V increase the resistance to hydrogen-enhanced failure by RCF.

The microstructure beneath the raceway has been visualized by OM and SEM. The micrographs in Figure 5.25 show examples of typical early surface initiated microcracks found on RCF specimens of hydrogen-charged 100Cr6 and 100Cr6+0.5V as a consequence of rolling contact testing. 100Cr6 failed at a very early stage ending with spall formation after 0.3×10^6 cycles. No surface microcracks were observed. In the 100Cr6+0.5V case, it

Table 5.6: Summary of RCF results for hydrogen-free and hydrogen-charged 100Cr6 and 100Cr6+0.5V in a decreasing order. Number of stress cycles is in millions.

Test number	100Cr6 H-free	100Cr6 H-charged	100Cr6+0.5V H-free	100Cr6+0.5V H-charged
1	88	0.4	6.3	3
2	50.4	0.3	4.3	2.1
3	39.9	0.08	3.0	2.0
4	31.5	0.05	2.9	1.9
5	29	0.03	2.2	1.8
6	28.9	0.02	2.1	1.6
7	28.1	0.01	1.8	1.3
8	19.3	0.01	1.8	1.1
9	-	-	1.8	1.1
10	-	-	1.7	0.9
11	-	-	1.4	0.8
12	-	-	1.0	0.4
13	-	-	0.9	-

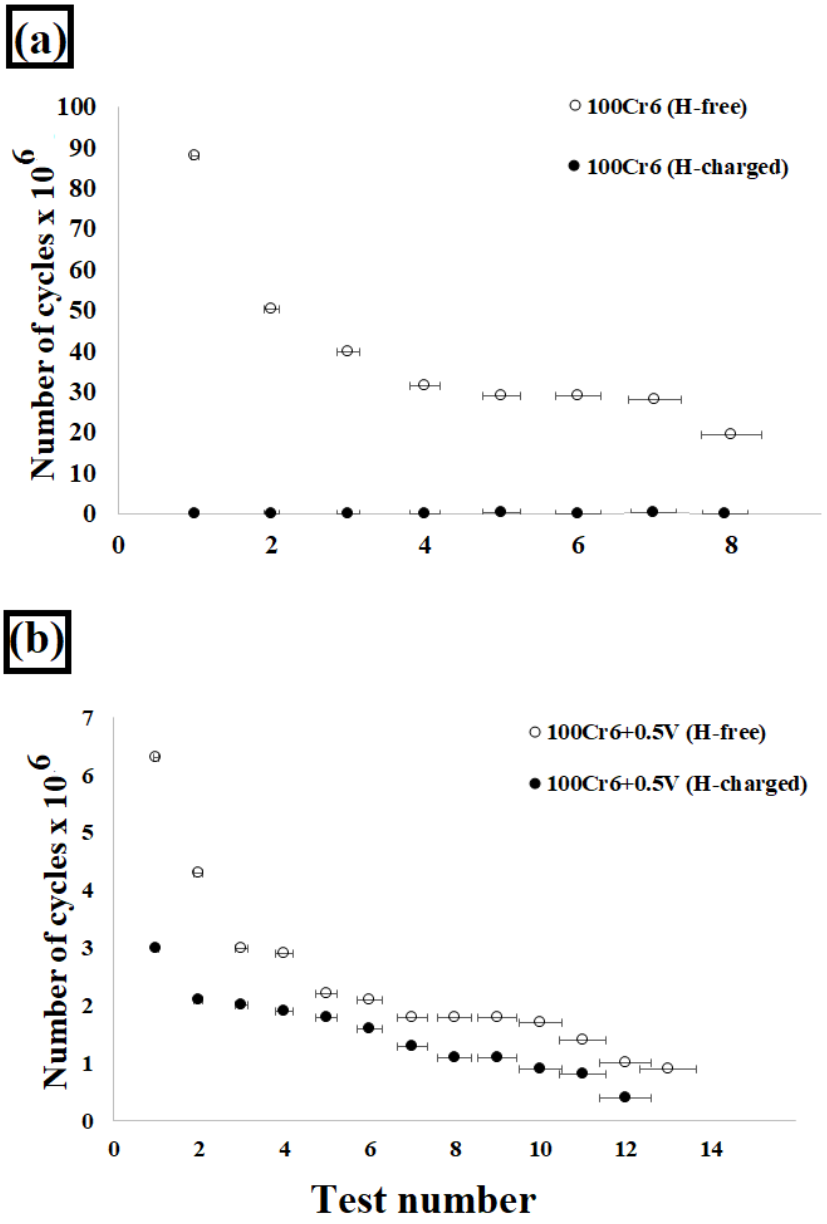

Figure 5.24: RCF results of hydrogen-free and hydrogen-charged: (a) 100Cr6, and (b) 100Cr6+0.5V steels. Data are plotted in a diminishing manner of bearing life.

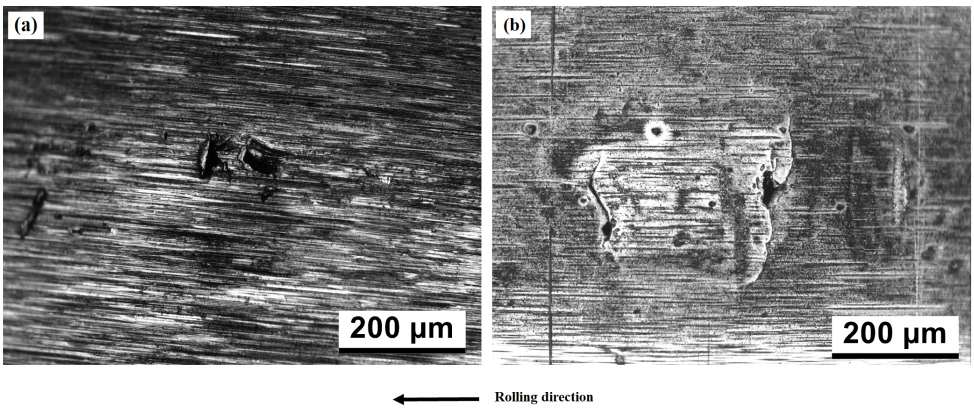

Figure 5.25: Optical images of RCF raceway from hydrogen-charged: a) 100Cr6 failed after 0.3 $\times 10^6$ cycles, and b) 100Cr6+0.5V failed after 3.0×10^6 cycles.

is clear that the spalling formation started with several microcracks growing perpendicular to the rolling direction before the specimen failed after 3.0×10^6 cycles.

Metallographic sections were prepared to study the microstructural evolution during rolling contact fatigue for both steels in hydrogen free and charged conditions. For 100Cr6 specimens it was not possible to detect any details under OM, so the specimens were placed under the SEM. Here the micrographs revealed very tiny microcracks in the range of 10 μm and less. SEM/EDX confirmed carbon rich points suggesting that the white etching areas (WEAs) formed around cementite particles, Figure 5.26. After hydrogen charging some microcracks were observed propagating from rolling contact surface, Figure 5.27a. Higher numbers of WEAs were found distributed around cementite particles, Figure 5.27b,c and d. Their sizes were also about 10 μm or less. Sub-surface morphology of hydrogen-free 100Cr6+0.5V specimens revealed fine cracks in the depth of 164 μm below the raceway, Figure 5.28. The microcrack length averaged between 12 to 26 μm.

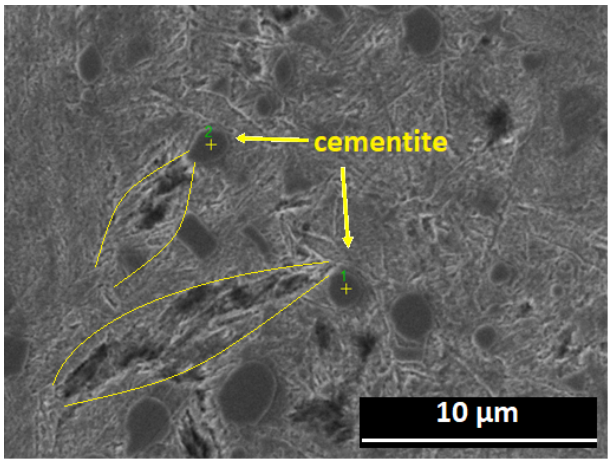

Figure 5.26: SEM showing WEAs forming around cementite particles at the subsurface of hydrogen-charged 100Cr6.

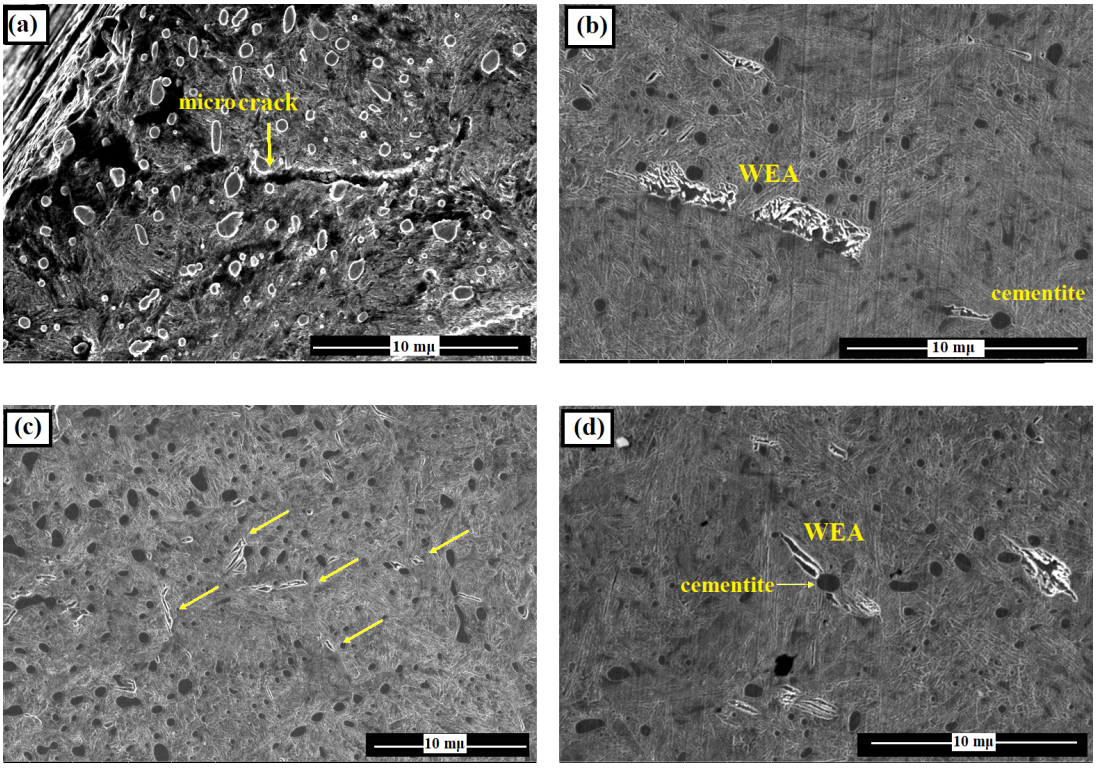

Figure 5.27: SEM showing WEAs forming around cementite particles at the subsurface of hydrogen-charged 100Cr6.

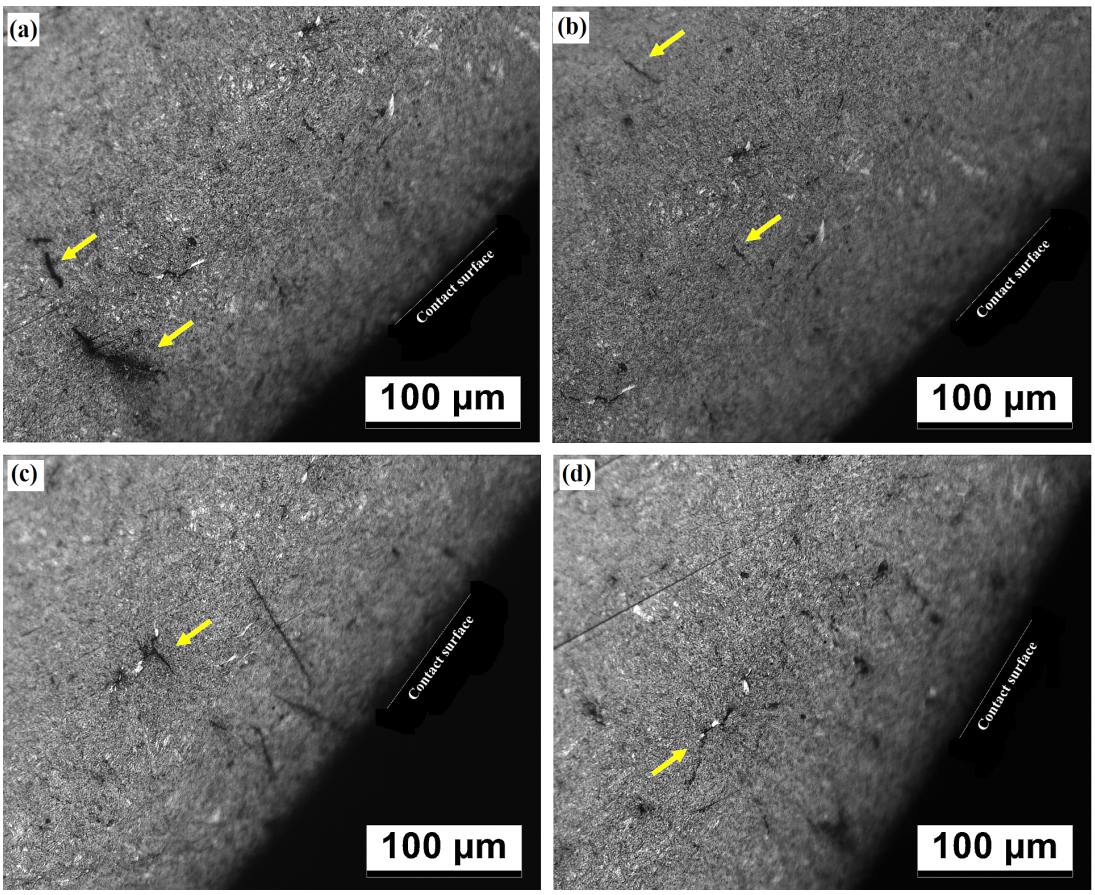

Figure 5.28: Optical microscope showing early surface microcracks observed below the raceway of a hydrogen-free 100Cr6+0.5V specimen. The images are taken from different zones below the raceway and the microcracks are indicated by yellow arrows.

On the other hand, longer and near to surface microcracks were seen at a depth of 62 to 72 μm after hydrogen charging, with a single deep microcrack found 133 μm below the raceway in only one specimen Figure 5.29. The microcracks were about 23 to 45 μm long, with some microcracks observed to propagate and link with the surface, Figure 5.29a. In terms of microcracks sites, microcracks occurred in defect-free locations in hydrogen-free specimens, with few being associated with inclusions. The hydrogen-charged specimens followed an opposite trend as almost all microcracks formed around inclusions. It was also noticed that few microcracks propagated into a star-like form around the inclusions.

In addition, higher number of WEAs/butterflies were observed in 100Cr6+0.5V con-

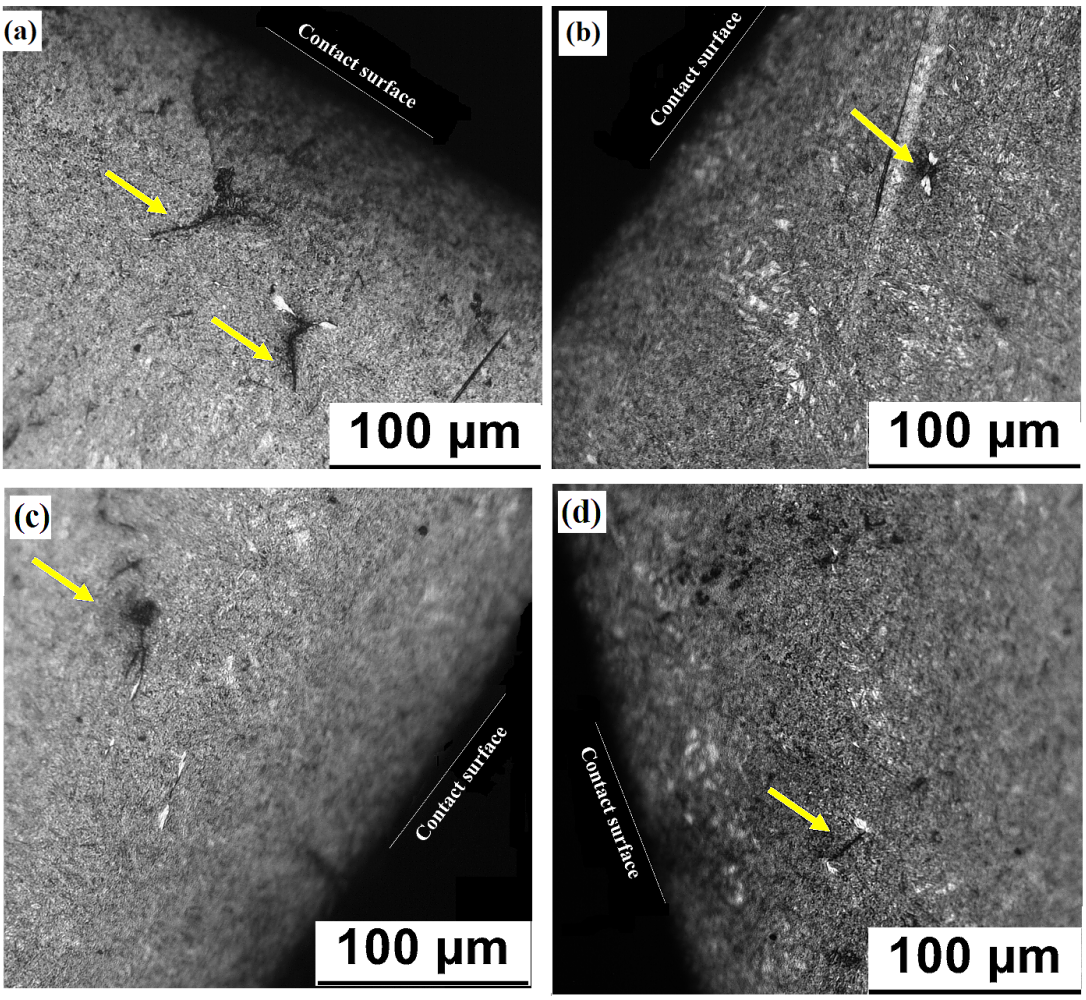

Figure 5.29: Optical microscopy images showing early surface microcracks observed below the raceway of a hydrogen-charged 100Cr6+0.5V specimen. The images are taken from different zones below the raceway and the microcracks are indicated by yellow arrows.

taining hydrogen Figure 5.30, and in some locations were grouped in a large network, Figure 5.30d. Long butterflies sized between 20 to 66 μm were found at about 30 to 60 μm under the raceway, in comparison with smaller butterflies sized 10 μm that were found deeper at about 85 μm under the raceway in hydrogen-free specimens. In both cases, butterflies were oriented between 20° to 40° with respect to the rolling direction. The frequent association between inclusions and microcracks in hydrogen-charged specimens strongly indicates that damage is more likely to appear earlier and is initiated by

NMIs.

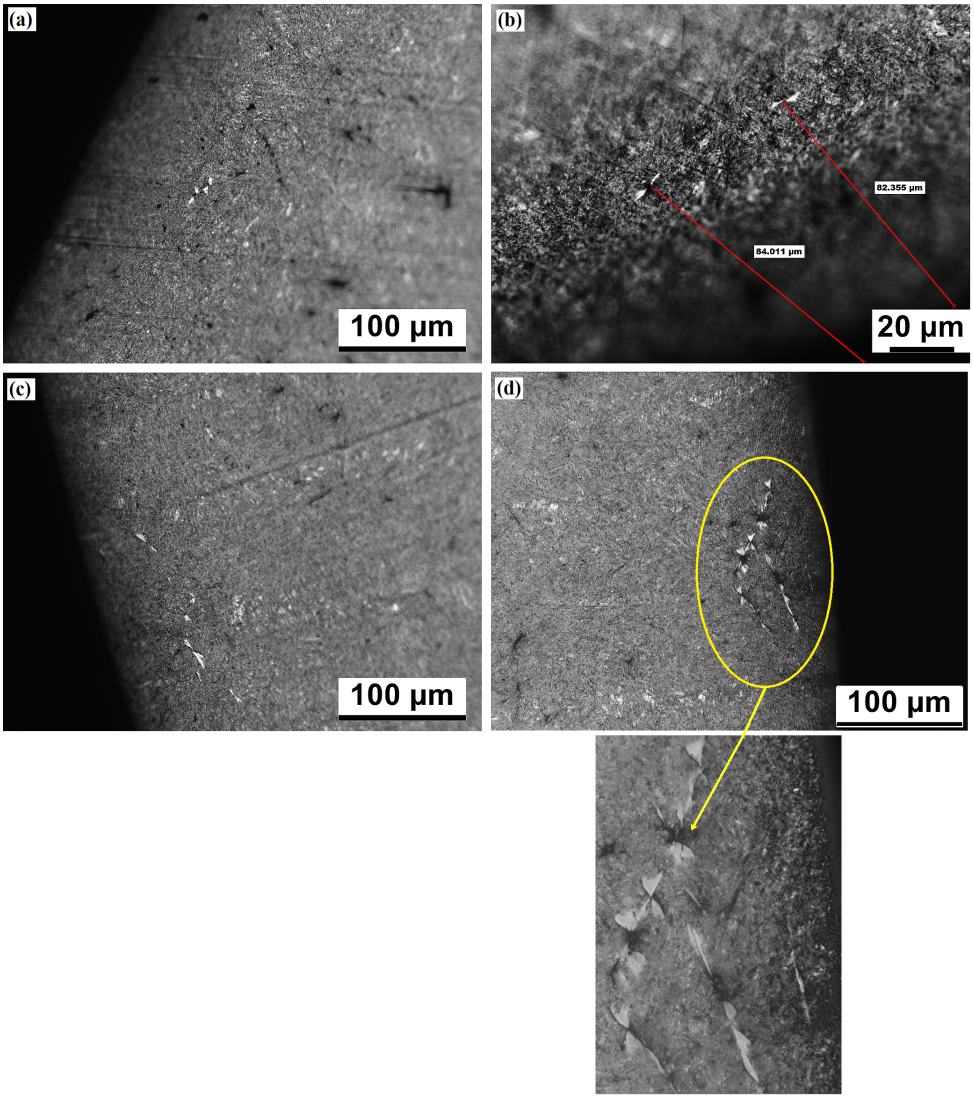

Figure 5.30: Early stage damage shown by a white-etching butterflies in 100Cr6+0.5V steel: a and b) hydrogen-free, c and d) hydrogen-charged.

SEM/EDX analysis was carried out to identify the NMIs present in the alloy. Most of the inclusions were MnS (A-type), Al_2O_3 and SiO_2 (D-type). Detailed images showing some of the NMIs that were found in the studied 100Cr6+0.5V steel are presented in Figure 5.31. Al_2O_3 inclusions were fine in size ($\sim$ 3 μm), while all other inclusions were large ($>$ 60 μm). Having entered the lattice, hydrogen gathers around these inclusions and embrittles the steel over a period of time, and with the absence of effective traps such

as V_4C_3, microcracks initiate and propagate rapidly within the entire subsurface causing an early and sudden failure.

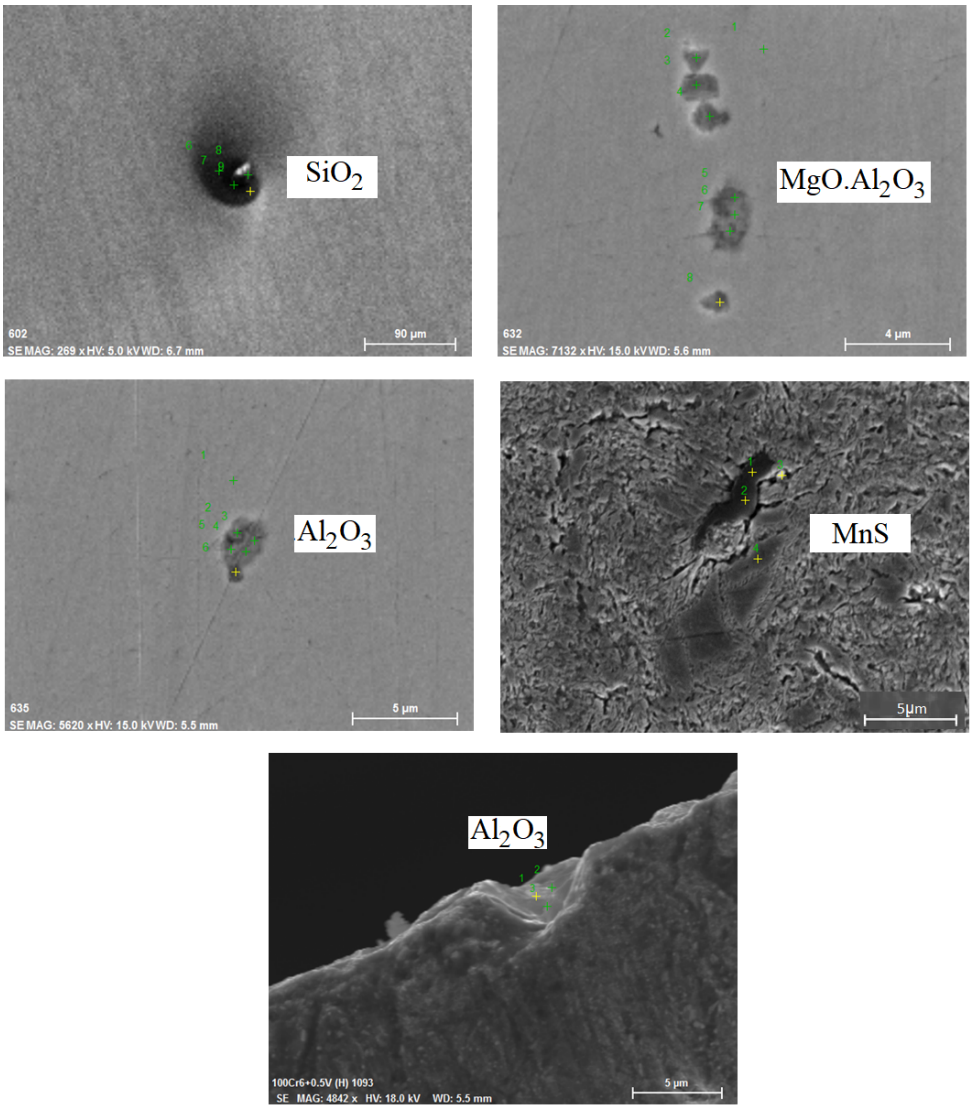

Figure 5.31: Non-metallic inclusions observed in 100Cr6+0.5V RCF specimens.

Finally, the results disclosed that damage -manifested by WEAs- under the raceway caused by stress concentrations around NMIs due to the alloy low cleanliness. The ability of vanadium-added bearing steel to trap hydrogen and enhance the bearing life was affected by the high oxygen content in the alloy. Moreover, large globular particles and stringers of NMIs which remain in the alloy after casting, in addition to coarse cementites formed during heat treatments, all act as stress raisers and can induce microcrack nucle-

ation during cyclic loading since they can be deformed or broken up forming voids around them [16] which is considered as preferred sites for hydrogen accumulation. Therefore, it is crucial to lower the non-metallic oxide inclusions in bearing steel and control their composition and size distribution in order to minimise the subsurface failure during rolling contact fatigue.

5.2 TRIP steel results and discussion

5.2.1 Influence of the heating rate on $\alpha + \mathrm{p} \rightarrow \alpha + \gamma$ transformation

A typical micrograph of the initial microstructure for 0.5C-1.25Mn-1.45Si-0.75Al TRIP alloy is shown in Figure 5.32. The microstructure is composed of nearly 36 % ferrite and 64 % pearlite. It was found that the heating rate has a significant influence on ferrite + pearlite to austenite transformation, and subsequently on the final microstructure. In Figure 5.33a where the specimen was heated with low heating rate (HR) of 3.0 °C s^{-1}, pearlite was completely decomposed, and the final microstructure consists of ferrite, retained austenite, and bainite. However, raising the heating rate from 3.0 to 10.0 °C s^{-1} caused an incomplete decomposition of pearlite which remained in the final microstructure in the form of separated colonies, Figure 5.33b.

To experimentally validate this rationale, Ac_1 and Ac_3 were determined by means of dilatometery, Figure 5.34, where Ac_1 and Ac_3 temperatures represent respectively the start and end temperatures of austenite formation under equilibrium conditions.

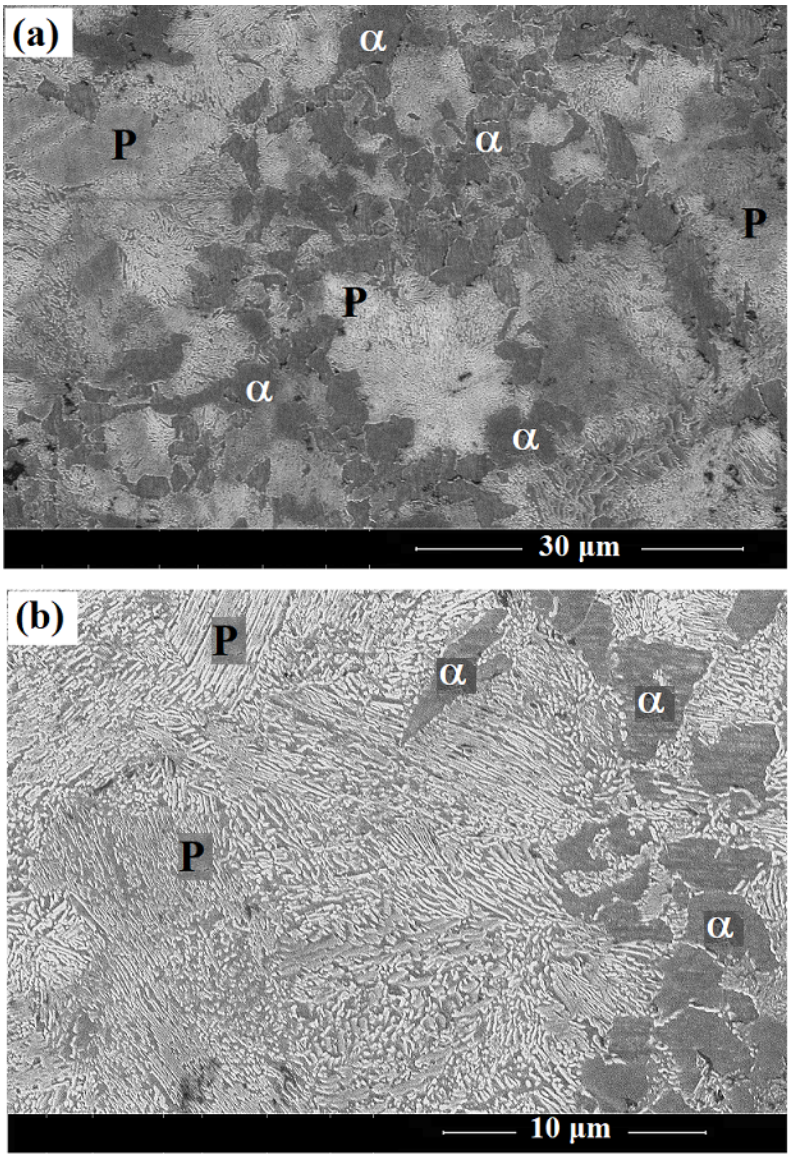

Figure 5.32: Initial microstructure for the studied TRIP steel in two magnifications: a) 30 μm and b) 10 μm (α: ferrite and P: pearlite).

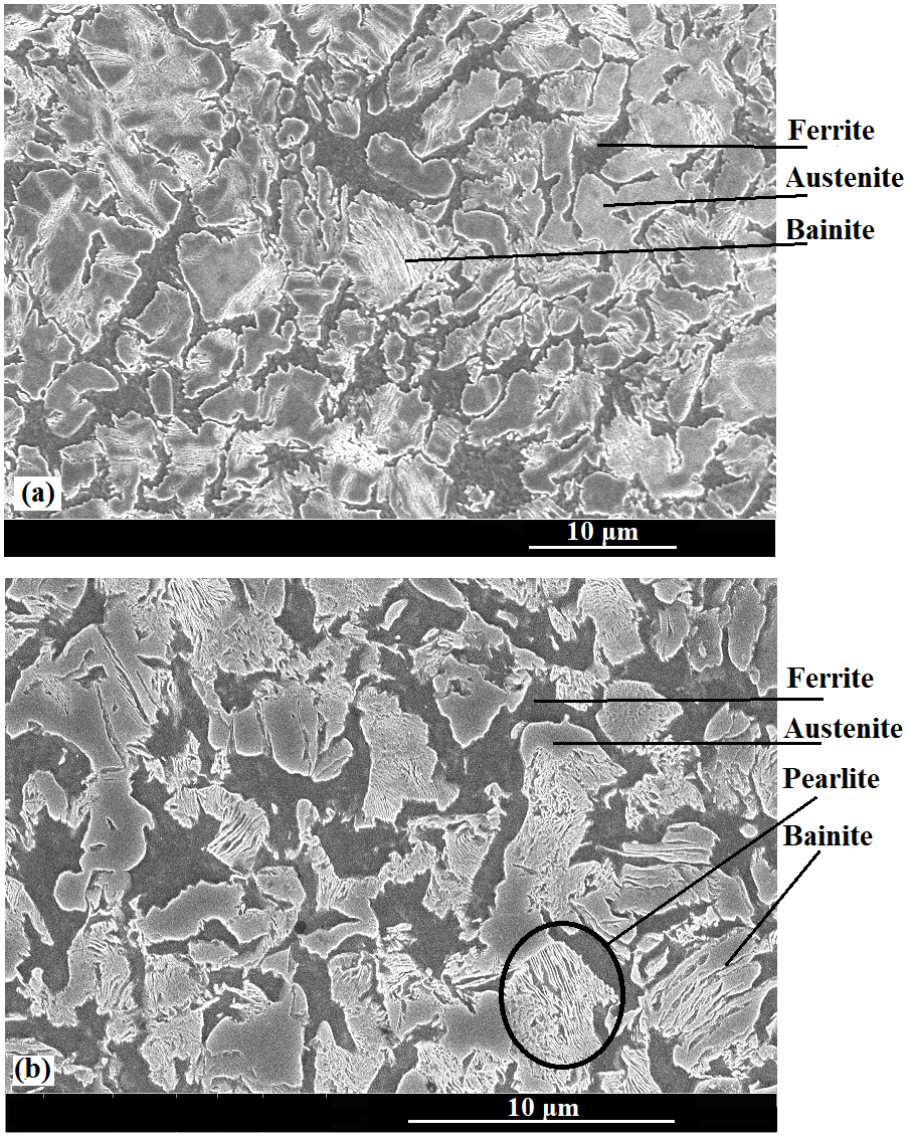

Figure 5.33: SEM images showing morphologies of the studied TRIP steel after identical two-stages heat treatments: a) HR = 3.0 °C s^{-1} and b) HR = 10.0 °C s^{-1}. Incomplete decomposed pearlite was found with higher heating rate [magnification 10μm].

Clearly, higher heating rate (10.0 °C s^{-1}) led to a decrease in both Ac_1 and Ac_3 to 754 °C and 790 °C.

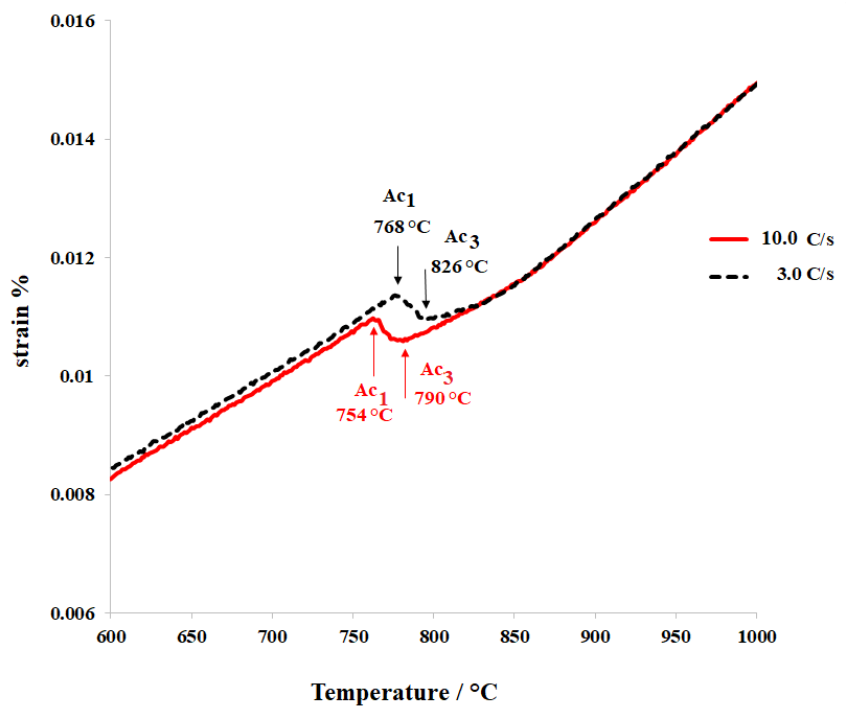

Figure 5.34: Influence of heating rate on Ac_1 and Ac_3 temperatures.

By calculating the equilibrium phases using Thermo-Calc ® with TCFE8 v8.0, it was found that cementite transformation ends at about 753 °C, Figure 5.35, therefore, at a higher heating rate the diffusion of carbon from when the cementite start to transform to austenite at 754 °C, Figure 5.34, is limited due to the short time of transformation, therefore pearlite colonies remain in the final TRIP microstructure.

Caballero *et al.* [232] demonstrated that in eutectoid carbon steel, both start and finish temperatures of the pearlite to austenite transformation starts later and appears to be slower the higher the heating rate is. Carbon diffusion rate through pearlitic cementite lamellae dominates austenite growth rate [232, 233]. Austenite first starts to nucleate inside pearlite at points where cementite meets with the edges of the pearlite colony, Figure 5.36 [234].

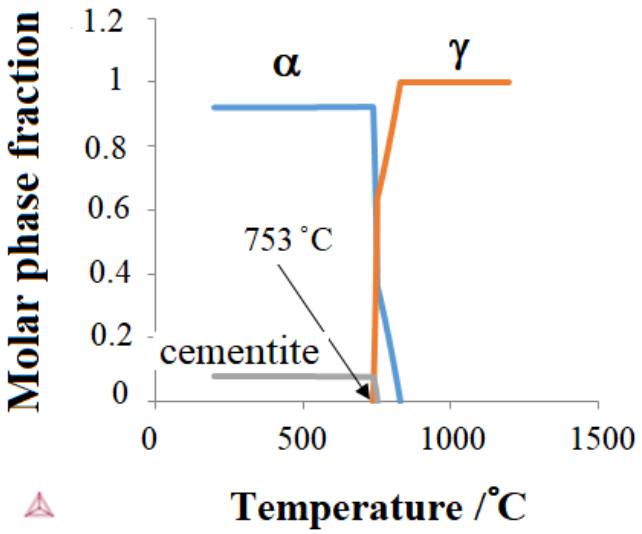

Figure 5.35: Cementite equilibrium diagram.

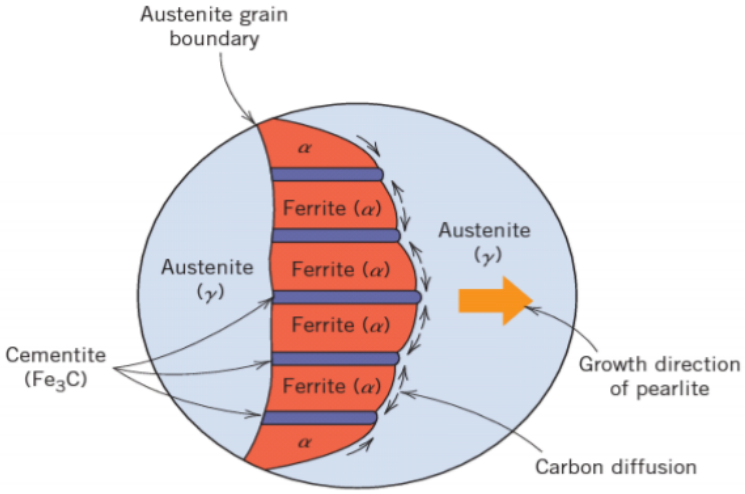

Figure 5.36: Formation and growth of pearlite [234].

This nucleation mechanism starts once the cementite rich regions disappeared (once the pearlite dissolution is completed). Austenite nuclei then grow into ferrite through redistribution of carbon between the former and the latter, simultaneously, resulting in a transformation of ferrite to austenite [235, 236]. According to that, lower heating rate (3.0 °C s^{-1}) raises Ac_1 to 768 °C giving a reasonable time for pearlite to decompose before austenite transformation starts.

Quantitative analyses of phases in the microstructure after applying intercritical annealing (IA) with optimised HR= 3.0 °C s^{-1} revealed that 65 % austenite was in the ferrite matrix, Figure 5.37. Therefore, the experiment result match the calculations data very well since the phase fraction obtained experimentally is close to the calculated value (62 %) shown in Figure 3.6.

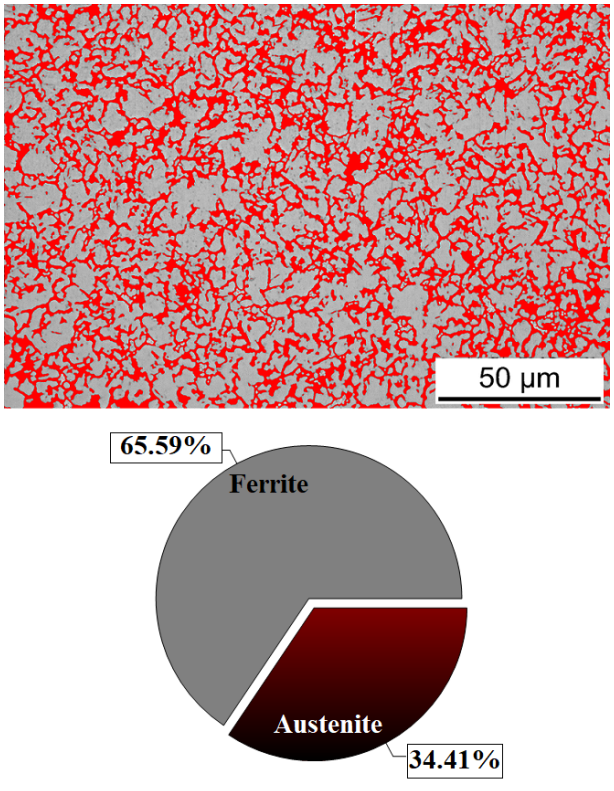

Figure 5.37: Quantitative analyses of phases in the microstructure after applying IA.

5.2.2 Bainite isothermal transformation stage

In this study, it is of great importance to identify the type and volume fraction of retained austenite as well as the carbon content in it. Retained austenite is an untransformed form of austenite that remains after quenching from austenitisation to room temperature [237, 238]. These different types of retained austenite contribute to the mechanical properties differently. Blocky retained austenite provides high work hardening and strengthening, while film-like retained austenite enhances the mechanical properties by increasing the transformation-induced strain hardening phenomena to larger strains [239, 240]. Therefore, controlling the phase constitution was performed by a rapid quench from IA temperature to 302 °C (to avoid pearlite formation) at which bainitic isothermal transformation takes place.

Three cases of BIT were chosen to calculate the fraction of retained austenite in the final microstructure: 24, 30 and 60 minutes (the reason will be discussed later). The fractions were first obtained experientially using X-ray phase analysis in Figure 5.38 based on the Rietveld method, then the results were confirmed using Miller equation, eq. 5.2 [241]:

$$Vf_\gamma = \frac{1.4 \cdot [I_\gamma^{220}]}{I_\alpha^{221} + 1.4 \cdot [I_\gamma^{220}]} \tag{5.2}$$

where I_γ^{220} is the integrated intensity obtained from the $(220)_\gamma$ diffraction peak of retained austenite, and I_α^{221} is the integrated intensity from the $(221)_\alpha$ diffraction peak of ferrite.

Also, the fraction of retained austenite is noticeably connected to the austenite lattice constant, which in turn is dependent on the carbon concentration in γ phase. The value of

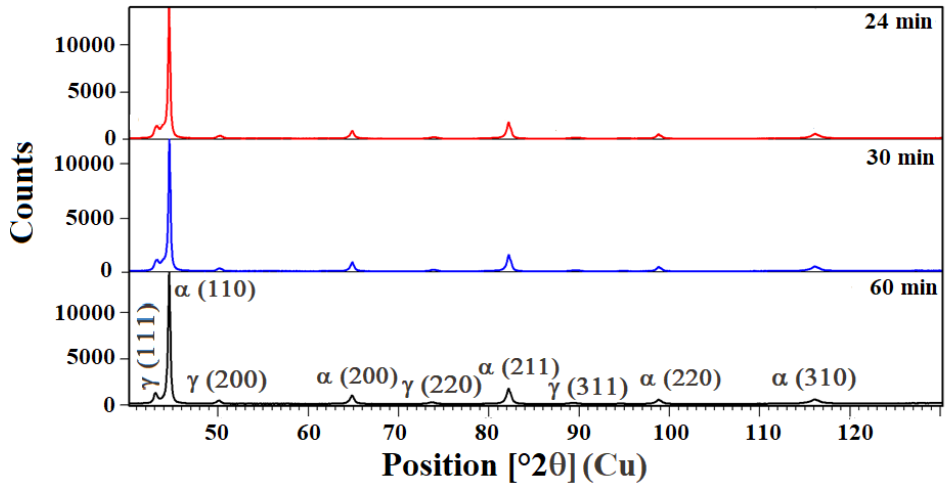

Figure 5.38: XRD patterns of the TRIP steel after full heat treatment with different BIT holding times. Diffraction peaks of the austenitic phase (γ), the ferrite phase (α).

lattice constant varies in a quite small range, from 3.62 to 3.64 Å. The fraction of retained austenite in the range of the bainite isothermal transformation (BIT) holding time from 24 to 60 minutes is associated with a carbon content enrichment in austenite. Carbon concentration ($C_\gamma, wt.\%$) in retained austenite was estimated from 1.37 to 1.74 wt.%, respectively, from the lattice parameter by XRD using CuKα radiation. The average lattice parameter ($a_\gamma \times 10^{-10}$m) which was measured from the austenite diffraction peak was converted into carbon content by using the relationship, eq .5.3 [242]:

$$a_\gamma = 3.578 + 0.033(C_\gamma, wt.\%) \tag{5.3}$$

Furthermore, austenite thermodynamic stability is described by the start temperature of the martensitic transformation (M_s), expressed most often by the following equation, eq. 5.4 [243] where all the concentrations are given in weight fraction:

$$Ms(°C) = 545 - 33000 \times C_c + 200 \times C_{Al} + 700 \times C_{Co} - 1400 \times C_{Cr} - 1300 \times C_{Cu} - 2300 \times C_{Mn}$$
$$- 500 \times C_{Mo} - 400 \times C_{Nb} - 1300 \times C_{Ni} - 700 \times C_{Si} + 300 \times C_{Ti} + 400 \times C_V \quad (5.4)$$

From X-ray diffraction analysis of retained austenite fractions it was noticed that the first two scenarios, 3 and 6 minutes, did not meet the criteria presented in Table 3.3 of the studied steel due to exceedingly high retained austenite which remained untransformed: 57.6 % and 51.9 %, and high M_s temperatures: 241.1 °C and 238.1 °C, respectively. Furthermore, stability of austenite against transformation to martensite increases at higher M_s [244]. Gruber *et al.* [245] deduced that the M_s temperature occurs at lower temperatures the longer the tempering times are. Table 5.7 presents the hardness, fractions of retained austenite together with the carbon concentration in austenite, and martensite starting temperature. According to these findings, the sixth scenario which includes holding for 180 minutes was also excluded because of the strong reduction in M_s temperature to -75.4 °C.

Table 5.7: Comparison between hardness, retained austenite fraction, carbon content and M_s for six scenarios of BIT holding times.

Bainitic isothermal holding time (minutes)	**3**	**6**	**24**	**30**	**60**	**180**
Hardness (HV30)	416	418	349	347	336	347
Retained austenite (vol.%)	57.6	51.9	48.4	36.7	34.1	18.9
Carbon in austenite (wt.%)	0.92	0.93	1.37	1.39	1.74	1.88
M_s (°C)	241.1	238.1	92.9	86.3	-29.2	-75.4

Therefore, three results among six were selected for analysis and comparison: 24, 30 and 60 minutes hold at BIT, Figure 5.39. Table 5.8 summarises the fractions of retained

austenite together with the lattice constant, carbon concentration in austenite as well as the martensite start temperature, and bainite subunit size. 10 TEM images for each case were used to measure the average subunit size using software ImageJ.

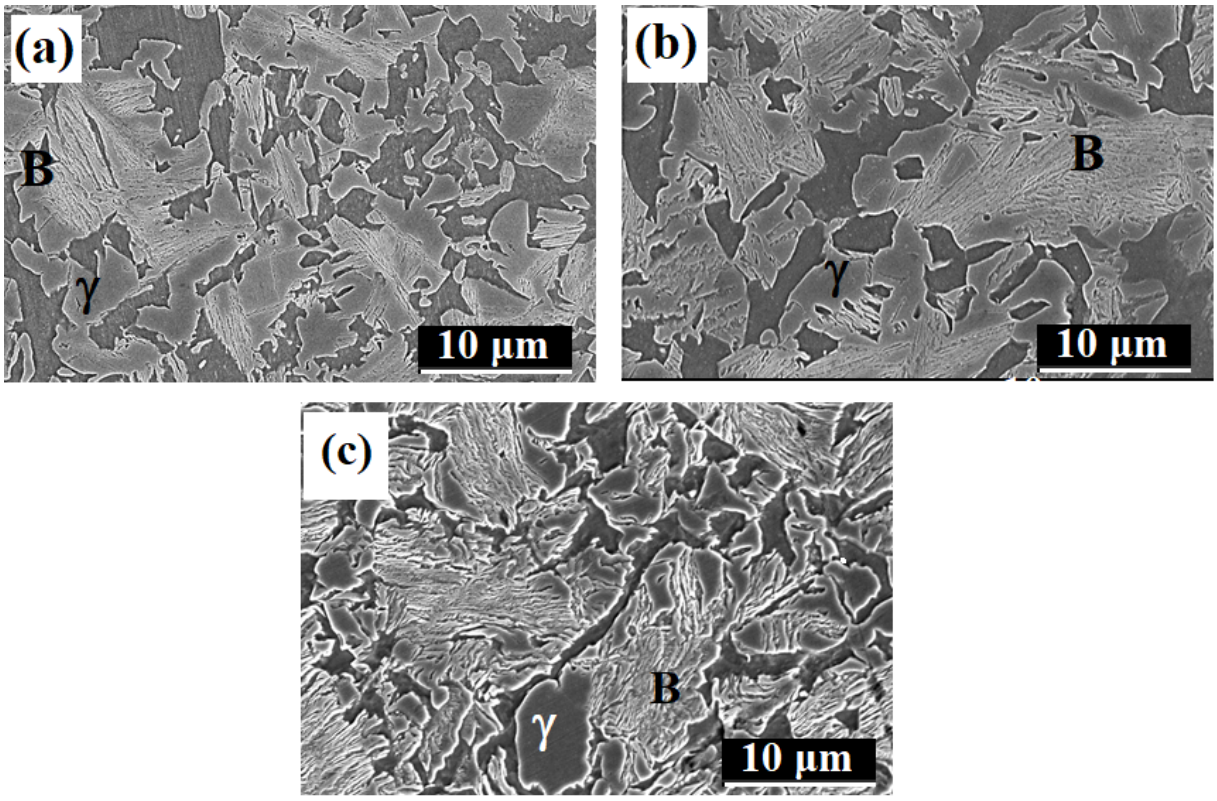

Figure 5.39: Retained austenite to bainite transformation as a result of increasing BIT holding time: a) 24 min, b) 30 min, and c) 60 min (B: bainite and γ: austenite).

It appears from Figure 5.38 and Table 5.8 that the fraction of retained austenite decreases along with increasing the holding time at the isothermal bainitic transformation stage, reaching 34.1 % by holding for 60 minutes at 302 °C. The transformation is accompanied by a drop in the hardness from 349 to 336 HV30, Table 5.7, as a result of increasing the bainitic subunit sizes. Blocky retained austenite was observed in the microstructure distributed throughout the bainite matrix.

Table 5.8: Summary of XRD analysis of the studied TRIP steel.

Bainite isothermal holding time (minutes)	24	30	60
Total volume fraction of retained austenite (vol.%)	48.4	36.7	34.1
Blocky retained austenite (vol.%)	22	22	12.8
Blocky retained austenite grain size (μm)	2.5	2.5	1.4
Lattice parameter of austenite (Å)	3.623224 ± 0.000210	3.623899 ± 0.000143	3.635575 ± 0.000162
Total carbon content in austenite (wt.%)	1.37	1.39	1.74
M_s (°C)	92.9	86.3	- 29.2
Subunit size (nm)	78	114	118

Its volume fraction was estimated using systematic manual point count according to ASTM E562 - 11 standard [246]. An average of 10 SEM images with a magnification of 10 μm were used to determine the volume fraction of blocky retained austenite. This type was found to form a relatively high portion of the total retained austenite. Its size varies between 2.7 μm for both 24 and 30 minutes holding scenarios, and 1.3 μm for the 60 minutes scenario, and with the amount of carbon content found in the total retained austenite, it is expected that blocky retained austenite contributes to good mechanical properties.

The M_s temperature was found to be higher than room temperature for the lower carbon contents, and this also explains the high hardness numbers produced by holding for 24 minutes compared to 60 minutes at BIT. Here we came to the conclusion that the most promising microstructure with respect to the expected strength of 1303 MPa is obtained after tempering in BIT stage between 24 to 30 minutes with an average hardness of 349 HV30.

TEM micrographs, Figure 5.40, show a microstructure consisting of nanoscale plates of bainitic ferrite, separated by carbon-enriched retained austenite obtained at 302 °C for 24, 30 and 60 minutes. A typical feature of the lower bainite structure is cementite precipitating on the ferrite/austenite interface, Figure 5.40a, which forms during holding at the transformation stage depending on the temperature [131]. However, the high silicon concentration in the alloy retards this reaction [247–249], which explains the absence of cementite in the specimens that were subjected to longer bainitic isothermal holding times, Figure 5.40b and c.

It is remarkable that bainite continues to grow with extended heating at BIT by continuous nucleation of sub-units in which carbon is re-distributed from supersaturated

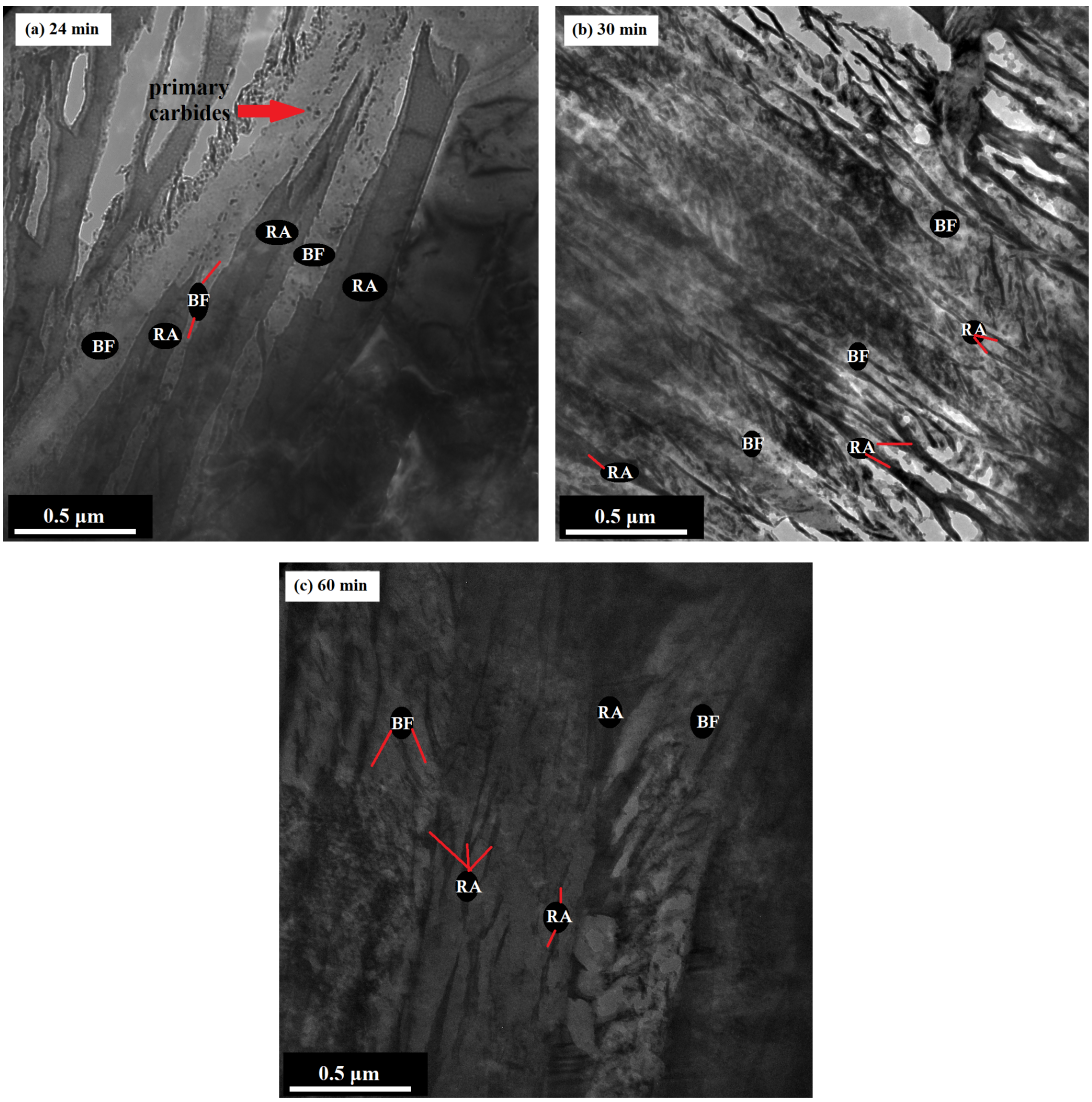

Figure 5.40: TEM micrographs of TRIP steel (a) BIT for 24 min, (b) BIT for 30 min, and (c) BIT for 60 min. (BF: bainitic ferrite, and, RA: retained austenite).

bainitic ferrite to the surrounding retained austenite [250, 251]. In the recent experiments, the bainitic sub-unit grew almost 45 %, from 78 to 114 nm when BIT heating time increased from 24 to 30 minutes, Table 5.8.

Carbon concentration in retained austenite increases and the bainite free energy becomes less than that of austenite of the same composition [252–254], and the transformation ends [255], which is obvious from the sub-unit size that grew from 114 to only

118 nm when the BIT hold extended from 30 to 60 minutes in comparison to 45 % of growth between 24 and 30 minutes, Figure 5.41. An empirical relationship $L_T = \pi t/2$ was used to calculate the sub-units thicknesses (t) from TEM images, because it is rare for the entire bainite plate to be imaged. L_T is the mean lineal intercept in a direction normal to the plate length [256].

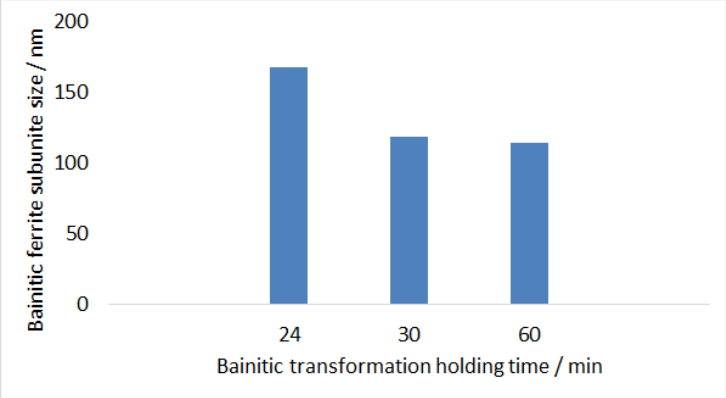

Figure 5.41: Bainitic ferrite sub-unite size associated with BIT holding time.

TEM micrograph in Figure 5.42 is taken from a specimen subjected to a 24 minutes holding at BIT stage, it clearly shows dislocations surrounding the blocky retained austenite. The distribution of dislocations near austenite/bainitic ferrite helps to accommodate the transformation strain during bainitic growth progresses that takes place by the expansion of the growing bainitic ferrite plate [257]. Dislocations also participate in increasing the elongation ability of TRIP steels. When transforming into martensite, the austenite grains cause a volume expansion that plastically deforms the surrounding bainitic ferrite, which generates dislocations in the contiguous ferrite as a consequence [258].

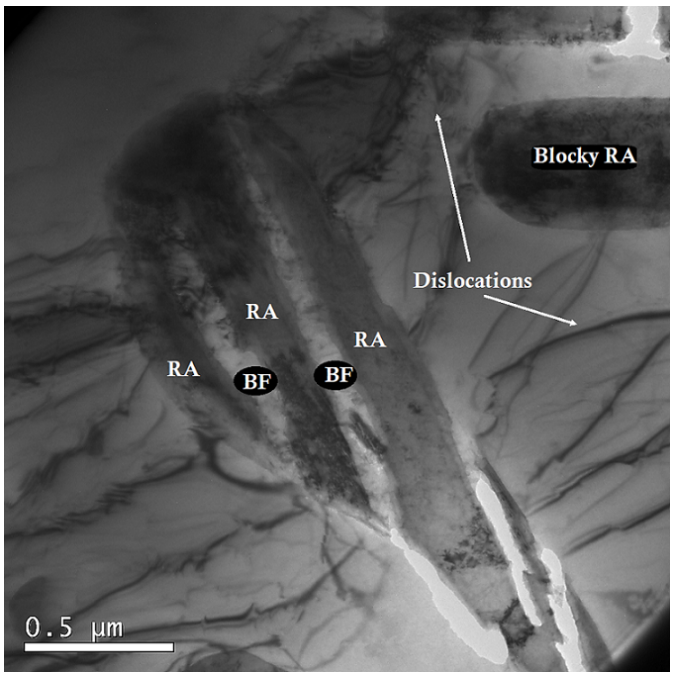

Figure 5.42: TEM image reveals dislocation surrounding retained austenite (BF: bainitic ferrite, and, RA: retained austenite).

5.2.3 Hydrogen induced cracking under stress in TRIP steel

The impact of hydrogen on the mechanical properties of TRIP steels was examined by performing hydro-hardness test on two specimens, 24 and 60 minutes holding at BIT. Both hydrogen charged specimens surfaces in Figure 5.43c and d showed cracks initiating indicating the embrittlement caused by hydrogen.

More brittle behaviour was observed on the hydrogen charged specimen that was subjected to a bainitic transformation at 302 °C for 24 minutes with a crack length about 243 μm (Figure 5.43c), comparing to 167 μm for the 60 minutes bainitic transformation specimen (Figure 5.43d). Indeed, the formation of cracks is induced by the presence of hydrogen, since they were not observed on the hydrogen-free specimen tested under similar conditions, Figure 5.43a and b. As stated in Table 5.7, prolonged bainitic annealing leads

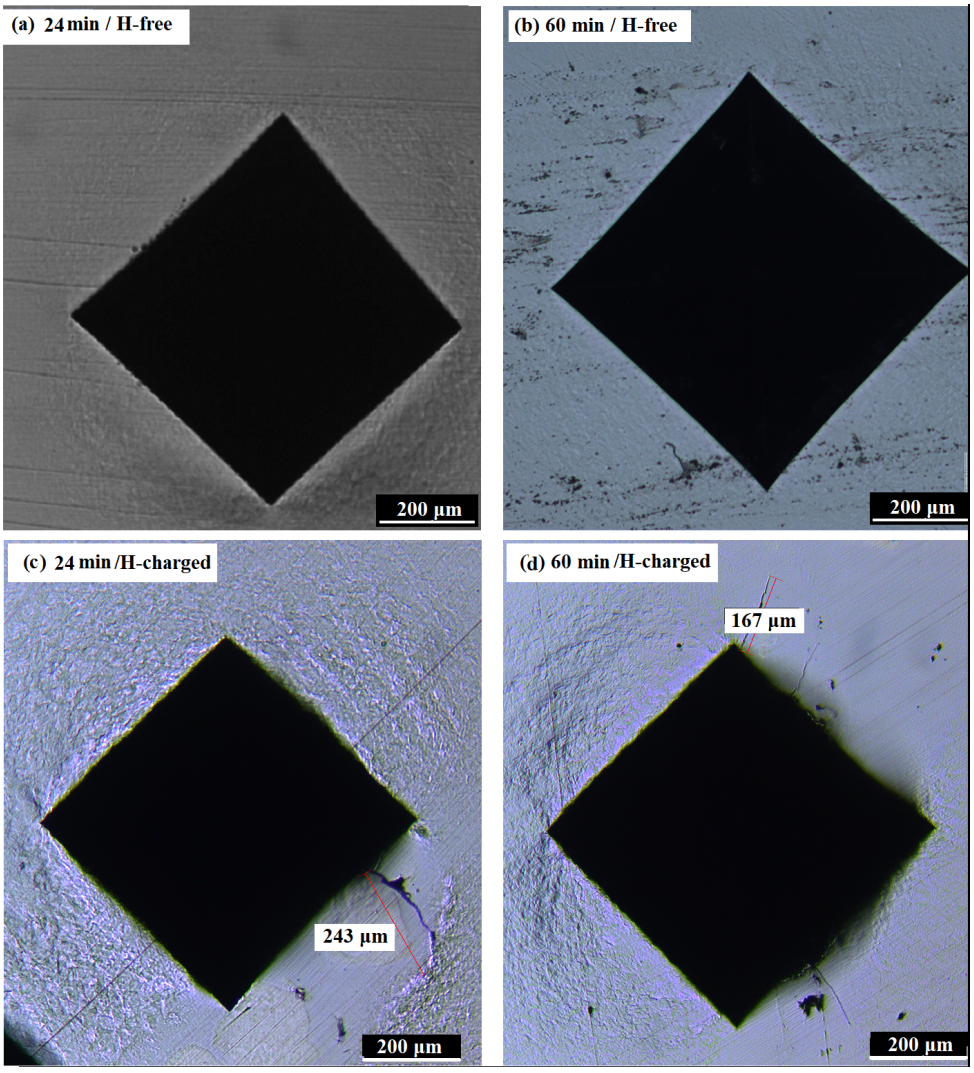

Figure 5.43: The effect of hydrogen on crack initiation in TRIP steel. H-free: a) BIT for 24 minutes, b) BIT for 60 minutes. H-charged: c) BIT for 24 minutes, d) BIT for 60 minutes.

to more austenitic transformation, and since retained austenite is an irreversible hydrogen trapping site, it acts as a source of hydrogen in the material. As a result, the specimen that was bainitic annealed for 24 minutes, contains a higher fraction of retained austenite, and therefore a higher quantity of trapped hydrogen. According to HEDE mechanism, accumulated hydrogen weakens the cohesive bonds between metal atoms, and with increasing pressure of hydrogen due to their large amount, brittle cracks propagate. Considering this, the specimen with lower retained austenite fraction propagated less and the crack is

smaller. Based on this result, it is questionable whether the presence of retained austenite with great volume fractions is beneficial to immobilise diffusible hydrogen within the material, or it should be considered as a detrimental source of hydrogen and increases the TRIP steel susceptibility to hydrogen embrittlement.

5.2.4 Determination of de-trapping activation energy for hydrogen traps

Before measuring the de-trapping activation energy, it was necessary to test the effect of holding time on the amount of trapped hydrogen. For this, a specimen from each case: BIT at 302 °C for 24, 30 and 60 minutes were hydrogen charged to saturation, then the trapped hydrogen in each specimen was measured using TDA. During heating, hydrogen at different traps released and the amount of hydrogen is recorded with the temperature [259]. The specimens trapped 5.5, 3.2 and 2.4 ppm, respectively, Figure 5.44. Trapped hydrogen decreased from 5.5 to 3.2 ppm as bainitic holding time increased just from 24 to 30 minutes. However, extending holding time from 30 to 60 minutes accompanied by a slight decrease in the amount of trapped hydrogen, from 3.2 to 2.4 ppm. The experiment was repeated under identical conditions and the results were similar, trapped hydrogen decreases with prolonged holding at bainitic stage. Predominantly, this trend is accompanied by the reduction of retained austenite fraction during bainite transformation. This trend could also be explained based on retained austenite size. Considering that diffusible hydrogen occupies the strongest traps with higher binding energy first before moving to fill up the weaker traps [220], it can be safely assumed that a large portion of hydrogen is trapped by retained austenite, this implies that hydrogen mass becomes lower with decreasing austenite volume fraction, Table 5.9. Several studies reported that

finer austenite grain size reduced the hydrogen embrittlement susceptibility [260–262]. Grain size often plays an important role in enhancing the mechanical properties of steels, and this was proved in section 5.2.3 when the specimen with smaller austenite grain size exhibited a shorter crack comparing to the longer crack formed with larger grain size.

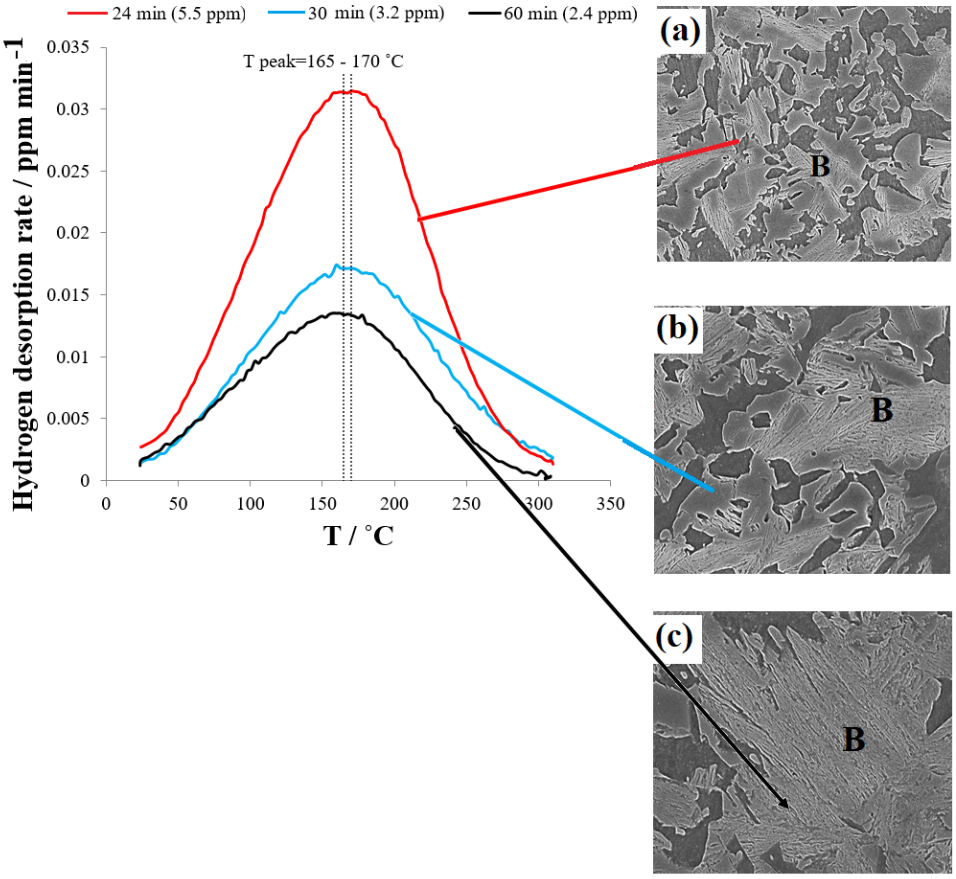

Figure 5.44: TDA profiles of trapped hydrogen taken from three specimens of TRIP steels: BIT at 302 °C for: a) 24, b) 30 and c) 60 min. SEM magnification 10 μm.

Finally, the de-trapping activation energy were calculated to verify the major type of traps in this steel. From Figure 5.44, it is clear that the hydrogen evolution curves are virtually identical with peak temperatures range between 165 to 170 °C for all cases, thus, it was speculated that hydrogen was trapped at the same type of trapping site as will be further elaborated below. According to this view, BIT at 302 °C for 30 minutes was chosen to measure the de-trapping activation energy considering that it is an intermediate case

Table 5.9: Comparison between the amount of trapped hydrogen with respect to retained austenite size in the studied TRIP steel.

Bainite isothermal holding time (minutes)	24	30	60
Total retained austenite fraction (vol.%)	48.4	36.7	34.1
Blocky retained austenite (vol.%)	31.5	25.9	19.8
Blocky retained austenite grain size (μm)	2.7	2.7	1.3
Trapped hydrogen (ppm)	5.5	3.2	2.4

between 24 and 60 minutes holding cases, in addition that the three specimens showed comparable peak temperatures.

Hydrogen escapes from the trap when its de-trapping activation energy is reached, and the higher the activation energy is, the stronger is the trap [259]. Accordingly, the correlation between hydrogen traps types in the material and bainitic holding time was discussed. Numerous reports showed that during bainitic holding stage, austenite transforms to bainite [119, 128, 133, 263, 264]. However, austenite retained within bainite and its fraction depends on temperature and, indeed, on the holding time, which dominates the amount of trapped hydrogen.

The de-trapping activation energy was calculated using the peak shift method as hydrogen desorption peak temperatures shift as a consequence of varying heating rate, Figure 5.45a. By using equation 5.1, the de-trapping activation energy is 45.6 kJ mol^{-1} which means that hydrogen in trapped in retained austenite [265]. It is noteworthy to mention that the transformation of retained austenite to martensite during plastic deformation of TRIP steels releases the hydrogen that is trapped in austenite, causing the strong irreversible trap to act as a reversible trap. Furthermore, hydrogen trapping capac-

ity of retained austenite is linearly proportional to its volume fraction [266] which could also explain the reason why the lower retained austenite fraction specimen exhibited more embrittlement resistance in the hydro-hardness test.

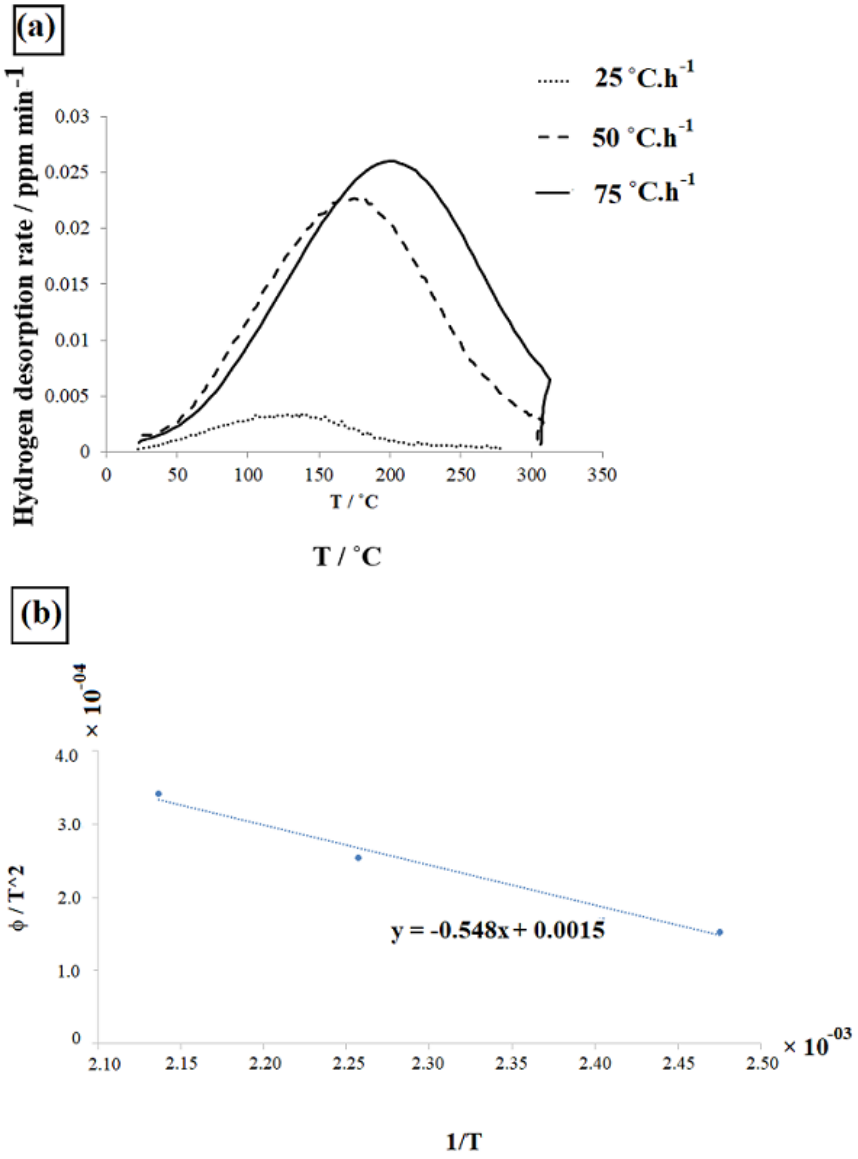

Figure 5.45: a) Change in hydrogen evolution curve with heating rate, b) determination of activation energy of de-trapping for studied TRIP steel (peak shift method [267]), BIT at 302 °C for 30 min.)

5.3 Summary

In the first part of this chapter, the role of vanadium in enhancing the mechanical properties of 100Cr6 bearing steel was discussed in detail. The remodeled heat treatment for 100Cr6+0.5V was applied and the treated steel was characterised and compared with properties resulting from the original heat schedule. The new alloy 100Cr6+0.3V was cast and an intensive investigation was performed. The results showed an adequate hardness and hydrogen trapping capacity. The de-trapping activation energies for 100Cr6 and 100Cr6+0.5V were calculated using TDA. These results indicated that the main trapping sites are dislocations and V_4C_3, respectively. In terms of mechanical properties testing, and although a level of ductility loss was observed in hydrogen charged vanadium bearing steels, there is a direct evidence that V_4C_3 precipitations significantly enhances the hydrogen trapping comparing to vanadium-free steel. The behaviour of hydrogen in 100Cr6+0.5V and 100Cr6+0.3V steels has been investigated by means of hydro-hardness technique. The length of the radial cracks produced by Vickers indentation is dependent on the vanadium content in the steel, thus on the amount of trapped hydrogen within the lattice. Tensile tests were performed on both hydrogen free and charged notched specimens. Hydrogen charged specimens displayed a rather fast and significant ductility drop during immediate tensile testing compared with hydrogen-free specimens. Fractography confirmed the correlation between the presence of NMIs and early failure as a result of hydrogen induced microcracks. The same trend was found in RCF tests. Despite its early failure, 100Cr6+0.5V showed an increase in bearing life in the presence of hydrogen comparing to 100Cr6 which is a satisfactory proof that hydrogen embrittlement is not the main reason of the failure. This assumption was proved by SEM/EDX which confirmed vast majority of the microcracks that occurred under RCF test associated with NMIs.

In the second part, the heat treatment of Fe-C-Mn-Si-Al TRIP steel was optimised. The most promising microstructure with respect to the UTS (1303 MPa) was obtained after tempering in BIT stage for 24 min with a hardness of 349 HV30. Microstructural evolution by TEM after applying the optimised heat treatment showed lower bainite structure consisting of ferrite plates and films of retained austenite. The impact of hydrogen on the mechanical properties of this steel was examined by performing hydro-hardness testing. More brittle behaviour was observed on the hydrogen charged specimens that were subjected to a bainitic transformation at 302 °C for 24 minutes compared to 60 minutes transformation. It is suggested this is a result of the high content of trapped hydrogen in retained austenite as a 24 minutes bainitic holding resulted in a higher volume fraction of untransformed retained austenite that acts as a source of hydrogen in the material. Finally, the de-trapping activation energy was calculated to verify the major type of traps in this steel. The main trapping site was found to be consistent with retained austenite.

Chapter 6

General conclusions and suggestions for future work

In this work, the effect of hydrogen embrittlement (HE) on the mechanical properties of advanced high strength steels was studied. Four grades with medium and high carbon steels were investigated. High carbon bearing steel used to provide a direct evidence of the benefits of nanosized V_4C_3 with respect to advanced high strength steels life given the substantial levels of hydrogen ingress that is observed in many operational conditions of such steels. Vanadium-added bearing steels were investigated along with a medium carbon TRIP steel. The aim of studying hydrogen embrittlement in the TRIP steels is to provide an insight into delayed cracking in bearing steels owing to retained austenite transformation. Overall, the findings of this study can be understood as:

6.1 Microstructural and hydrogen trapping comparison

- For 100Cr6+0.5V high carbon bearing steel that was treated with the original heat treatment (HT), the microstructure was originally investigated with TEM in a previous study. Here, the formation of nanosize V_4C_3 was confirmed using atom probe tomography. The carbides average volume fraction was ~ 0.0081 with a 5 nm radius, which is in a good agreement with the earlier study findings.

  However, a new heat treatment was suggested for 100Cr6+0.5V in order to reduce energy consumption. TEM observations showed the formation of V_4C_3 particles range between 5 to 10 nm radius embedded in a tempered martensite microstructure. The V_4C_3 volume fraction was found to be lower than what was found in the specimens that were treated according to the original HT, but despite that, the steel preserved its unique properties of high hardness and hydrogen trapping properties.

  Moreover, a new bearing steel 100Cr6+0.3V was proposed and examined. TEM/EDX confirmed the formation of V_4C_3 nano-particles sized 5 - 10 nm unlike the modelling results which suggested a 4 nm carbide radius at the end of the heat treatment. This variation between the experimental and the modelling results indicates that carbides coarsening is in fact much faster than what is predicted by modelling. However, the variation did not effect the mechanical properties or the hydrogen trapping efficiency of the steel.

- For medium carbon TRIP steel, thermodynamic calculations were used for phase fractions prediction during the intercritical annealing (IA) stage of the designed steel. It was estimated that after holding at 771 °C for 900 seconds, 86 % of the transformation is completed and the structure should contain about 62 % of retained

austenite (RA). The final microstructure showed lower bainite structure consisting of ferrite plates, film-like and blocky retained austenite. Quantitative analysis of phases reveled that the 65 % of austenite retained in the ferrite matrix, which is in good agreement with the calculations. Bainite sub-unit size and the proportion of final phases depend on the bainitic isothermal holding time and temperature. Increasing the bainitic transformation holding time resulted in a change of the bainite morphology as it allows more growth for bainite, hence lowering its hardness. This is because the larger plates have lower carbon concentration and thus lower hardness. Therefore, the most promising microstructure with respect to the expected UTC (1303 MPa) is obtained after in bainite isothermal tempering at 302 °C for 24 to 30 minutes.

- The role of RA is of great importance on the hydrogen embrittlement of high strength steels, therefore, three grades of 100Cr6+V bearing and TRIP steels were both studied in this research despite the microstructural differences between the studied steels. X-ray analysis for 100Cr6+V bearing steels showed around 13 - 15.5 % of austenite retained after heat treatment in the final microstructure. This volume fraction of RA is desired because of its beneficial effects on improving rolling contact fatigue performance. On the other hand, TRIP steel revealed higher RA content which varies depending on the heat treatment used. Bainitic isothermal holding for 24, 30 and 60 minutes resulted in 48.4, 36.7 and 34.1 % of RA with carbon content 1.37, 1.39 and 1.74 wt.%, respectively. The presence of stable RA in the microstructure enhances the total elongation by TRIP effect and inhibits its transformation into martensite under a small strain.

- In terms of hydrogen trapping, the amount of trapped hydrogen increased with increasing vanadium content, therefore the volume fraction of nano-size V_4C_3 carbides

in all grades of bearing steels. 100Cr6+0.5V trapped 4.4 ppm in comparison with 3 ppm trapped by the same steel when it was treated with the new designed HT. 100Cr6+0.3V trapped 1.7 ppm while 100Cr6 trapped 0.6 ppm only. This brings forth direct evidence that trapping capacity depends on the effective surface area of carbides and their volume fraction. The activation energies for hydrogen evolution from trapping sites were calculated for 100Cr6 and 100Cr6+0.5V steels. The main trapping sites in 100Cr6 are dislocations with a de-trapping activation energy of 32.3 kJ mol^{-1}, which explains the low trapping capacity in vanadium-free bearing steels as hydrogen tend to diffuse out easily from weak trapping sites such as dislocations. Nano-size V_4C_3 were confirmed to be the major trapping sites in 100Cr6+0.5V with a de-trapping activation energy of 35.2 kJ mol^{-1}. In contrast, more hydrogen was trapped in TRIP steel that contain higher RA content suggesting that RA acts as a source of hydrogen in the material. De-trapping activation energy measurements verified that the major type of traps in this steel is retained austenite.

6.2 Mechanical properties and hydrogen embrittlement

- Slow strain rate testing was conducted to estimate mechanical properties of vanadium-added 100Cr6 steel with and without hydrogen charging. Before hydrogen charging 100Cr6+0.5V showed remarkable results with an ultimate tensile strength (UTS) of 2577 MPa in comparison to 2352 MPa for 100Cr6. A noticeable drop was noticed after hydrogen charging in both steels. However, 100Cr6+0.5V fracture morphology showed few tiny brittle regions in the fracture crack propagation path isolated by widely spread ductile regions indicating that the specimen failed in a ductile manner which is triggered by coarse cementite in 100Cr6+0.5V, unlike 100Cr6 that failed

due to the presence of non-metallic inclusions (NMIs) in 100Cr6. The effect of steel cleanliness on HE was evident through rolling contact fatigue (RCF) tests. Numerous long and near-surface butterflies were found in both hydrogen-charged steels and most of the cracks were clearly associated with NMIs, which emphasizes that the cleanliness of the steel and raceway has a significant effect on bearing life. Additionally, RCF tests confirmed the correlation between bearing life and the addition of vanadium. 100Cr6 RCF rods showed a low HE resistance due to the high amount of weakly trapped hydrogen. In the contrary, HE degree was lower for 100Cr6+0.5V rods since hydrogen atoms were mostly trapped by V_4C_3. Further investigations were done through hydro-hardness tests that confirmed HE resistance follows different tendencies. While all vanadium-added steels trapped more hydrogen and were more resistant to HE than 100Cr6 with shorter cracks, 100Cr6+0.3V exhibited the best HE resistance after hydrogen charging as in 100Cr6+0.5V cracks were longer and the specimen kept cracking for one hour after charging was stopped. Most importantly, it was found that ductility loss is reversible as specimens, especially vanadium-added steels, recovered when they were left two weeks in room temperature. Thus, our findings suggest that the best HE resistance, as well as cost savings, can be obtained by decreasing the amount of vanadium in the 100Cr6 alloy.

- Finally, the impact of hydrogen on the mechanical properties of TRIP steel was more pronounced in specimens with higher amount of RA that acts as hydrogen traps and as a result become source for hydrogen in the material. Hydro-hardness tests confirmed that the plastic deformation aids RA transformation to brittle martensite, and when this process is combined with releasing hydrogen -due to the decomposition of austenite-, the materal becomes more prone to HE. Therefore, for better HE resistant-TRIP steels, it is suggested that RA should not exceed 0.36 % of the total

phases in TRIP steels.

6.3 Future work

Looking forward, further investigations are necessary to validate the new findings that can be drawn from this study, which can lead to the development of using vanadium in advanced high strength steels. Accordingly, future work is suggested as follows:

- To validate the beneficial effects of lowering the vanadium content on HE of bearing steels and its impact on their mechanical properties, tensile tests and RCF must be conducted on the new 100Cr6+0.3V steel, and the results should be then compared to what was found for 100Cr6+0.5V in this study. Furthermore, 100Cr6+0.5V steel cleanliness is one of the variables that needed to be improved. To alleviate NMIs in the steel, impurity controls throughout the steelmaking should be addressed in future studies. Much cleaner steels with lower inclusion content will help to increase the actual benefits of vanadium in enhancing the bearing life of 100Cr6 steel. Again, RCF tests should be performed on 100Cr6+0.5V specimens with higher cleanness rate then study the effect based on the results of this study.

- In terms of 0.5C-1.25Mn-1.45Si-0.75Al TRIP steel, it is suggested to use more advanced thermal desorption analysis equipment to detect hydrogen peaks at higher temperatures, which was not available for this work. It would also be interesting to study the possibility of adding vanadium to TRIP steels to form vanadium carbides traps, then examine the influence of V_4C_3 on the mechanical properties and compare the results with what has been achieved in the recent work.

- It is also recommended to utilise visualizing methods such as tritium autoradio-

graphy or hydrogen microprint technique to visualize the location of hydrogen in nano-scale site such as retained austenite and V_4C_3 especially in vanadium-added TRIP steel.

- Electric current pulse is a recently developed technique to instantly remove hydrogen from high strength steels [268]. When electric current is applied, the de-trapping activation energy is decreased and the hydrogen diffusion coefficient is increased, so the hydrogen removal is accelerated. Applying this method with adding vanadium to high strength steels will combine benefits of precipitations strengthen of the V_4C_3 and removing hydrogen out of the steel, thus avoiding hydrogen-induced damage caused by trapped hydrogen inside the material.

Bibliography

[1] Johnson, W.H. On some remarkable changes produced in iron and steel by the action of hydrogen and acids. Proceedings of the Royal Society of London. **vol.** 23, pp. 168-179. 1874.

[2] Frohmberg, R. P., Barnett, W. J., and Troiano, A. R. Delayed Failure and Hydrogen Embrittlement in Steels. *Transactions of American Society for Metals.* **vol.** 47, pp. 892. 1955.

[3] Hirth, J. P. Effects of hydrogen on the properties of iron and steel. *Metallurgical and Materials Transactions A.* **vol.** 11(6), pp. 861-890. 1980.

[4] Pressouyre, G. M. Hydrogen traps, repellers, and obstacles in steel; Consequences on hydrogen diffusion, solubility, and embrittlement. *Metallurgical and Materials Transactions A.* **vol.** 14(10), pp. 2189-2193. 1983.

[5] Nagumo, M., Nakamura, M., and Takai, K. Hydrogen Thermal Desorption Relevant to Delayed-Fracture Susceptibility of High-Strength Steels. *Metallurgical and Materials Transactions A.* **vol.** 32(2), pp. 339-347. 2001.

[6] Ichitani, K., Kanno, M., and Kuramoto, S. Review: Recent Development in Hydrogen Microprint Technique and Its Application to Hydrogen Embrittlement. *ISIJ International.* **vol.** 43(4), pp. 496-504. 2003.

[7] Kowalczyk-Gajewska, K. and Stupkiewicz, S. Modelling of Texture Evolution in Kobo Extrusion Process, Archives of metallurgy and materials. *Institute of Fundamental Technological Research (ippt).* **vol.** 58, pp. 113-118. 2013.

[8] Song, J. and Curtin, W. A. A nanoscale mechanism of hydrogen embrittlement in metals. *Acta Materialia.* **vol.** 59(4), pp. 1557-1569. 2011.

[9] Lee, J., Lee, T., Kwon, Y. J., Mun, D-J, Yoo, J-Y, and Lee, C. S. Effects of Vanadium Carbides on Hydrogen Embrittlement of Tempered Martensitic Steel. *Metals and Materials International.* **vol.** 22(3), pp. 364-372. 2016.

[10] Szost, B. A., Vegter, R. H., and Rivera-Díaz-Del-Castillo, P.E.J. Hydrogen-Trapping Mechanisms in Nanostructured Steels. *Metallurgical and Materials Transactions A.* **vol.** 44A, pp. 4542-4550. 2013.

[11] Szost, B. A., Vegter, R. H., and Rivera-Díaz-Del-Castillo, P.E.J. Developing bearing steels combining hydrogen resistance and improved hardness. *Materials & Design.* pp. 499-506. 2013.

[12] Wei, F. G., Hara, T., and Tsuzaki, K. Precise determination of the activation energy for desorption of hydrogen in two Ti-added steels by a single thermal-desorption spectrum. *Metallurgical and Materials Transactions B.* **vol.** 35(3), pp. 587-597. 2004.

[13] Choo, W. Y. and Lee, J. Y. Thermal Analysis of Trapped Hydrogen in Pure Iron. *Metallurgical and Materials Transactions A.* **vol.** 13A, pp. 135-140. 1982.

[14] Eliaz, N., Shachar, A., Tal, B., and Eliezer, D. Characteristics of hydrogen embrittlement, stress corrosion cracking and tempered martensite embrittlement in high-strength steels. *Engineering Failure Analysis.* **vol.** 9(2), pp. 167-184. 2002.

[15] Erick Shaw Alley, E. S. *Influence of microstructure in rolling contact fatigue of bearing steels with inclusions*. PhD thesis Georgia Institute of Technology. 2009.

[16] Walker, P. F. *The Relationship between Early Processing and Properties in Bearing Steels*. PhD thesis University of Cambridge, UK. 2015.

[17] Otsuka, T., Hanada, H., Nakashima, H., Sakamoto, K., Hayakawa, M., Hashizume, K., and Sugisaki, M. Observation of Hydrogen Distribution around Non-Metallic Inclusions in Steels with Tritium Microautoradiography. *Fusion Science and Technology*. **vol.** 48, pp. 708-711. 2005.

[18] Van der Ven, A. and Ceder, G. The thermodynamics of decohesion. *Acta Materialia*. pp. 1223-1235. 2004.

[19] Sears Brands SKF spherical roller bearings:Setting the standard for performance and reliability. http://https://www.skf.com/binary/26-148465/6100_EN.pdf. Accessed: 2019.

[20] Horvath, C.D. *Advanced steels for lightweight automotive structures*. Cambridge: Woodhead Publishing. pp. 35-78. 2010.

[21] Erdemir, A. Rolling-contact fatigue and wear resistance of hard coatings on bearing-steel substrates. *Surface and Coatings Technology*. **vol.** 54-55(1), pp. 482-489. 1992.

[22] Bhadeshia, A.H. K. D. H. Recent developments in bearing steels. *Materials Science and Technology*. **vol.** 32, pp. 1059-1061. 2016.

[23] Joo Hyun, R. *Hydrogen Embrittlement in TRIP and TWIP Steels*. PhD thesis. Pohang University of Science and Technology. 2012.

[24] ISO 4042, Annex A: hydrogen embrittlement relief after electroplating. https://www.iso.org/obp/ui/#iso:std:iso:4042:ed-2:v1:en. Accessed: 2015.

[25] Woodtli, J. and Kieselbach, R. Damage due to hydrogen embrittlement and stress corrosion cracking. *Engineering Failure Analysis*. **vol.** 7, pp. 427-450. 2000.

[26] Heitjans, P. and Karger, J. *Diffusion in condensed matter: Methods, Materials, Models*. 2nd edition. Birkhauser, p. 1-965, 2005.

[27] Louthan, M.R., Bernstein, I.M. and Thompson, A.W. *Hydrogen in Metals*. ASM. Metals Park, OH, p. 53. 1974.

[28] Nelson, H.G. Hydrogen embrittlement. *Treatise on Materials Science & Technology*. **vol.** 25, pp. 275-359. 1983.

[29] Bernstein, I.M., Garber, R. and Pressouyre, G.M. *Effect of Hydrogen on Behaviour of Materials*. TMS-AIME. Metals Park, OH, 1974, p. 53. New York, 1976, p. 37.

[30] Chene, J. Stress Corrosion Cracking of Nickel Based Alloys in Water-cooled Nuclear Reactors - Chapter 7. Woodhead Publishing. 2016.

[31] Derbeken, J. V. Corrosive salty water threatens 120 Bay Bridge anchor rods. https://www.sfgate.com/bayarea/article/Corrosive-salty-water-threatens-120-Bay-Bridge-6308061.php. Accessed: 2019.

[32] Hydrogen embrittlement in high-strength steels. http://www.tribonet.org/hydrogen-embrittlement-in-high-strength-steels/. Accessed: 2019.

[33] Oriani, R.A. The diffusion and trapping of hydrogen in steel. *Acta Metallurgica*. **vol.** 18, pp. 147-157. 1970.

[34] Lynch, S.P. Environmentally assisted cracking: overview of evidence for an adsorption-induced localised-slip process. *Acta Metallurgica*. **vol.** 20, pp. 2639-2661. 1988.

[35] Beachem, C.D. A new model for hydrogen assisted cracking (Hydrogen embrittlement). *Metallurgical and Materials Transactions.* **vol.** 3, pp. 437-451. 1972.

[36] Rebecca, C. *Investigation on fatigue crack growth and hydrogen embrittlement on pipeline steels.* Master's thesis. Politecnico di Milano, Italy. 2009/2010.

[37] Lynch, S.P. Progress towards understanding mechanisms of hydrogen embrittlement and stress corrosion cracking. *Corrosion NACE.* **Paper No.** 07493. 2007.

[38] Troiano, A.R. The role of hydrogen and other interstitials in the mechanical behavior of metals. *ASM-Trans.* **vol.** 52, pp. 54-80. 1960.

[39] Oriani, R.A. A mechanistic theory of hydrogen embrittlement of steels. *Berichte der Bunsengesellschaft für physikalische Chemie.* **vol.** 52, pp. 848-857. 1972.

[40] Lynch, S.P. *Stress Corrosion Cracking Theory and Practice.* Defence Science and Technology Organisation, Australia. pp. 90-130. 2011.

[41] Vehoff, H. *Hydrogen related material properties - Hydrogen in Metals III. Topics in Applied Physics.* Springer, Berlin, Heidelberg pp. 215-278. 1997.

[42] Lynch, S.P. Mechanisms of hydrogen assisted cracking - a Review. *Conference: International Conference on Hydrogen Effects on Material Behaviour and Corrosion Deformation Interactions. At: Moran, WY.* pp. 449-466. 2003.

[43] Stellwag, B. and Kaeschke, H. Kinetics of H-induced stress corrosion cracking. [in German] *Werkstoe und Korrosion.* **vol.** 33, pp. 274-280. 1982.

[44] Jones, D.A. *Principles and prevention of corrosion.* Macmillan Publishing Company, New York. pp. 234-289; 333-355. 1992.

[45] Hertzberg, R. W. *Deformation and fracture mechanics of engineering materials.* 4th ed. New York: John Wiley & Sons. pp. 460-464; 485-520. 1996.

[46] Jones, R. H., Ricker, R. E. *Stress-corrosion cracking. Metals handbook.* 9th ed. Ohio: ASM International. pp. 145-163. 1987.

[47] Mouritz, A. *Introduction to Aerospace Materials.* Woodhead Publishing Limited. pp. 428-453. 2012.

[48] Ryu, J. H., Kim, S. K., Lee, C. S., Suh, D-W and Bhadeshia, H. K. D. H. Effect of aluminium on hydrogen-induced fracture behaviour in austenitic Fe-Mn-C steel. Proceedings of The Royal Society A Mathematical Physical and Engineering Sciences. **vol.** 469, pp. 469. 2012.

[49] Koyama, M., Akiyama, E. and Tsuzaki, K. Effect of hydrogen content on the embrittlement in a Fe-Mn-C twinning-induced plasticity steel. *Corrosion Science.* **vol.** 59, pp. 277-281. 2012.

[50] Martin, M. L., Fenske, J. A., Liu, G. S., Sofronis, P. and Robertson, I. M. On the formation and nature of quasi-cleavage fracture surfaces in hydrogen embrittled steels. *Acta Materialia.* **vol.** 59, pp. 1601-1606. 2011.

[51] Shah, M. Development of Bainite-Austenite Steel by Air Cooling with Good Erosion Resistance. Thesis. Academy of Scientific and Innovative Research, India. 2015.

[52] Sofronis, P. and Robertson, I. M. A Combined Materials Science/Mechanics Approach to the Study of Hydrogen Embrittlement of Pipeline Steels. Hydrogen and Fuel Cells Program Review (Presentation May 10, 2011). https://www.hydrogen.energy.gov/pdfs/review11/pd023_sofronis_2011_p.pdf. Accessed: 2019.

[53] Robertson, I. M. The effect of hydrogen on dislocation dynamics, Engineering Fracture Mechanics. *Engineering Fracture Mechanics.* **vol.** 68, pp. 671-692. 2001.

[54] Robertson, I. M. *Dislocations in solids.* Elsevier, New York. vol. 195. 2009.

[55] Birnbaum, H.K. and Sofronis, P. Hydrogen-enhanced localized plasticity - A mechanism for hydrogen-related fracture. *Materials Science and Engineering: A* **vol.** 176(1-2), pp. 191-202. 1994.

[56] ASTM International *Failures of Rolling-Element Bearings: Failure Analysis and Prevention.* Metals Handbook - 9th edn. (ASTM International, West Conshohocken). **vol.** 11, pp. 508. 1990.

[57] Otai ASTM 52100 Bearing Steel, Otai Special Steel. http://www.astmsteel.com/product/52100-bearing-steel-aisi/. Accessed: 2018.

[58] Dossett, J. L. and Totten, G. E. *Heat Treating of Irons and Steels.* ASM International. **vol.** 4D. 2014.

[59] Briant, C. L. and Banerji, S. K. Intergranular failure in steel: role of grain boundary composition. *International metals reviews.* **vol.** 23(1), pp. 164-199. 1978.

[60] Rycerz, P., Olver, A., and Kadiric, A. Propagation of surface initiated rolling contact fatigue cracks in bearing steel. *International Journal of Fatigue.* **vol.** 97, pp. 29-38. 2017.

[61] Kang, J. H., Hosseinkhani, B., and Rivera-Díaz-del Castillo, P. E. J. Rolling contact fatigue in bearings: multiscale overview. *MaterialsScience and Technology.* **vol.** 28(1), pp. 44-49. 2012.

[62] Ganti,S., Turner, B., Kirsch, M., Anthony, D., McCoy, B., Trivedi, H., and Veeraraghavan, S. Three-dimensional (3D) analysis of white etching bands (WEBs) in AISI M50 bearing steel using automated serial sectioning. *Materials Characterization.* **vol.** 138(1), pp. 11-18. 2018.

[63] Ono, K. and Meshii, M. Hydrogen Detrapping from Grain Boundaries and Dislocations in High Purity Iron. *Acta Metallurgica et Materialia.* **vol.** 40, pp. 1357-1364. 1992.

[64] Fu, H. *Microstructural alterations in bearing steels under rolling contact fatigue.* PhD thesis University of Cambridge, UK. 2017.

[65] Martin, J. A., Borgese, S. F., and Eberhardt, A. D. Microstructural alterations of rolling bearing steel undergoing cyclic stressing. *Journal of Fluids Engineering.* **vol.** 88(3), pp. 555-565. 1966.

[66] Grabulov, A., Ziese, U., and Zandbergen, H. W. TEM/SEM investigation of microstructural changes within the white etching area under rolling contact fatigue and 3-D crack reconstruction by focused ion beam. *Scripta Materialia.* **vol.** 57(7), pp. 635-638. 2007.

[67] Grabulov, A., Petrov, R., and Zandbergen, H. W. EBSD investigation of the crack initiation and TEM/FIB analyses of the microstructural changes around the cracks formed under rolling contact fatigue (RCF). *International Journal of Fatigue.* **vol.** 32(3), pp. 576-583. 2010.

[68] Evans, M-H. White structure flaking (WSF) in wind turbine gearbox bearings: effects of butterflies and white etching cracks (WECs). *Materials Science and Technology.* **vol.** 28, pp. 3-22. 2012.

[69] Bush, J. J., Grube, W. L., and Robinson, G. H. Microstructural and residual stress changes in hardened steel due to rolling contact. *Transactions of the ASM.* **vol.** 54, pp. 390-412. 1961.

[70] Swahn, H., Becker, P. C., and Vingsbo, O. Martensite decay during rolling contact fatigue in ball bearings. *Metallurgical transactions A*. **vol.** 7(8), pp. 1099-1110. 1976.

[71] Warhadpande, A., Sadeghi, F., and Evans, R. D. Microstructural alterations in bearing steels under rolling contact fatigue part 1: historical overview. *Tribology Transactions*. **vol.** 56(3), pp. 349-358. 2013.

[72] Swahn, H., Becker, P. C., and Vingsbo, O. Electron-microscope studies of carbide decay during contact fatigue in ball bearings. *Metal Science*. **vol.** 10(1), pp. 35-39. 1976.

[73] Juvonen, P. *Effects of Non-metallic Inclusions on Fatigue Properties of Calcium Treated Steels*. Doctor of Science in Technology Thesis Otamedia OY, Espoo, Finland. 2004.

[74] Radu, C. It's All About the Steel: the Importance of Bearing Steel Cleanliness for Long-Life Applications *RKB technical review*. 2011.

[75] Rolling Bearings Bearings Materials, NSK Motion and Control. www.nskamericas.com. Accessed: 2019.

[76] Voort, V. and George F. *Metallographic, Principles and Practice*. McGraw-Hill. New York, NY 1984.

[77] Sauveur, A. *Metallography and heat treatment of iron and steel-4th ed.* McGraw-Hill. New York, NY. 1935.

[78] NPTEL. Lecture28: inclusion sources and control. https://nptel.ac.in/courses/113104059/lecture_pdf/Lecture%2028.pdf. Accessed: 2019.

[79] Atkinson, H.V. and Shi, G. Characterization of inclusions in clean steels: a review including the statistics of extremes methods. *Progress in Materials Science*. **vol.** 48, pp. 457-520. 2003.

[80] Nagumo, M. Hydrogen related failure of steels - a new aspect. *Materials science and technology*. **vol.** 20, pp. 940-950. 2004.

[81] Guetard, G. and Rivera-Díaz-del-Castillo, P.E.J. Formation of oxide under rolling contact fatigue. *Tribology International*. **vol.** 95, pp. 262-266. 2016.

[82] Nakai, Y., Shiozawa, D., Kikuchi, S., Obama, T., Saito, H., Makino, T., and Neishi, Y. Effects of inclusion size and orientation on rolling contact fatigue crack initiation observed by laminography using ultra-bright synchrotron radiation. *Procedia Structural Integrity*. **vol.** 2, pp. 3117-3124. 2016.

[83] *Steels for Bearing Production from Ovako*. 2006.

[84] *Ovako Steel Cleanliness Specifications*. Technical Report. 1/1998.

[85] Anmark, N., Karasev A., and Jonsson P.G. The Effect of Different Non-Metallic Inclusions on the Machinability of Steels. *Materials*. **vol.** 8, pp. 751-783. 2015.

[86] Todoshchenko, O. M. I., Yagodzinskyy, Y., Saukkonen, T., and Hanninen, H. Role of Nonmetallic Inclusions in Hydrogen Embrittlement of High-Strength Carbon Steels with Different Microalloying. *Metallurgical and Materials Transactions A*. **vol.** 45(11), pp. 4742-4747. 2014.

[87] Vegter,R. H. and Slycke, J. T. The Role of Hydrogen on Rolling Contact Fatigue Response of Rolling Element Bearings. *Journal of ASTM International*. **vol.** 7(2), pp. 1-12. 2009.

[88] Uyama, H., Yamada, H., Hidaka, H., and Mitamura, N. The Effects of Hydrogen on Microstructural Change and Surface Originated Flaking in Rolling Contact Fatigue. *Tribology Online*. **vol.** 6(2), pp. 123-132. 2011.

[89] Ciruna, J.A. and Szieleit, H.J. The effect of hydrogen on the rolling contact fatigue life of AISI 52100 and 440C steel balls. *Wear*. **vol.** 24(1), pp. 107-118. 1973.

[90] Tal-Gutelmacher, E., Eliezer, D., and Abramov, E. Thermal desorption spectroscopy (TDS) - Application in quantitative study of hydrogen evolution and trapping in crystalline and non-crystalline materials. *Materials Science and Engineering A*. **vol.** 445-446, pp. 625-631. 2007.

[91] McNabb, A and Foster, P.K. A new analysis of the diffusion of hydrogen in iron and ferritic steels. *Transactions of the Metallurgical Society of AIME*. **vol.** 227, pp. 618-627. 1963.

[92] Szost, B. A. *Hydrogen trapping in bearing steels: mechanisms and alloy design*. PhD thesis. University of Cambridge. 2013.

[93] Pressouyre, G. M. and Bernstein, I. M. A quantitative analysis of hydrogen trapping. *Metallurgical Transactions A*. **vol.** 9(11), pp. 1571-1580. 1978.

[94] Yoshino, Y. Metallurgical Influences on the Hydrogen Uptake by Steel in H2S Environment. *Corrosion*. **vol.** 39(11), pp. 435-444. 1983.

[95] Aoki, K., and Tanino, M. Yawata Technical Report. **No.** 255, pp. 159-161. 1966.

[96] Bernstein, I. M. and Pressouyre, G. M. *Hydrogen Degradation of Ferrous Alloys*. Noyes Publications. Park Ridge, NJ pp. 666. 1985.

[97] Crafts, W., and Lamont, J. *Transactions of the Metallurgical Society of AIME*. p. 562. 1950.

[98] Smith, C. S. *Trans. AIME.* **vol.** 175, pp. 15. 1948.

[99] Oikawa, T., Zhang, J. J., Enomoto, M., and Adachi, Y. Influence of Carbide Particles on the Grain Growth of Ferrite in an Fe-0.1C-0.09V Alloy. *ISIJ International.* **vol.** 53(7), pp. 1245-1252. 2013.

[100] Vanherpe, L., Moelans, N., Blanpain, B. and Vandewalle, S. Pinning effect of spheroid second-phase particles on grain growth studied by three-dimensional phase-field simulations. *Computational Materials Science.* **vol.** 49(2), pp. 340-350. 2010.

[101] Zajac, S., Siwecki, T., Hutchinson, W.B., and Lagneborg, R. Strengthening mechanisms in vanadium microalloyed steels intended for long products. *ISIJ international.* **vol.** 38(10), pp. 1130-1139. 1998.

[102] Asahi, H., hirakami, D., and yamasaki, S. Hydrogen trapping behaviour in vanadium-added steel. *ISIJ international.* **vol.** 43(4), pp. 527-533. 2003.

[103] Yamazaki, S. and Takahashi, T. Evaluation method of delayed fracture property of high strength steels. *Tetsu-to-Hagané.* **vol.** 83(7), pp. 454-459. 1997.

[104] Yamasaki, S. and Bhadeshia, H. K. D. H. Modelling and characterisation of V_4C_3 precipitation and cementite dissolution during tempering of Fe-C-V martensitic steel. *Materials Science and Technology.* **vol.** 19, pp. 1335-1343. 2003.

[105] Yamasaki, S. and Bhadeshia, H. K. D. H. M_4C_3 precipitation in Fe-C-Mo-V steels and relationship to hydrogen trapping. *Proceedings A.* **vol.** 462, pp. 2315-2330. 2006.

[106] Kawakami, K. and Matsumiya, T. Numerical analysis of hydrogen trap state by TiC and V_4C_3 in bcc-Fe. *ISIJ international.* **vol.** 52(9), pp. 1693-1697. 2012.

[107] Chen, Y.-S., Haley, D., Gerstl, S. S. A., London, A. J., Sweeney, F., Wepf, R. A., Rainforth, W. M., Bagot, P. A. J., and Moody, M. P. Direct observation of individual

hydrogen atoms at trapping sites in a ferritic steel. *Science*. **vol.** 355, pp. 1196-1199. 2017.

[108] Matsumura, O., Sakuma, Y. and Takechi, H. Enhancement of Elongation by Retained Austenite in Intercritical Annealed 0.4C-1.5Si-O.8Mn Steel. *Transactions of the Iron and Steel Institute*. **vol.** 27, pp. 570-579. 1987.

[109] Kuziak, R., Kawalla, R. and Waengler, S. Advanced high strength steels for automotive industry. *Archives of Civil and Mechanical Engineering.*. **vol.** 8(2), 103-117. 2008.

[110] Matsumura, O., Sakuma, Y. and Takechi, H. Enhancement of Elongation by Retained Austenite in Intercritical Annealed 0.4C-1.5Si-O.8Mn Steel. *Transactions of the Iron and Steel Institute*. **vol.** 27, pp. 570-579. 1987.

[111] Sakuma, Y., Matsumara, O. and Takechi, H. Mechanical properties and retained austenite in intercritically heat-treated bainite-transformed steel and their variation with Si and Mn additions. *Metallurgical and Materials Transactions A*. **vols.** 22, pp. 489-498. 1991.

[112] Matsumura, O., Sakuma, Y. and Takechi, H. Retained Austenite in 0.4CSi1.2Mn Steel Sheet Intercritically Heated and Austempered. *ISIJ International*. **vol.** 32(9), pp. 1014-1020. 1992.

[113] Goel, N. C., Sangal, S. and Tangri, K. A theoretical model for the flow behavior of commercial dual-phase steels containing metastable retained austenite: Part I. derivation of flow curve equations. *Metallurgical Transactions A*. **vol.** 16, pp. 2013 - 2021. 1985.

[114] Kim, C. Modeling tensile deformation of dual-phase steel. *Metallurgical Transactions A*. **vol.** 19, pp. 1263 - 1268. 1988.

[115] Rao, B.V.N. and Rashid, M.S. Direct observations of deformation-induced retained austenite transformation in a vanadlum-containing dual-phase steel. *Metallography*. **vol.** 19, pp. 19-37. 1983.

[116] Sangal, S., Goel, N. C. and Tangri, K. Direct observations of deformation-induced retained austenite transformation in a vanadlum-containing dual-phase steel. *Metallurgical and Materials Transactions A*. **vol.** 16, pp. 2023 - 2029. 1985.

[117] Nemecek, S., Novy, Z. and Stanková, H. Optimization of heat treatment of TRIP steels. *La Metallurgia Italiana*. **vol.** 2, pp. 47-51. 2006.

[118] Choi, I.D., Bruce, D.M., Kim, S.J., Lee, C.G.,d Park, S H., Matlock, D.K. and Speer, J.G. Deformation Behavior of Low Carbon TRIP Sheet Steels at High Strain Rates. *ISIJ International*. **vol.** 42, pp. 1483-1489. 2002.

[119] Imai, N., Komatsubara, N. and Kunishige, K. *Japan Technical Information Service*. pp. 25. 1992.

[120] Grajcar, A. and Krztoń, H. Effect of isothermal holding temperature on retained austenite fraction in medium carbon Nb/Ti-microalloyed TRIP steel. *Journal of Achievements in Materials and Manufacturing Engineering*. **vol.** 49(2), pp. 391-399. 2011.

[121] Narayanaswamy, B., Hodgson, P., Timokhina, I. and Beladi, H. The impact of retained austenite characteristics on the two-body abrasive wear behavior of ultrahigh strength bainitic steels. *Metallurgical and Materials Transactions A*. **vol.** 47, pp. 4883-4895. 2016.

[122] Caballero, F. G., García-Mateo, C., Chao, J., Santofimia, M. J., Capdevila, C. and Andrés, C. G. Effects of morphology and stability of retained austenite on the ductility of TRIP-aided bainitic steels. *ISIJ International.* **vol.** 48, pp. 1256-1262. 2008.

[123] Chatterjee, S. *Transformations in TRIP-assisted Steels: Microstructure and Properties.* PhD thesis, University of Cambridge, UK. 2006.

[124] Scheil, E. Uber die Umwandlung des Austenits in Martensit in Eisen-Nickellegierungen unter Belastung. *ZAAC.* **vol.** 207, pp. 21-40. 1932.

[125] Patel, J.R. and Cohen, M. Criterion for the Action of Applied Stress in the Martensitic Transformation. *Acta Metallurgica.* **vol.** 1(5), pp. 531-538. 1953.

[126] Joo Hyun, R. *Hydrogen Embrittlement in TRIP and TWIP Steels.* Ph.D. Pohang University of Science and Technology. 2012.

[127] Chatterjee, S., Murugananth, M. and Bhadeshia, H.K.D.H. δ-TRIP Steel.. *Materials Science and Technology.* **vol.** 23, pp. 819-827. 2007.

[128] Bhadeshia, H.K.D.H. *Bainite in Steels.* Second edition. IOM Communications Ltd. UK. 2001.

[129] Garcia-Mateo, C. and Caballero, F.G. 1.09 - Advanced High Strength Bainitic Steels. *Comprehensive Materials Processing.* **vol.** 1, pp. 165-190. 2014.

[130] Jacques, P.J., Girault, E., Harlet, P. and Delannay, F. The Developments of Cold-rolled TRIP-assisted Multiphase Steels. Low Silicon TRIP-assisted Multiphase Steels. *ISIJ International.* **vol.** 41, pp. 1061-1067. 2001.

[131] Matas, S.J. and Hehemann, R.F. The structure of bainite in hypoeutectoid steels. *Transactions of the Metallurgical Society of AIME.* **vol.** 221(1), pp. 179-185. 1961.

[132] Basuki, A. and Aernoudt, E. Influence of rolling of TRIP steel in the intercritical region on the stability of retained austenite. *Journal of Materials Processing Technology.* **vols.** 89-90, pp. 37-43. 1999.

[133] Schrader, A. and Wever, F. *Arch. Eisenhittenwesen.* **vol.** 23, pp. 489. 1952.

[134] Shi, W., Li, L., Zhou, Y., Fu, R.Y. and Wei, X.C. *Heat Treatment of Metals.* **vol.** 8, pp. 9. 2002.

[135] Mintz, B. The Influence of Al on the Mechanical Properties of Hot Rolled Steel Plates. *Materials Science Forum.* **vols.** 426-432, pp. 1219-1224. 2003.

[136] Girault, E., Martens, A., Jacques, P., Houbaert, Y., Verlinden, B. and Van Humbeeck, J. Comparison of the effects of silicon and aluminum on the tensile behavior of multiphase TRIP-assisted steels. *Materials Science Forum.* **vol.** 44, pp. 885-892. 2001.

[137] Jacques, P. J., Girault, E., Martens, A., Verlinden, B., Van Humbeeck, J, and Delannay, F. *ISIJ International.* **vol.** 41, pp. 1068. 2001.

[138] Kim, J.S., Lee, Y.H., Lee, D.L., Park, K.T. and Lee, C.S. Effect of intergranular ferrite on hydrogen delayed fracture resistance of ultrahigh strength boron-added steel. *ISIJ International.* **vol.** 47, pp. 913-919. 2007.

[139] Ham, J.O., Kim, B.G. and Lee, S.H. Measurement method of sensitivity for hydrogen embrittlement of high strength bolts. *Korean Journal of Metals and Materials.* **vol.** 49, pp. 1-8. 2011.

[140] Mine, Y., Horita, Z. and Murakami, Y. Effect of hydrogen on martensitie formation in austenitic stainless steels in high-pressure torsion. *Acta Materialia.* **vol.** 57, pp. 2993-3002. 2009.

[141] Gerberich, W.W., Chen, Y.T. and John, C. A short-time diffusion correlation for hydrogen-induced crack growth kinetics. *Metallurgical Transactions A*. **vol.** 6, pp. 1485-1498. 1975.

[142] Oriani, R.A. and Josephic, P.H. Equilibrium aspects of hydrogen induced cracking of steels. *Acta Metallurgica*. **vol.** 22, pp. 1065-1074. 1974.

[143] Xiukui, S., Jian, X. and Yiyi, L. Hydrogen permeation behavior in metastable austenitic stainless steels 321 and 304. *Acta Metallurgica*. **vol.** 37, pp. 2171-2176. 1989.

[144] Kiuchi, K. and McLellan, R.B. The solubility and diffusivity of hydrogen in well-annealed and deformed iron. *Acta Metallurgica*. **vol.** 31, pp. 961-984. 1983.

[145] Murakami, Y., Kanezaki, T., Mine, Y. and Matsuoka, S. Hydrogen embrittlement mechanism in fatigue of austenitic stainless steels. *Metallurgical and Materials Transactions A*. **vol.** 39, pp. 1327-1339. 2008.

[146] Turnbull, A. and Hutchings, R.b. Analysis of hydrogen atom transport in a two-phase alloy. *Materials science and Engineering A*. **vol.** 177, pp. 161-171. 1994.

[147] Hanada, H., Otsuka, T., Nakashima, H., Sasaki, S., Hayakawa, M. and Sugisaki, M. Profiling of hydrogen accumulation in a tempered martensite microstructure by means of tritium autoradiography. *Scripta Materialia*. **vol.** 53, pp. 1279-1284. 2005.

[148] Wach, S., Miodownik, A.P. and Mackowiak, J. The diffusion of hydrogen through pure iron membranes. *Corrosion Science*. **vol.** 6, pp. 271-285. 1966.

[149] Ronevich, J.A. , De Cooman, B.C., Speer, J.G., De Moor, E. and Matlock, D.K. Hydrogen effects in prestrained transformation induced plasticity steel. *Metallurgical and Materials Transactions A*. **vol.** 43A, pp. 2012-2293. 2012.

[150] Maroef, I., Olson, D.L., Eberhart, M. and Edwards, G.R. Hydrogen trapping in ferritic steelweldmetal. *International Materials Reviews*. **vol.** 47(4), pp. 191. 2002.

[151] Lee, J.-L. and Lee, J.-Y. The interaction of hydrogen with the interface of Al_2O_3 particles in iron. *Metallurgical Transactions A*. **vol.** 1, pp. 2183-2186 1986.

[152] Venezuela, J., Liu, Q., Zhang, M., Zhou, Q. and Atrens, A. The influence of hydrogen on the mechanical and fracture properties of some martensitic advanced high strength steels studied using the linearly increasing stress test. *Corrosion Science*. **vol.** 99, pp. 98-117 2015.

[153] Duprez, L., Verbeken, K. and Verhaege, M. Effect of hydrogen on the mechanical properties of multiphase high strength steel. *Effect of hydrogen on materials*. pp. 62-69. 2009.

[154] Ronevich, J.A., Speer, J.G. and Matlock, D.K. Hydrogen Embrittlement of Commercially Produced Advanced High Strength Sheet Steels. *SAE International Journal of Materials and Manufacturing*. **vol.** 3, pp. 255-267 2010.

[155] Ronevich, J.A., Speer, J.G. and Matlock, D.K. Hydrogen Embrittlement of Commercially Produced Advanced High Strength Sheet Steels. *SAE Technical Paper*. 2010.

[156] Ulmer, D.G. and Altstetter, C.J. Phase relations in the hydrogen-austenite system. *Acta Metallurgica*. **vol.** 41, pp. 2235-2241. 1993.

[157] Rozenak, P. and Bergman, R. X-ray phase analysis of martensite transformations in austenitic stainless steels electrochemically charged with hydrogen. *Materials Science and Engineering A*. **vol.** 437, pp. 366-378. 2006.

[158] Yang, Q., Qaio, L.J., Chiovelli, S. and Luo, L.J. Critical hydrogen charging condtions for martensite transformation and surface cracking in TYPE 304 stainless steel. *Scripta Materialia*. **vol.** 40, pp. 1209-1214. 1999.

[159] Bentley, A.P. and Smith, G.C. Phase transformation of austenitic stainless steels as a result of cathodic hydrogen charging. *Metallurgical Transactions A*. **vol.** 17, pp. 1593-1600. 1986.

[160] Hojo, T., Sugimoto, K.I., Mukai, Y.C. and Ikeda, S.S. Effects of aluminum on delayed fracture properties of ultra high strength low alloy TRIP-aided steels. *ISIJ international*. **vol.** 48, pp. 824-829. 2008.

[161] Laureys, A., Depover, T., Petrov, R. and Verbeken, K. Microstructural characterization of hydrogen induced cracking in TRIP-assisted steel by EBSD. *Materials Characterization*. **vol.** 112, pp. 169-179. 2016.

[162] Pérez Escobar, D., Miñambres, C., Duprez, L., Verbeken, K. and Verhaege, M. Internal and surface damage of multiphase steels and pure iron after electrochemical hydrogen charging. *Corrosion Science*. **vol.** 53, pp. 3166 - 3176. 2011.

[163] Lovicu, G., Bottazzi, M., Ďaiuto, F., Sanctis, M., Dimatteo, A., Santus, C. and Valentini, R. Hydrogen Embrittlement of Automotive Advanced High-Strength Steels. *The Minerals, Metals & Materials Society and ASM International*. **vol.** 43A, pp. 4075-4087. 2012.

[164] McMahon, C.J. Hydrogen-induced intergranular fracture of steels. *Engineering Fracture Mechanics*. **vol.** 68, pp. 773-788. 2001.

[165] Jacques, P.J. Transformation-induced plasticity for high strength formable steels. *Current Opinion in Solid State and Materials Science*. **vol.** 8(3-4), pp. 259-265. 2004.

[166] Andreone, C. and Murut, A. Influence of the austenite retained in the hydrogen embrittlement in AISI 4340. *Scripta Metallurgica.* **vol.** 24, pp. 1453-1458. 1990.

[167] Chan, S.L.I., Lee, H.L. and Yang, J.R. Effect of retained austenite on the hydrogen content and effective diffusivity of martensitic structure. *Metallurgical Transactions A.* **vol.** 22, pp. 2579-2586. 1991.

[168] Park, Y.D., Maroef, I.S., Landau, A. and Olson, D.L. Retained austenite as a hydrogen trap in steel welds. *Welding Journal.* **vol.** 22, pp. 27-35. 2002.

[169] Gu, J.L., Chang, K.D., Fang, H.S. and Bai, B.Z. Delayed fracture properties of 1500MPa Bainite/Martensite dual-phase high strength steel and its hydrogen traps. *ISIJ International.* **vol.** 42, pp. 1560-1564. 2002.

[170] Tsubakino, H., Harada, H. and Yin, J. Thermal release of hydrogen from high strength steel containing retained austenite. *ISIJ International.* **vol.** 39, pp. 298-300. 1999.

[171] Depover, T., Pérez Escobar, D., Wallaert, E., Zermout, Z. and Verbeken, K. Effect of in-situ hydrogen charging on the mechanical properties of advanced high strength steels. *International Journal of Hydrogen Energy.* **vol.** 39, pp. 4647-4656. 2014.

[172] Figueroa, D. and Robinson, M.J. Hydrogen transport and embrittlement in 300M and AerMet100 ultra high strength steels. *Corrosion Science.* **vol.** 52, pp. 1593-1602. 2010.

[173] Escobar, P., Duprez, L., Verbeken, K. and Verhaege, M.. Identification of the hydrogen trap sites in a high strength TRIP steel by means of Thermal Desorption Analysis. *Effects of Hydrogen on Materials.* Proceedings of the 2008 International Hydrogen Conference 2010.

[174] Luppo, M.I. and Ovejero-Garcia, J. The influence of microstructure on the trapping and diffusion of hydrogen in a low carbon steel. *Corrosion Science*. **vol.** 32, pp. 1132-1136. 1991.

[175] Pressouyre, G. M A classification of hydrogen traps in steel. *Metallurgical Transactions A*. **vol.** 10, pp. 1571-1573. 1979.

[176] MatCalc. https://http://matcalc.at. Accessed: 2016.

[177] Spencer, P.J. A brief history of calphad. *Calphad*. **vol.** 32, pp. 8. 2008.

[178] Wagner, R., Kampmann, R., and Voorhees, P.W. *"Homogeneous Second-Phase Precipitation", in Phase Transformations in Materials*. New York: Momentum Press, 2013. Wiley-VCH. pp. 310-407. 1991

[179] Thermo-Calc. Software System. Thermodynamic Framework and Data. Foundation of Computational Thermodynamics. Stockholm, Sweden. Accessed: 2016.

[180] Kozeschnik, E. *Modeling Solid-State Precipitation*. New York: Momentum Press, 2013.

[181] Svoboda, J., Fischer, F.D., Fratzl, P., and Kozeschnik, E. Modelling of kinetics in multi-component multi-phase systems with spherical precipitates I: Theory. *Materials Science and Engineering A*. **vol.** 385, pp. 166-174. 2004.

[182] Zajac, S. Extended Use of Vanadium in a New Generation of Flat Rolled Steels. *in International Seminar on Application Technologies of Vanadium in Flat - Rolled Steels*. 2005.

[183] Russell, K.C. Nucleation in Solid: The Induction and Stady State Effects. *Advances in Colloid and Interface Science*. **vol.** 13, pp. 205. 1980.

[184] Kozeschnik, E. Thermodynamic and kinetic simulations with MatCalc, Lecture notes [Sound Recording]. MatCalc. 2009.

[185] Kozeschnik, E., Svoboda, J., and Fischer, F.D. Modified evolution equations for the precipitation kinetics of complex phases in multi-component systems. *Calphad.* **vol.** 28, pp. 379-382. 2004.

[186] Kozeschnik, E., Svoboda, J., Fratzl, P., and Fischer, F.D. Modelling of Kinetics in Multi-component Multi-phase Systems with Spherical Precipitates II - Numerical Solution and Application. *Materials Science and Engineering A.* **vol.** 385, pp. 157-165. 2004.

[187] Zhu, R., Li, S., Karaman, I., Arroyave R., Niendorf, T., and Maier, H.J. Multi-phase microstructure design of a low-alloy TRIP-assisted steel through a combined computational and experimental methodology. *Acta Materialia.* **vol.** 60, pp. 3022-3033. 2012.

[188] Speich, G.R., Demarest, V.A., and Miller, R.L. Formation of Austenite During Intercritical Annealing of Dual-Phase Steels. *Metallurgical and Materials Transactions A.* **vol.** 12, pp. 1419-1428. 1981.

[189] Luzginova, N. *Microstructure and transformation kinetics in bainitic steels.* PhD thesis Delft University of Technology. pp. 16-18, 2008.

[190] Hopkin, S. *Atomic scale characterisation of bearing steels susceptible to hydrogen embrittlement.* Master's thesis. University of Oxford. 2016.

[191] Gault, B., Moody, M. P., Cairney, J. M., and Ringer, S. P. *Atom Probe Microscopy.* Springer. 1 ed., 2012.

[192] Agilent Technologies, Inc. A.7.G. Chromatograph, Operation Manual. https://www.agilent.com. Accessed: 2015.

[193] Standard Test Method for Knoop and Vickers Hardness of Materials (ASTM E384 - 10e2). https://compass.astm.org/Standards/HISTORICAL/E384-10E2.htm. Accessed: 2015.

[194] Standard Test Methods for Tension Testing of Metallic Materials (ASTM E8 / E8M - 16a). https://www.astm.org/Standards/E8. Accessed: 2017.

[195] Glover, D. *A Ball-Rod Rolling Contact Fatigue Tester*. In STP771-EB Rolling Contact Fatigue Testing of Bearing Steels, edited by JJC Hoo. West Conshohocken, PA: ASTM International. pp. 107-124. 1982.

[196] Käfer, K., Bernardi, H., Santos, O., Otubo, L., Lima, N., and Otubo, J. The influence of microstructure and mechanical resistance on the shape memory of ECAE processed stainless Fe-Mn-Si-Cr-Ni-Co Steel *Materials Research*. **vol.** 21(5). 2018.

[197] McEvily, A.J. and Magee, C.L. Low Alloy Steels. *Iron and Steel Institute, London*. pp. 111-117. 1968.

[198] Magnisci. http://magnisci.com/. Accessed: 2018.

[199] Wu, L.L., Xiao, F.R., Wang, Y.C., Liang, C.B., Sun, G.P., and Liao, B. Effect of vanadium on microstructure and wear resistance of Ni-Cr alloyed cast iron. *International Journal of Cast Metals Research*. **vol.** 26, pp. 176-183. 2013.

[200] Arnoldo, B.J. Microstructure of vanadium-, niobium-and titanium-alloyed high-chromium white cast irons. *International Journal of Cast Metals Research*. **vol.** 13, pp. 343-361. 2001.

[201] Chan, S.L.I. Hydrogen trapping ability of steels with different microstructures. *Journal of the Chinese Institute of Engineers.* **vol.** 22, pp. 43-53. 1999.

[202] Krauss, G. Tempering of Lath Martensite in Low and Medium Carbon Steels: Assessment and Challenges. *steel research international.* **vol.** 89, pp. 43-53. 2018.

[203] Bhadeshia, H. K. D. H. and Honeycombe, R. *Steels: microstructure and properties. The tempering of martensite steels.* pp. 183-208. 2006.

[204] Leslie, W.C. *The physical Metallurgy of Steels.* McGraw-Hill. Tokyo, Japan. 1981.

[205] Egami, T. and Billinge, S.J.L. Underneath the Bragg Peaks, Pergamon Press, Oxford, 2003.

[206] Turk, A., San Martín, D., E.J. Rivera-Díaz-del-Castillo, P. Correlation between vanadium carbide size and hydrogen trapping in ferritic steel. *Scripta Materialia.* **vol.** 152, pp. 112-116. 2018.

[207] Iron-Iron Carbide Phase Diagram Example. https://web.archive.org/web/20080216023642/http://www.sv.vt.edu/classes/MSE2094_NoteBook/96ClassProj/examples/kimcon.html. Accessed: 2019.

[208] Lagneborg, R., Siwecki, T., Zajac, S., and Hutchinson, B. The role of vanadium in microalloyed steels. *Scandinavian Journal of Metallurgy.* **vol.** 28, pp. 186-241. 1999.

[209] Baker, T. Processes, microstructure and properties of vanadium microalloyed steels. *Materials Science and Technology.* **vol.** 25, pp. 1083-1107. 2009.

[210] Miller, M. and Burke, M. An atom probe field ion microscopy study of neutron-irradiated pressure vessel steels. *Journal of Nuclear Materials.* **vol.** 195(1-2), pp. 68-82. 1992.

[211] Lee, J-Y and LEE, S. M. Hydrogen trapping phenomena in metals with b.c.c. and f.c.c. crystal structures by the desorption thermal analysis technique. *Surface and Coatings Technology*. **vol.** 28, pp. 301-314. 1986.

[212] Takai, T., Yamauchi, G., Nakamura, M., and Nagumo, M. *Journal of the Japan Institute of Metals and Materials*. **vol.** 62, pp. 267-275. 1998.

[213] Cheng, L., Enomoto, M., Hirakami, D., and Tarui, T. Influence of Carbon Segregation to Dislocations on Thermal Desorption Spectrum of Hydrogen in Medium Carbon Martensitic Steels. *IsIJ International*. **vol.** 53(1), pp. 131-138. 2013.

[214] Kissinger, H. E. Reaction Kinetics in Differential Thermal Analysis *Analytical Chemistry*. **vol.** 29 (11), pp. 1702-1706. 1957.

[215] Szost, B. A. and Rivera-Díaz-Del-Castillo, P.E.J. Unveiling the nature of hydrogen embrittlement in bearing steels employing a new technique. *Scripta Materialia*. **vol.** 68, pp. 467-470. 2013.

[216] Kohn, D. H. and Ducheyne, P. Tensile and fatigue strength of hydrogen-treated Ti-6Al-4V alloy. *Journal of Materials Science*. **vol.** 26, pp. 328-334. 1991.

[217] Horikawa, K., Yamaue, K., and Kobayashi, H. Effect of continuous hydrogen charging on tensile and fatigue properties of amorphous Ni-Zr alloy membranes. *Materials Transactions*. **vol.** 49(10), pp. 2238-2242. 2008.

[218] Cook, R. F. and Pharr, G. M. Direct observations and analysis of indentation cracking in glasses and ceramics. *Journal of the American Ceramic Society*. **vol.** 73, pp. 787-817. 1990.

[219] Yonezu, A., Masanori, A., Toshiyuki, K., Hiroyuki, H., and Kohji, M. On hydrogen-induced Vickers indentation cracking in high-strength steel. *Mechanics Research Communications*. **vol.** 37, pp. 230-234. 2010.

[220] Dadfarnia, M., Sofronis, P. and Neeraj, T. Hydrogen interaction with multiple traps: Can it be used to mitigate embrittlement?. *International Journal of Hydrogen Energy*. **vol.** 36, pp. 10141-10148. 2011.

[221] Elboujdaini, M. and Revie, R. W. Metallurgical factors in stress corrosion cracking (SCC) and hydrogen-induced cracking (HIC). *J Solid State Electrochem*. **vol.** 13, pp. 1091-1099. 2009.

[222] Depover, T. and Verbeken, K. Evaluation of the effect of V_4C_3 precipitates on the hydrogen induced mechanical degradation in Fe-C-V alloys. *Materials Science & Engineering A*. **vol.** 675, pp. 299-313. 2016.

[223] Hardie, D.,Charles, E.A., and Lopez, A.H. Hydrogen embrittlement of high strength pipeline steels. *Corrosion Science*. **vol.** 48, pp. 4378-4385. 2006.

[224] Li, S., Akiyama, E., Yuuji, K., Tsuzaki, K., Uno, N., and Zhang, B. Hydrogen embrittlement property of a 1700-MPa-class ultrahigh-strength tempered martensitic steel. *Science and Technology of Advanced Materials*. **vol.** 11(2). 2010.

[225] Bailey, N. Fisheyes, hydrogen embrittlement and removal. *TWI Research Bulletin*. **vol.** 15(12). 1974.

[226] Chen, J.H. and Cao, R. *Micromechanism of cleavage fracture of metals: A cmprehensive microphysical model for cleavage cracking in metals.* Butterworth-Heinemann. Oxford. UK. 2015.

[227] Fan, D., Jahangiri, N., Kaushik, P., Pielet, H., and Jun, H. Bending performance improvement of dual-phase steel with 1000-MPa tensile strength. *Conference: International symposium on new developments in advanced high-strength sheet steels*. 2017.

[228] X. Sun, K.S. Choi, A. Soulami, W.N. Liu, and M.A. Khaleel, On key factors influencing ductile fractures of dual phase (DP) steels. *Materials Science and Engineering A*. **vol.** 526(1-2), pp. 140-149. 2009.

[229] Guetard, G. *Powder and ingot metallurgical bearing steels*. PhD thesis University of Cambridge, UK. 2016.

[230] Koyama, M., Rohwerder,M., Tasan, C.C., Bashir,A., Akiyama, E., Takai, K., Raabe, D., and Tsuzaki, K. Recent progress in microstructural hydrogen mapping in steels: quantification, kinetic analysis, and multi-scale characterisation. *Materials Science and Technology*. **vol.** 33, pp. 1481-1496. 2017.

[231] Koyama, M., Abe, Y., Saito, K., Akiyama, E., Takai, K., and Tsuzaki, K. Martensitic transformation-induced hydrogen desorption characterized by utilizing cryogenic thermal desorption spectroscopy during cooling. *Scripta Materialia*. **vol.** 122, pp. 50-53. 2016.

[232] Caballero, F.G., Capdevila, C. and García de Andrés, C. Influence of Pearlite Morphology and Heating Rate on the Kinetics of Continuously Heated Austenite Formation in a Eutectoid Steel. *Metallurgical and Materials Transactions A*. **vol.** 32, pp. 1283-1291. 2001.

[233] De Meyer, M., Mahieu, J. and De Cooman, B.C. Empirical Microstructure Prediction Method for Combined Intercritical Annealing and Bainitic Transformation of TRIP steel. *Materials Science and Technology*. **vol.** 10, pp. 1121-1132. 2002.

[234] The Iron-Carbon System http://www.uobabylon.edu.iq

[235] Oliveira, F.L.G., Andrade, M.S. and Cota, A.B. Kinetics of austenite formation during continuous heating in a low carbon steel. *Materials Characterization*. **vol.** 58, pp. 256-261. 2007.

[236] The Iron-Iron Carbide Diagram. The Hand Book on Mechanical Maintenance. http://practicalmaintenance.net/?p=1315

[237] Ayer, R. and Machmeier, P.M. Transmission electron microscopy examination of hardening and toughening phenomena in Aermet 100. *Metallurgical Transactions A*. **vol.** 24, pp. 1943-1955. 1993.

[238] Sato, K. *Improving the Toughness of Ultrahigh Strength Steel*. PhD thesis, University of California. 2002.

[239] Yi, H.L., Chen, P. and Bhadeshia, H.K.D.H. Optimizing the morphology and stability of retained austenite in a δ-TRIP steel. *Metallurgical and Materials Transactions A*. **vol.** 45(8), pp. 3512-3518. 2014.

[240] Ding, R., Tang, D. and Zhao, A.M. A novel design to enhance the amount of retained austenite and mechanical properties in low-alloyed steel. *Scripta Metallurgica*. **vol.** 88, pp. 21-24. 2014.

[241] Miller, R. *Transactions of the American Society of Metals*. **vol.** 57, pp. 892-899. 1964.

[242] Dyson, D.J. and Holmas, B. *Journal of the Iron and Steel Institute*. **vol.** 208, pp. 469. 1970.

[243] Wei, Xu. *Genetic Design of Ultra High Strength Stainless Steels: Modelling and Experiments*. Ph.D. thesis, University of Science and Technology, China. 2oo9.

[244] Kokosza, A. and Pacyna, J. *Archives of Metallurgy and Materials.* **vol.** 55, pp. 1001-1006. 2010.

[245] Gruber, M., Ploberger, S., Wiessner, M., Marsoner, S. and Ebner, R. Influence of heat treatment on the microstructure of a high Co-Ni secondary hardening steel. *Archives of Metallurgy and Materials* **vol.** 60, pp. 2131-2137. 2015.

[246] Standard Test Method for Determining Volume Fraction by Systematic Manual Point Count [ASTM E562 - 11]. http:///practicalmaintenance.net/?p=1315

[247] Owen, W. S. The effect of silicon on the kinetics of tempering. *Transactions of the American Society of Metals* **vol.** 46, pp. 812-829. 1954.

[248] Gordine, J. and Codd, I. The influence of Si up to 1.5 wt% on the tempering of a spring steel. *Journal of the Iron and Steel Institute* **vol.** 207, pp. 461-467. 1969.

[249] Hobbs, R. M., Lorimer, G. W. and Ridley, N. Effect of silicon on the microstructure of quenched and tempered medium carbon steels. *Journal of the Iron and Steel Institute* **vol.** 210, pp. 757-764. 1972.

[250] Bhadeshia, H.K.D.H. and Christian, J. W. Effect of silicon on the microstructure of quenched and tempered medium carbon steels. *Metallurgical transactions A* **vol.** 21, pp. 767-797. 1990.

[251] Singh, S. B. and Bhadeshia, H.K.D.H. Effect of silicon on the microstructure of quenched and tempered medium carbon steels. *Materials Science and Engineering: A* **vol.** 12, pp. 610-612. 1996.

[252] Santofimia, M.J., Caballero, F.G., Capdevila, C., García-Mateo, C. and García de Andrés, C. Evaluation of Displacive Models for Bainite Transformation Kinetics in Steels. *Materials Transactions* **vol.** 47(6), pp. 1492 - 1500. 2006.

[253] Bhadeshia, H.K.D.H. and Waugh, A.R. *Acta Metallurgica* **vol.** 30, pp. 775-784. 1982.

[254] Chang, L. C. and Bhadeshia, *Materials Science and Engineering: A* **vol.** 184, pp. 17-20. 1994.

[255] Stark, I., Smith, G. D. and Bhadeshia, H.K.D.H. *Solid-Solid Phase Transformations* ed. by G. W. Lorimer (Institute of Metals, London). 1988.

[256] Garcia-Mateo, C., Caballero, F.G. and Bhadeshia, H.K.D.H. Acceleration of Low-temperature Bainite. *ISIJ International.* **vol.** 43, pp. 1821-1825. 2003.

[257] Cornide, J., Miyamoto, G., Caballero, F., Furuhara, T., Miller, M. K., Garcia-Mateo, C. Distribution of Dislocations in Nanostructured Bainite, Solid State Phenomena. *Solid State Phenomena* **vols.** 172-174, pp. 117-122. 2011.

[258] Jacques, P., Furnemont, Q., Mertens, A. and Delannay, F. On the sources of work hardening in multiphase steels assisted by transformation-induced plasticity. *Philosophical Magazine A* **vol.** 81, pp. 1789-1812. 2001.

[259] Castro, F.J. and Meyer, G. Thermal desorption spectroscopy (TDS) method for hydrogen desorption characterization (I): theoretical aspects. *Journal of alloys and Compounds* **vol.** 330, pp. 59-63. 2002.

[260] Fuchigami, H., Minami, H. and Nagumo, M. Effect of grain size on the susceptibility of martensitic steel to hydrogen-related failure. *Philosophical Magazine Letters* **vol.** 86, pp. 21-29. 2006.

[261] Bernstein, I.M. and Thompson, A. W. Effect of Metallurgical Variables on Environmental Fracture of Steels. *International Metals Reviews (Review No. 212)* **vol.** 21, pp. 269-287. 1976.

[262] Procter, R.P.M. and Paxton, H.W. Hydrogen Embrittlement of Stainless Steel and carbon steel. *TRANS ASM* **vol.** 62, pp. 989. 1969.

[263] Banerjee, M. K. *Comprehensive Materials Finishing* **vol.** 2, pp. 180-213. PUBLISHER(S) Elsevier BV. 2017.

[264] Zaefferer, S., Ohlert, J. and Bleck, W. A study of microstructure, transformation mechanisms and correlation between microstructure and mechanical properties of a low alloyed TRIP steel. *Acta Materialia* **vol.** 52, pp. 2765-2778. 2004.

[265] Enomoto, D. and Hirakami, M. Thermal desorption analysis of hydrogen in high strength martensitic steels. *Metallurgical and Materials Transactions A* **vol.** 43, pp. 1-10. 2011.

[266] Park, Y.D., Landau, A., Olson, D.L., Maroef, I. and Edwards, G.R. Proc. 5th International Conference Trends in Welding Research. pp. 31-36. Ohio. 1998.

[267] Asahi, H., Hirakami, D., and Yamasaki, S. Hydrogen trapping behavior in vanadium-added steel. *ISIJ International* **vol.** 43(4), pp. 527-533. 2003.

[268] Xiang, S., Ma, R., and Zhang, X. Removing hydrogen in solid metal using electric current pulse, *Journal of Alloys and Compounds* **vol.** 845. 2020